UNIVERSITÀ DELLA CALABRIA

UNIVERSITA' DELLA CALABRIA

Dipartimento di FISICA

Scuola di Dottorato

ARCHIMEDE IN SCIENZE, TECNOLOGIE E COMUNICAZIONE

Indirizzo

Via Pietro Bucci. Laboratorio di Nanoscienze di Superficie. Cubo 33C. Piano Terra. UNICAL

Con il contributo di

UNIVERSIDAD NACIONAL DE CHIMBORAZO-ECUADOR

CICLO

XXVIII

TITOLO TESI

Experimental and Theoretical Study of Polyhedral Carbon Nano-Onions

Settore Scientifico Disciplinare: FIS/01 FISICA SPERIMENTALE, CHIM/02 CHIMICA FISICA

Direttore: Ch.mo Prof. PIETRO PANTANO

Firma _____

Supervisore: Ch.mo Prof. LORENZO CAPUTI

Firma _____

Co-relatore: Ch.mo Dr. GIORGIO DE LUCA

Firma _____

Dottorando: Dott. Marlon Basantes Valverde

Firma _____

UNIVERSITÀ DELLA CALABRIA

Dipartimento di FISICA

Experimental and Theoretical Study of Polyhedral Carbon Nano-Onions

A dissertation submitted to the PhD school of

Archimede in Scienze, Tecnologia e Comunicazione

For Fulfillment of the Requirements for the Degree of Doctor of Philosophy
in Physics and Nanomaterials

By
Marlon Danilo Basantes Valverde

Supervisor
Prof. Lorenzo S. Caputi

Co-relatore
Dr. Giorgio De Luca

PhD Coordinator
Prof. Pietro Pantano

(2014-2017), Rende/Italy

Dedication

A mi papá Humberto y a mi mamá Judith a quienes les debo todo.

A mi amada y querida esposa Clara María.

A Geovanny, Williams y Jeaneth.

Dedico esta investigación

(I dedicate this Research)

ACKNOWLEDGMENT

I would like to sincerely thank my supervisor ***Prof. Lorenzo Caputi*** for his excellent guidance, who knew how to guide my research. Thanks to his high vision in both experimental and theoretical knowledge.

Thanks very much to Dr. Giorgio De Luca ITM-CNR for his help, guidance and friendship. He was a very important support in my theoretical Chemical-Physics formation.

Thanks a lot to the members of Laboratory of Surface Nanoscience for their friendship and for providing me the best conditions to carry out my research. I also express special thanks to all my seniors and junior colleagues in the lab; Nadia, Denia, Salih, Francesca and Andrea for better teamwork and the lovely friendship environment they have given me.

Also, I would like to thank the Universidad Nacional de Chimborazo in Ecuador for their financial support in my doctoral studies.

I am also grateful to my family support. I would like to thank my father, mother and brothers for their continuous prayers to achieve and complete my work.

In particular, I thank my beloved wife for her encouragement and patience throughout the PhD period. All in my life, I owe to her.

Finally, I would like to express my deep appreciation to all the friends I have known at the UNICAL.

Rende/Italy, November 2017 Marlon Basantes Valverde

CONTENTS

List of Figures

Abstract

Carbon nano-onions (CNOs), in their spherical or polyhedral forms, represent an important class of nanomaterials due to their peculiar physical and electrochemical properties. Among the different methods of production, arc discharge between graphite electrodes sustained by deionized water is one of the most promising to obtain good quality CNOs. The arc discharge method is applied to optimize the production of CNOs, and the synthesized nanomaterials by TEM was studied. An innovative experimental arrangement is used to obtain CNOs dispersed in water together with other carbon nanomaterials, and a black hard cathodic deposit. A simple mechanical grinding of the deposit it allowed to obtain turbostratic polyhedral CNOs with different aspect ratios, which exhibited higher stability towards burning in air, compared to CNOs found in water. A mechanism for the formation of the CNOs contained in the deposit, different from the generally accepted mechanism responsible for the synthesis of CNOs dispersed in water, is hypothesized.

These spherical or polyhedral multi-shell fullerenes are widely studied owing to their interesting electronic and mechanical proprieties; nevertheless, comparative studies on these nanoparticles remain scarce. Herein, some key electronic proprieties of single and double walled icosahedral fullerenes as function of their sizes were calculated in the frame of the Density Functional Theory. In particular, structures of icosahedral polyhedral fullerenes, previously validated, were used to get the gap between the Highest Occupied Molecular Orbital and the Lowest Unoccupied Molecular Orbital levels (H-L gap), electron affinity, first ionization potential, electronegativity as well as the Density of the electronic States. This work shows that the H-L gap of the single-wall fullerenes decreases as the nanoparticles size increases, whereas an opposite trend was obtained for the double walled fullerenes. Going from single to double wall nanoparticles; a systematic and marked decrease of the H-L gap was found although, this difference reduces increasing the size of the double walled up obtaining an inversion. The DOS structures of SW nanoparticles changes radically adding a second shell, and the extent of these changes depends on the sizes of the analyzed fullerenes.

Sommario

I carbon nano-onions (CNOs), costituiti da strati concentrici di atomi di carbonio con ibridizzazione sp^2 e dimensioni dell'ordine delle decine di nanometri, hanno attratto una forte attenzione per le loro elevata conducibilità, elevata area superficiale ed eccezionale velocità dei processi carica e scarica. L'interesse verso i CNOs è molto aumentato, anche grazie allo sviluppo di metodi di preparazione efficaci. Tra essi, la sintesi di CNOs mediante scarica tra elettrodi di grafite in acqua deionizzata è uno dei metodi più promettenti per ottenere CNOs di elevata qualità. I materiali sintetizzati sono stati studiati mediante Microscopia Elettronica a Trasmissione (Transmission Electron Microscopy, TEM). I campioni di materiale generato durante la scarica sono stati prelevati sulla superficie dell'acqua, sul fondo del beaker e sulla superficie del catodo. La formazione del deposito catodico è stata favorita dal particolare allestimento sperimentale, che prevede due gradi di libertà dell'anodo (traslazione e rotazione). A seguito di una macinazione meccanica, il deposito si è rivelato un agglomerato di CNOs poliedrici, molto più stabili in temperatura rispetto ai CNOs presenti nel materiale in sospensione, con strutture grafeniche esenti da difetti, sovrapposte in forma turbostratica. I risultati ottenuti hanno permesso di confutare il modello generalmente accettato in letteratura per la formazione di CNOs mediante scarica in acqua, e di proporre un nuovo modello per la sintesi dei CNOs presenti nel deposito, in cui la cristallizzazione dipende da un intenso gradiente di temperatura esistente in una zona molto vicina alla superficie del catodo.

Negli ultimi anni, i CNOs, sono stati ampiamente studiati sia nella loro forma sferica che poliedrica; tuttavia, la presenza di studi comparativi su tali nanoparticelle risulta essere quasi assente. In tale lavoro, sono state calcolate alcune delle proprietà chiave dei fullereni icosaedrici a singolo e doppio strato mediante la Teoria del Funzionale della Densità (Density Functional Teory, DFT). Le strutture dei fullereni poliedrici, presenti in letteratura, sono state utilizzate per calcolare il valore della gap esistente tra l'orbitale molecolare a più alta energia e l'orbitale molecolare a più bassa energia non occupato (H-L gap), l' affinità elettronica, il primo potenziale di ionizzazione, l' elettronegatività e la densità degli stati elettronici. I nostri risultati mostrano che il valore ricavato per la gap H-L diminuisce all'aumentare della dimensione delle nanoparticelle per i fullereni a singolo strato mentre aumenta nel caso dei fullereni a doppio strato. Si riscontra una diminuzione sistematica e marcata della gap H-L, passando dai fullereni poliedrici a singolo strato a quelli a doppio strato sebbene questa differenza riduca l'aumento delle dimensioni del doppio strato realizzando un' inversione. Le

strutture DOS delle nanoparticelle a singolo strato cambiano radicalmente aggiungendo una seconda shell e l' aumento di questi cambiamenti dipende dalle dimensioni dei fullereni analizzati.

Chapter 1

Introduction

1.1 Nanoscale science and nanostructures

Nanoscience primarily deals with synthesis, characterization, exploration and exploitation of Nanostructured Materials (NSMs). The NSMs are cornerstones of nanoscience and nanotechnology. It has the potential for revolutionizing the ways in which materials and products are created and the range and nature of functionalities that can be accessed. It already has a significant commercial impact, which will assuredly increase in the future as shown in Figure 1.1.

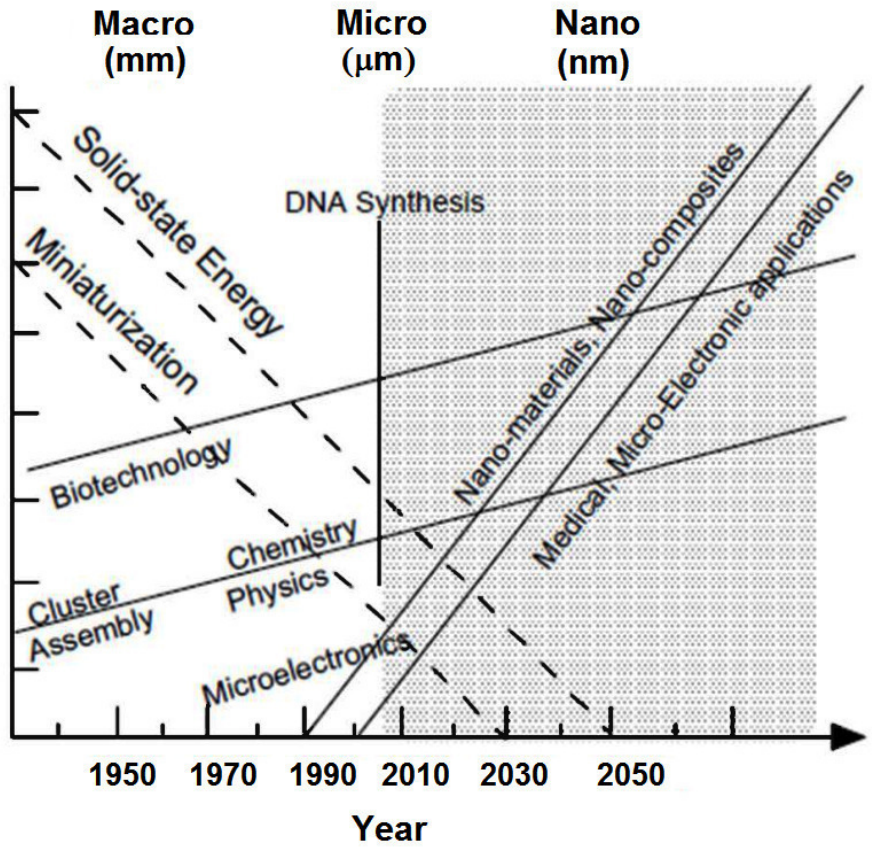

Figure 1.1. Evolution of science-technology and the future [1]

One of the areas of interest in Nano scale science over the last several decades is the construction of NSMs objects or materials from small building blocks of self-assembly [2-3]. A wide variety of nanostructures with different levels of dimensions and complexity, including nanospheres [4], nanocages [5], nanotubes [6-8] and topologically nontrivial assembles have been generated.

Nanoscale science, engineering and technology are areas that deal with matter on the nanometer length scale. Small features permit more functionality in a given space. The nanotechnology is the ability to work at the molecular level, atom by atom, to create large structures with fundamentally new molecular organization. Nanoscale materials are defined as a set of substances where at least one dimension is less than approximately 100 nanometers (nm). In this way, compared to the behavior of isolated molecules of about 1 nm (10^{-9} m or of bulk materials, behavior of structural features in the range of about 10^{-9} to 10^{-7} m (1 to 100 nm) exhibit important changes. NSMs are of interest because at this scale unique optical, magnetic, electrical are other properties emerge. The emergent properties have the potential for great impacts in electronics. Medicine and other fields.

Some NSMs occur naturally, but of particular interest are engineered nanomaterials. The two mail reasons why materials at the nanoscale can be different properties are increased relative surface area and new quantum effects. These NSMs have a much greater surface area to volume ratio than their conventional forms, for example the carbon nanostructures [8-9-10-11]. Also at nanoscale, quantum effects can become much more important determining the material properties and characteristics leading to novel optical, electrical and magnetic behaviours [13].

NSMs have an extremely small size, which heaving at least one dimension 100nm or less. NSMs can be nanoscale in one dimension (e.g. Surface films), two dimensions (e.g. Strands or fibers), or three dimensions (e.g. Particles). They can exist a single, fused, aggregated or agglomerated forms with spherical, tubular and irregular shapes. Common types of NSMs include nanotubes, dendrimers, quantum dots and fullerenes.

In Ref. [14] a restricted set of NSMs classes was suggested to build from the constituting elementary units, namely, 0D quantum dots, nanocrystals, nanoparticles and nanospheres, 1D nanorods, nanobelts, nanowiskers, nanofibers, nanotubes and nanowires, 2D nanosheets, graphene, self-assemble monolayers, Langmuir-Blodgett films, layer by layer assemblies, and interfacial structures [12]. Thus, all Nanostructures (NSs), classified as 0D, 1D, 2D on the basis of their dimensionality and concept of surface forms, can be built from elementary units (blocks) having low dimensionality 0D, 1D, and 2D. The 3D structures can be considered as NSMs if they involve the 0D, 1D, 2D NSs.

Figure 1.2 shows three sorts of elementary units (0D, 1D, 2D) and other classes for a total of 36 classes were defined on the basis of the dimensionality of NSs.

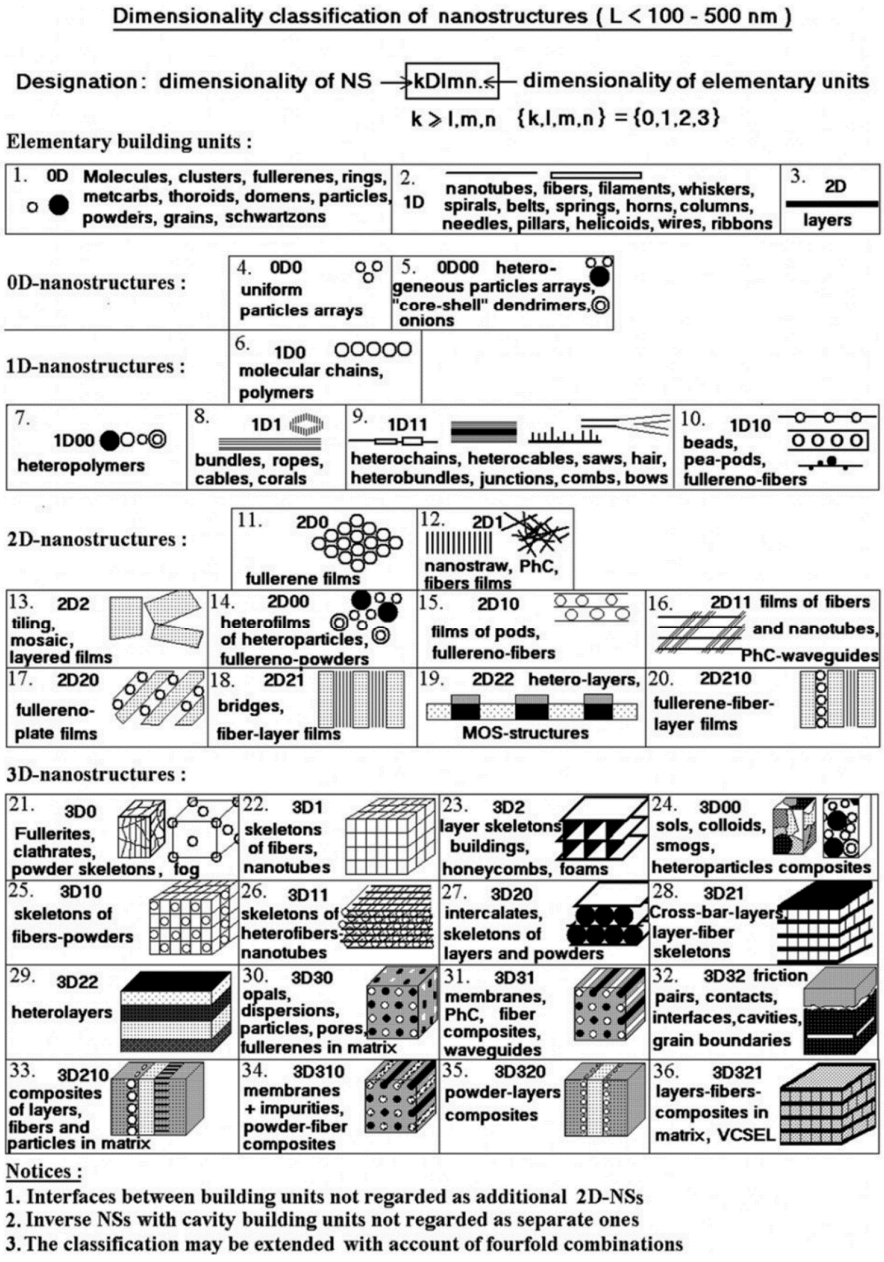

Figure 1.2: Dimensionality classification of nanostructures [14]

Researches expect to develop commercial applications for Nanotechnology (NT) for the next several years. This including: advanced drug; medical diagnostic tools, such as cancer-tagger mechanism and *lab on a chip* diagnostic for physicians; cooling chips or wafer to replace compressors in cars, refrigerators, air conditioners and other devices using non chemical or moving parts; sensors for airborne chemicals or other toxins, solar fuel cells and portable power to provide inexpensive clean energy; etc. NT is proposed presently to define as the complex of fundamental and engineering science that integrates a chemistry, physics and biology of nanostructures with a material science, electronics, and processes technologies focused on a comprehensive research on NSs, on a development of atomist-physical –chemical process self- and automatic-assembling of nanomaterials and workpieces using complex prove microscopies combined with the other tools, resulted in a fabrication and manufacturing of nanodevices, nanomachines, ultra-low integrated circuits, micro-opto-electro- mechanical system, nanobiorobots, etc.

The NT have seen arisen in early 80-th, when the scanning tunneling microscopy, the atomic force and other prove microscopies were invented. These have given the opportunity to realize the main concept formulated by Richard Feynman (1959), namely, to assemble artificially the nanoworkpieces and nanodevices from single atoms and molecules [15].

A nanoparticle (d < 100nm) physically is determined by a variety size effects. The size effects may be divided into two types the internal and external ones, as a well ass the classical and quantum effects. Internal or *intrinsic size effects* as determined as a change of the properties peculiar to particles (the lattice parameters, melting temperature, hardness, band gap, luminescence, diffusion coefficients, chemical activity, sorption, etc. External size effects arise inevitably and always in the process of interaction between different physical fields and matters under decreasing of their building units (the particles, grains domains) down to a crucial value when this size becomes to be comparable with a length of physical phenomena (the free length of electrons, phonons, coherent length irradiative wave, etc.). In turn the *classical size* effects appear to become apparent in variation of lattice, parameters, hardness, plasticity, thermal conductivity, diffusion, etc. The quantum size effects manifest themselves in a blue shift luminescence in the rise of peculiar low-dimensional quantum states, in the quantization of electronconductivity in magnetic field, in the oscillation of the superconductivity critical temperature, magnetoresistance and other physical characteristics, in the generation hypersound, etc. [16].

Nanotechnology therefore is a complex interdisciplinary science including: Nanochemistry, Nanophysics, Nanomaterials science, Nanoelectronics optoelectronics and nanoengeneering, Nanobionics, Nanotechnology nanodevice-building and nano-hand-craft.

Atoms, molecules, clusters, fullerenes, supramolecular structures, their crystals, nanotubes, nanowires, nanorodes, all their arises and photonic crystals serve as NT objectives. Fullerenes and atomic clusters are the smallest zero-dimensional (0D) nanostructures called quantum dots possessing the properties inherent for nanomaterial rather than for single atom. Nanotubes, nanorodes, nanowires, nanofibers manifest more advanced and promising properties as being 1D quantum wires nanoscopic in diameter but microscopic in length. Reduced two-dimensional 2D heterostructures, nanolayers and nanodisks as being the well know 2D quantum wells are believed to migrate from micro- to Nanoelectronics. In addition, the 2D arrays of nanowires and nanotubes ordered in 2D forest arrays in 2D crystals seem to be novel and very perspective core of NT.

One of the basic results of the material sciences is the insight that most properties of solids depend of the microstructure. A reduction in the spatial dimension or confinement of particles or quasi-particles in a particular crystallographic direction within a structure generally leads to change in physical properties of the system in that direction. Figure 1.3 shows the another classification of nanostructure materials and systems essentially depends on the number of dimensions which lie within the nanometer range: a) 3D system confine in three dimensions; b) 2D System confined in two dimensions; c) 1D system confined in one dimension and d) 0D-zero-dimensional structures.

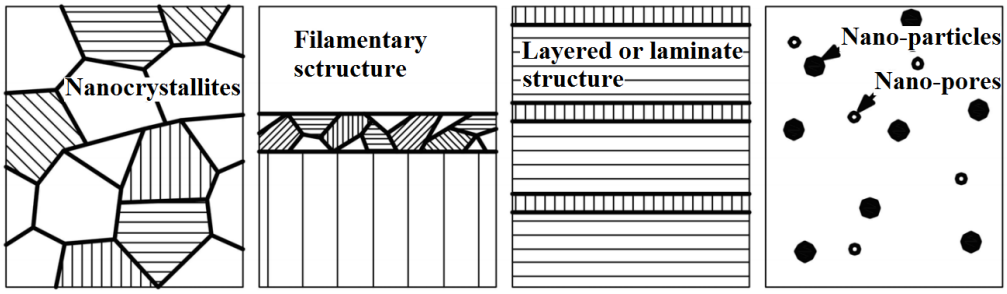

Figure 1.3: Schematic classification of nanomaterials: a) 3D-structures, b) 2D- structures, c) 1D-structures and d) 0D-structures [17]

Thus, is a very important the study of NSMs and their development, as well as the technics for synthesis and consolidation; their properties: mechanical, thermal, electrical, optical, chemical and magnetic [17].

In the last years, some novel materials have been the subject of numerous studies due to their particular structure (some of them of the thickness of an atom) and their multiple applications to the industry and the technology development. These 2-dimensional materials like graphene and silicene have unique physical and chemical properties and are very

important for electronics, chemical, physical and environmental sciences. In addition, within the so-called *carbon nanostructures*, besides the graphene, there are also the carbon nanotubes, fullerenes, nanocones, nanopeapods, nanotorii, nanohorns, nanobuds and onions. Figure 1.4 shows an analogy schematic classification of PbS nanomaterials.

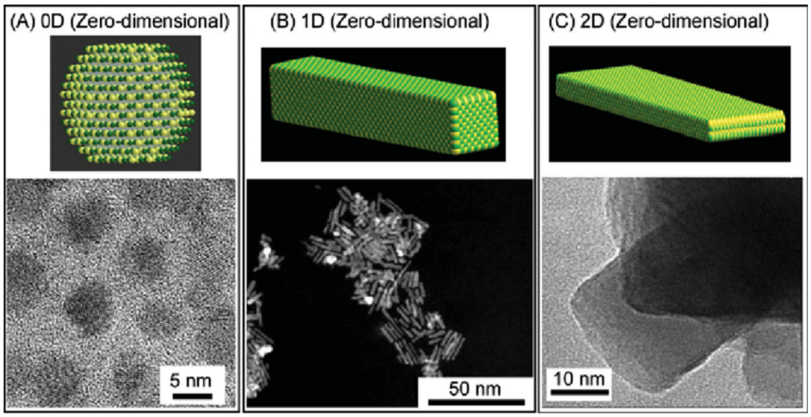

Figure 1.4: 0D, 1D and 2D structures of PbS nanomaterials [12]

One of the more important (relatively news) and promising carbon allotropes are the so-called "carbon nano-onions", which are made of spherical or polyhedral concentric layers of carbon atoms arranged in a honeycomb net. In particular, in the polyhedral carbon nano-onions there are flat and curved zones. The flat face are pieces of graphene.

1.2 Carbon Allotropes

The stable bonding configuration of carbon at ambient conditions is graphite, whit an energy difference between graphite and diamond of $\approx 0.02\ eV$ per atom. Due to the high energetic barrier between the two faces of carbon, the transition from diamond to the stable phase of graphite is very slow at normal conditions. In the reverse direction, there are two methods to produce synthetic diamond from graphite [18]. The original method is High Pressure High Temperature (HPHT) where various types of carbonaceous precursors can be used, including graphite, carbon black, fullerenes, but among these, the graphite is the most widely used. The second method uses Chemical Vapor Deposition (CVD), invented in the 1980s, which creates a carbon plasma on top a substrate onto which the carbon atoms deposit to form diamond [19].

In the diamond lattice, each carbon atom has four valence electrons spread in the *s* and *p* orbitals, the *s* orbital mixes with the three *p* orbitals (p_x, p_y, p_z) forming sp^3 hybridization,

creating a strong tetrahedral structure. This tetrahedral structure gives strength and stability to the bonds.

In the graphite lattice, the *s* orbital mixes with only two *p* orbitals forming three sp^2 orbitals pointing to vertices of a triangle in a plane. Three electrons occupied these orbitals and together with the one electron left in the *p* orbital perpendicular to the sp^2 plane contribute to conduction. Overlapping between sp^2 orbitals of neighboring atoms in the same plane occurs, also overlapping with their hybridized *p* orbital resulting in π bond. The whole structure is made of sheets held together by weak Vander Walls forces, separated by a distance 3.40 Å giving softness structure [20-22].

Bridging between these two main allotropes of carbon (diamond and graphite) lies a whole variety of carbon materials, which include, among others, amorphous sp^2 bonded carbon (such as thermally evaporated carbon, glassy carbon and nanodiamond films) and sp^3 bonded carbon (sometimes referred to as amorphous diamond).

Another polymorphic form of carbon was discovered in 1985 [23]. It exists in discrete molecular form, and consist of a hollow spherical cluster of carbon atoms. Each molecule is composed of groups of sixty and more carbon atoms, bonded one to another, making both hexagonal and pentagonal geometrical configurations [Figure 1.5]. The material composed of C_{60} is known as buckminsterfullerene. The C_{60} units form a crystalline structure and pack together in a face centered cubic array [24-25].

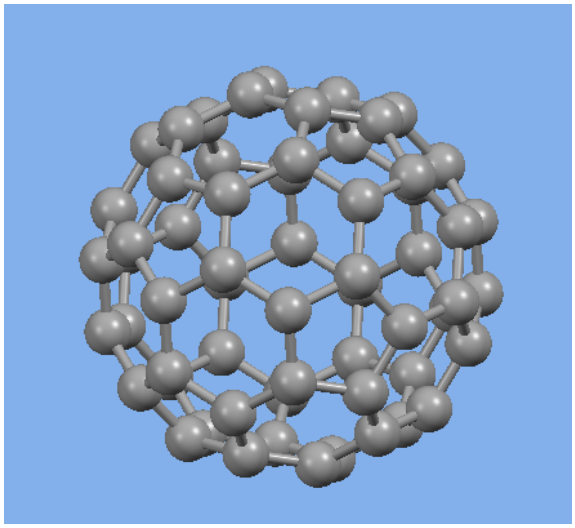

Figure 1.5: The Buckminsterfullerene C_{60}

The discovery that carbon could form stable and ordered structures other than graphite and diamond, stimulated researchers worldwide to search for the other new forms of carbon. Sumio Iijima discovered fullerene-related carbon nanotubes in 1991. The bonding in carbon nanotubes is sp^2, the tubes can therefore be considered as rolled-up graphitic sheets [26].

Carbon nanotubes exhibit extraordinary strength and unique electrical properties, and are efficient conductors of heat, that make them potentially useful in a wide variety of applications in nanotechnology, electronics, optics and other fields of material science.

Atomic carbon has an atomic number of 6 and $1s^2 2s^2 2p^2$ electronic ground state configuration. The carbon atom's electronic configuration is believed to change its ground state in diamond as introduced above. If a carbon atom enters into structure of diamond its two 2*s* and 2*p* electrons, redistribute into four new equal-energy-level orbitals called $2(sp^3)$ hybrid orbitals. It requires a loss of energy, but a very profitable covalent bonding compensates this effect. The angular distribution of the wave functions for these four $2(sp^3)$ orbitals can be illustrated by drawing four loves whose axes are at 109.5° to each other, the axes of these lobes thus extend towards the corners of an imaginary tetrahedron centered around the carbon atom Figure 1.6.

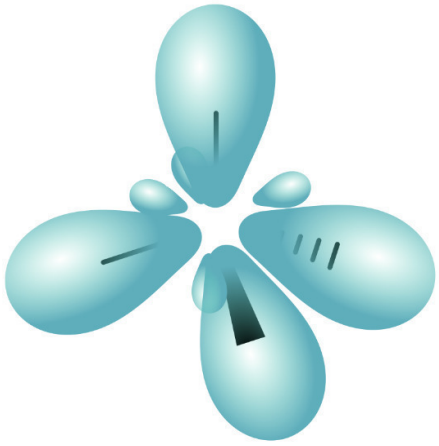

Figure 1.6: Representation of sp3 hybridization

Quantum Mechanics (QM) calculations indicate that greater overlap between orbitals results in a stronger covalent bond. The diamond structures represent a three dimensional network of strong covalent bonds, which explains why diamond is so hard. The diamond structure. Figure 1.7 is cubic whit an edge length of $a_0 = 3.567$ Å and can be viewed as two interpenetrating Face Centered Cubic (FCC) structures displaced by (¼, ¼, ¼)a_0. The diamond crystal is highly symmetric with a cubic space group O_h^7 [24]. Since all the valence electrons contribute to the covalent bond, they are not free to migrate through the crystal and thus, diamond is a poor conductor with a bandgap of 5.6 eV for unstressed diamond for the fundamental gap and 7.5 eV for the direct gap [27-28].

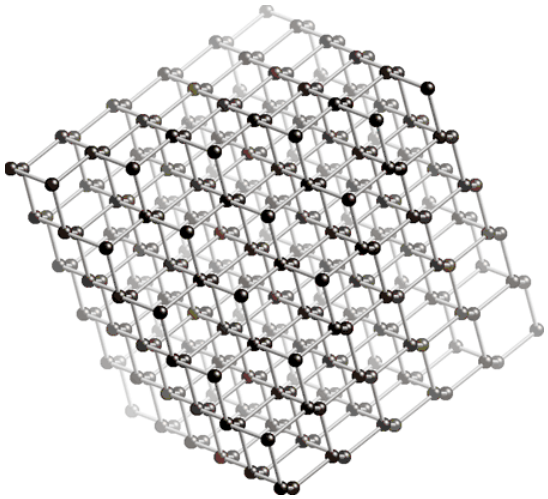

Figure 1.7: Diamond lattice: this figure shows how the tetrahedral are linked in space

In other hand, for the graphite structure three of the two 2*s* and two 2*p* electrons in carbon´s ground state redistributes into three hybrids 2(sp^2) orbitals which are a mathematical mixing of the *s* orbitals with two of the three *p* orbitals. The angular probabilities for these 2 (sp^2) orbitals can be represented by three coplanar lobes at 120° to each other. The fourth electron of the original two 2*s* and two 2*p* electrons fills that *p* orbital which does not participate in the 2(sp^2) hybrid, the lobe for this *p* orbital being perpendicular to the plane defined by the three 2(sp^2) orbitals, as shown in Figure 1.8.

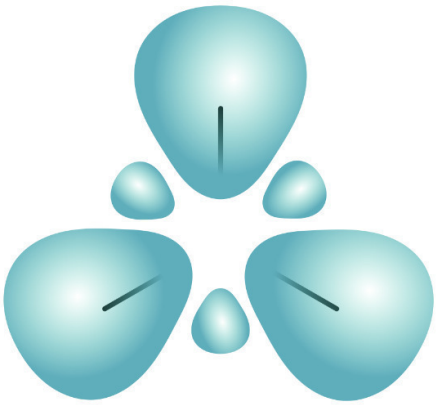

Figure 1.8: Representation of sp2 hybridization

In the graphite structure, overlap occurs between the 2(sp^2) orbitals of neighboring atoms in the same plane. For such neighbors a side-to-side overlap also occurs between their hybridized *p* orbitals. A side-to-side bonding known as π-bonding results between these neighbors. The electrons participating in this π-bonding seem able to move across these π-

bonds from one atom to the next. This feature explains the graphite´s ability to conduct electricity along the sheets of carbon atoms parallel to the (0001) direction. The in-plane nearest neighbor distance is 1.421 Å normal to (0001), adjacent sheets of carbon atoms are held together by the weak Van der Waals bonds and separated by a distance 3.40 Å . This gives softness to the structure [29-32]. The crystal structure is described by an hexagonal lattice with D_{6h}^4 space group. Balls and sticks model stacked graphite with highlighted the unit cell composed of 4 atoms is shown in Figure 1.9.

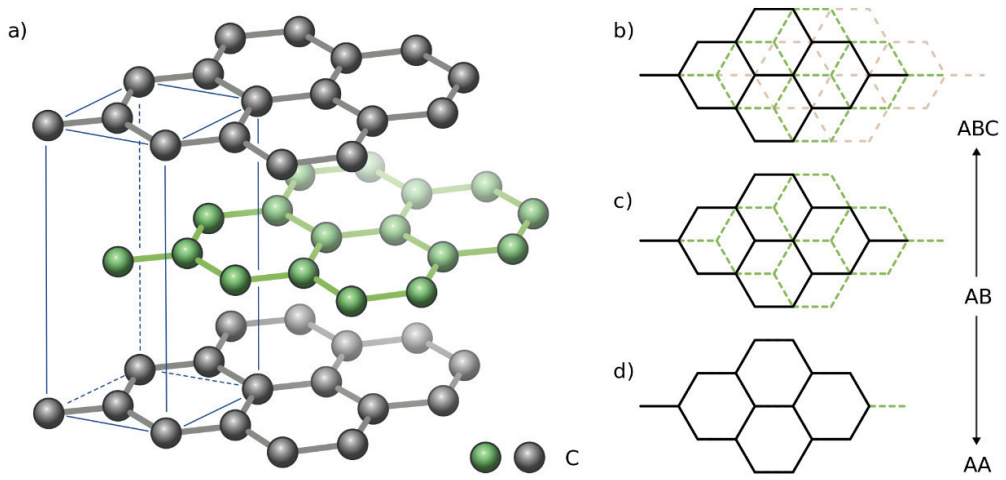

Figure 1.9: Graphite model a) in perspective at left panel. The right panel displays a schematic top view of the structure with various layer stockings: b) ABC stacking, c) most stable AB stacked graphite and d) AA stacking.

Finally, the amorphous structure is characterized by a high degree of short-range order and the absence of long-range order. The short-range order in amorphous structures can be seen in bond length, number of nearest neighbor atoms as well as in the angle between two bonds. At a longer range, there is no periodicity in the amorphous structure; hence, its symmetry is broken, giving isotropic characteristics to the structure.

Energetically, atoms in the amorphous structure are not bonded ideally hence, the energy of the amorphous structure is higher than of a pure crystal. An example of amorphous model is shown in Figure 1.10.

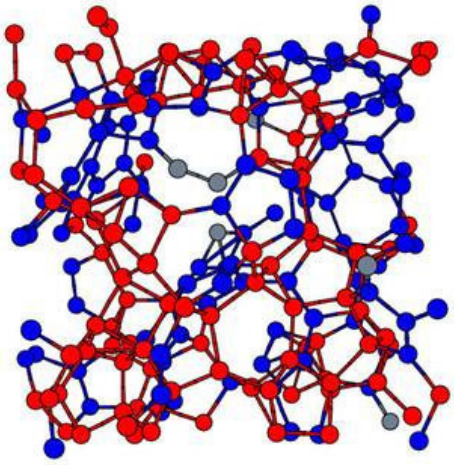

Figure 1.10: Amorphous carbon model. Red, blue and grey spheres are the sp^4, sp^3 and sp^2 atoms, respectively

The method of preparation of amorphous diamond strongly affects the properties of the structure. Two specific amorphous forms of carbon commonly appear and can be distinguished by their microscopic and macroscopic properties:

1. Diamond-like amorphous carbon, usually denoted by $ta-C$. This $ta-C$ is hard, dense material mostly made of distorted sp^3 bonds
2. Graphite-like amorphous carbon, usually denoted by $a-C$. This $a-C$ is a soft, opaque material mostly made of distorted sp^2 bonds.

1.3 Graphene

Carbon is chemically versatile, readily bonding with other elements to form a plethora of complex molecular structures. Carbon atoms can link with each other either tetrahedrally to form diamonds, or more commonly, in layers with a chicken-wire structure, graphite. The hexagonally arranged carbon-carbon bonds are rich in electrons, making the graphite conduct well along the layers. In recent decades, researchers have made new versions of graphite in which the layer's curl round into nanometer-sized balls (fullerenes) or roll up into tubes-carbon nanotubes, which have demonstrated technological promise. Graphene, however, consists of just a single-layer of graphite.

Graphene is the thinnest and strongest material ever isolated, and its electronic properties are quite different from those of graphite, nanotubes and the fullerenes. The electrical charge carriers in graphene move, unimpeded, at speeds 10–100 times faster than in today's silicon chips and at normal temperatures. Furthermore, graphene is stable in air,

transparent and flexible. Being carbon, the source material should be cheap and plentiful. It is not surprising that industry is excited by graphene's technological potential [33].

Graphene offers the seductive prospect of fast, nanoscale electronic devices. However, making and manipulating graphene is a daunting task, and the techniques are not yet in place to fabricate devices commercially. As in semiconductors, the electrical current is transported by either negative charge carriers' electrons) or the positive "holes" that they leave behind. Unlike conventional electrons and holes in semiconductors, graphene's charge carriers travel over hundreds of nanometers at a speed that is only 300 times slower than that of light [34-36].

Graphene is a one-atom-thick planar sheet of sp^2 bonded carbon atoms that are densely packed in a honeycomb crystal lattice. The sp^2 hybridization between one $2s$ orbital and two $2p$ orbitals leads to a trigonal planar structure and the carbon-carbon bond length in graphene is approximately $1.42\,\text{Å}$ [37-38]. Graphene is the basic structural element of all carbon allotropes including graphite, carbon nanotubes and fullerenes. Perfect graphenes consist exclusively of hexagonal cells; pentagonal and heptagonal cells constitute defects. A graphene model can be seen in Figure 1.11.

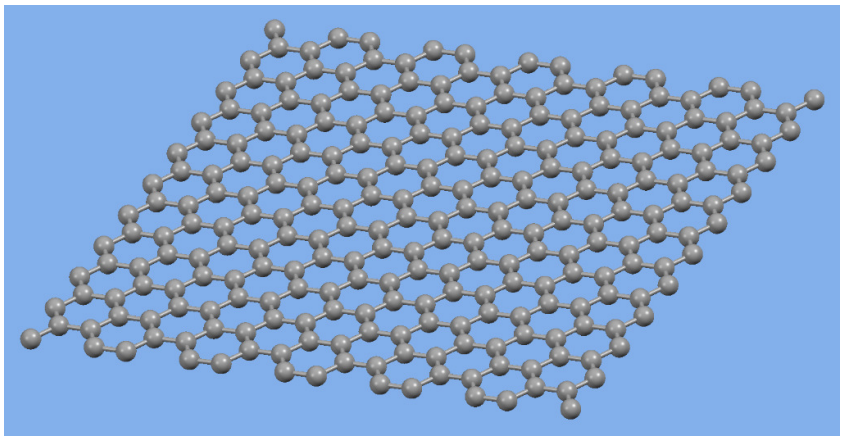

Figure 1.11: One Graphene sheet

The bonding orbitals have a filled shell and, hence form deeper valence band levels. The $2p_z$ orbitals on the neighboring carbon atoms are perpendicular to the planar structure of the graphene layer and can bind covalently, leading to the formation of a band.

The unique property of the electronic structure of graphene is that the π and π^* bands touch at a single point at the Fermi energy (E_F) at the corner of graphene's hexagonal Brillouin zone, and close to this so-called Dirac point the bands display a linear dispersion and form Dirac cones [38] [Figure 1.12]. Thus, undoped graphene is a semimetal ("zero gap

semiconductor"). The linear dispersion of the bands mimics the physics of quasi-particles with zero mass, the so-called massless Dirac fermions. The fascinating electronic and transport properties of graphene [37-39] make it to a point of focus not only in fundamental research but also in applied science and technology with a vision to implement graphene in a myriad of electronic devices replacing the existing silicon technology.

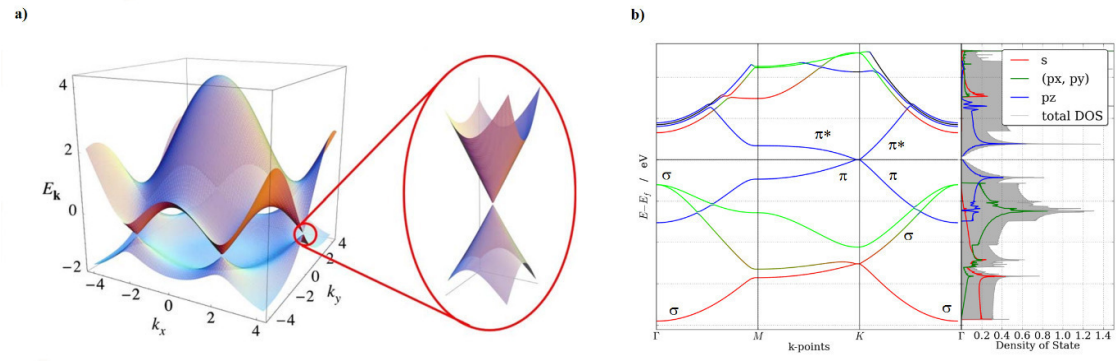

Figure 1.12: a) Electronic dispersion of π and π^* states in the honeycomb lattice of free-standing graphene. b) Band structure of free-standing graphene (σ, π and π^* bands are marked) [46]

Despite the fascinating recent achievements in graphene production, the second problem of controllable doping should be solved prior to being able to implement graphene in any kind of electronic device. Several strategies exist, which allow the modification of the electronic structure of graphene, including:

1. Fabrication of narrow, straight-edged stripes of graphene, so-called nanoribbons [40-41],
2. Preparation of bilayer graphene [42-43],
3. Direct chemical doping of graphene by an exchange of a small amount of carbon atoms, by nitrogen [44], boron [45] or transition-metal atoms [46];
4. Modification of the electronic structure of the graphene by the interaction with substrates [45–49];
5. Intercalation of materials underneath graphene prepared on different substrates [50-55];
6. Deposition of different materials on top of graphene [56-58]. Not surprisingly, the investigation of graphene interaction with supporting or doping materials, which may provide an additional important degree of control of graphene properties, has become one of the most important research fields [59-62]

Two common methods of graphene preparation on metallic surfaces exist:

1. Elevated temperature segregation of the carbon atoms to the surface of a bulk metallic sample, which was doped with carbon prior to the treatment [Figure 1.13 a]; and
2. Thermal decomposition of carbon-containing molecules on the surface of transition metals (TMs) [Figure 1.13 b].

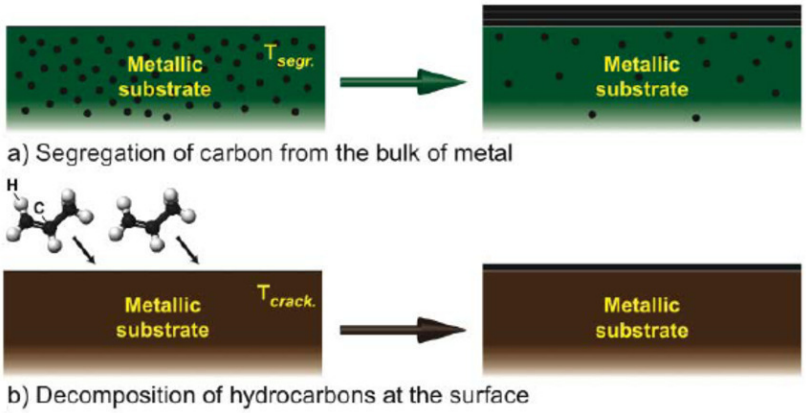

Figure 1.13: Two ways of the graphene preparation on metal surfaces: a) Segregation of bulk-dissolved carbon atoms to the surface at high temperature T_{segr}; b) Decomposition (cracking) of hydrocarbon molecules at the surface of transition metals at high temperature T_{crack} [62]

In the first method, the transition-metal sample with some amount of carbon impurities or the bulk crystal previously loaded with carbon (via keeping the sample at elevated temperature in the atmosphere of CO or hydrocarbons) is annealed at higher temperatures. This procedure leads to the segregation of carbon atoms to the surface of the metal. Careful control of the temperature and the cooling rate of the sample allow varying the thicknesses of the grown graphene layer: monolayer versus multilayer growth.

The second method involves the thermal decomposition (cracking) of carbon-containing molecules at a metal surface. Light hydrocarbon molecules, such as ethylene or propene, are commonly used, but the successful decomposition of CO, acetylene, and of heavy hydrocarbon molecules, such as cyclohexane, n-heptane, benzene, and toluene, was also demonstrated [47]. Molecules can be adsorbed on a metal surface at room temperature, and then annealing of the sample leads to the decomposition of molecules and hydrogen desorption. Alternatively, the hot sample surface can be directly exposed to precursor molecules, which decompose at the sample surface. Recent experiments demonstrate that both methods,

segregation and decomposition, lead to graphene layers of similar quality. In the case of segregation, the kinetics of single graphene layer formation is defined by a careful control of the annealing temperature (but multilayers of graphene could also be prepared). In the second method, the graphene thickness is naturally restricted to a single-layer due to the fact that the chemical reaction on the catalytically active metallic surface takes the place. Thus, the speed of hydrocarbon decomposition drops down by several orders of magnitude as soon as the first graphene monolayer is formed [63-64].

Graphene also provides a way of examining quantum phenomena in two dimensions. For example, a magnetic field applied perpendicularly to a current flowing in the plane of a 2D conductor, induces a transverse voltage, that increases in discrete quantum steps – the quantum hall effect. In metals, it appears only at very low temperatures, but in graphene it can be observed under ambient conditions, which indeed confirms its single-layer status. Furthermore, two new types of the quantum Hall effect were observed, which correspond to two different kinds of quasiparticles, one found in graphene and one in a bilayer of graphene

1.4 Carbon nano-onions

Recently, materials chemistry has been one of most intensively developing fields of science. It mainly involves the synthesis of new materials or the modification of their surfaces so that new properties can allow for their practical application. Much attention has been devoted to nanoparticles, which can form bigger micro- and macromolecular systems.

Carbon materials have always been at the focal point of energy applications. The emergence of new carbon nanohorns, foremost carbon nanotubes and graphene, has propelled research related to electrochemical energy storage and conversion, leading to what has been coined the *carbon new age* [65]. Among all carbon nanohorns and allotropes, carbon onion are one the most interesting. Carbon onion (CO), also called onion-like carbon (OLC), onion-like-fullerenes (OLFs) or carbon nano-onions (CNOs), are nanoscopic carbon particles, with a nearly spherical shape made of multiple enclosed fullerene-like carbon shells.

Carbon onions can be defined by virtue of their structure as *spherical* or *polyhedral* carbon nanoparticles, often smaller than 10 nm, consisting of several fullerene-like carbon shells enclosed in a *Russian doll* [66-68] manner which are defective and disordered to a certain degree [69]. This distinct multilayer architecture is also name-giving feature of CNOs. From vacuum-deposited amorphous carbon films, Iijima observed CNOs for the first time in 1980 [70]. He presented electron micrographs of small spherical particles of graphitized carbon,

whose sizes varied between 30 and 70 Å in diameter. Five years later, C_{60} was discovered by Smalley and co-workers [23]. In 1987 Iijima realized that the innermost shell of the CNOs he observed in 1980 had a diameter of 8 Å and therefore, it could be C_{60} [71]. In 1992 Ugarte [72] obtained CNOs by intense irradiation of carbon soot. The Figure 1.14 shows some CO features.

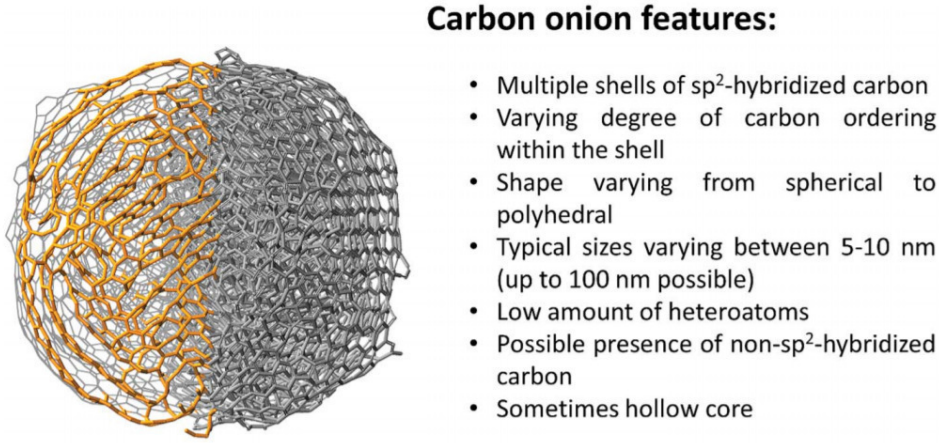

Figure 1.14: Typical features of COs [73]

Carbon onions are a rather novel addition to the carbon materials family. Depending of their synthesis method and the synthesis parameters, the resulting carbon onion differs in size, chemical composition, phase and morphology. These multi- shell fullerenes are conglobated by spherical or polyhedral concentric shells of carbon atoms, ranging from either double- and triple-shelled to multilayered structures and typically ranging from 4 to 25 nm in size.

So far, there is no consistent nomenclature for carbon onions in the literature [73]. Consistent nomenclature is a notorious issue throughout the entire field of nanocarbons, especially it comes to rather new carbon structures [74]. Most, reports often interchangeably, use either *carbon onions* (CO), *carbon nano-onions* (CNOs) or *onion-like-carbon* (OLC). All there are not in agreement with the nomenclature for sp^2-hybrized carbon nanoforms by Suarez-Martinez, Grobert and Ewels [69]. They suggest consistently calling carbons with an *onion* structure multi-wall fullerene. This unifying nomenclature employs a purely geometrical classification, independent of the state of carbon ordering (defects, particle size and shape) or synthesis method. When considering very large structures referred to as carbon onions with size more than 100 nm and a high defect density, the conceptual description as fullerene, normally applied to molecules, may be arguable. Also compared to carbon nanotubes (CNTs), the differentiation between single-, double-, few- and multi-wall architectures is not practical for carbon onions: almost all carbon onions qualify as multi-wall structures. Based on consideration similar to those used in the nomenclature of CNTs, it suggests the application

of the term CNOs only to those carbon particles that have at least 4 shells (lake multi-wall CNTs) a size smaller than 100 nm, spherical or polyhedral shape, and partially defective structure (amorphous domains, or islands of sp^3-hybridized carbon) [73]. The distinct structural characteristic defining carbon onions should be the clearly visible multi-shell character. This nomenclature also includes hollow CNOs (hollow-core) and CNOs with core (*e.g.* metal clusters or residual nanodiamond remaining inside of the carbon onion due to incomplete transformation). Finally, the European Union may considerer adopting a size dependent differentiation between CO (in general) and CNOs, with the latter referring to carbon onions smaller than 10 nm. This suggestion is motivated by the differentiation between nanodiamonds and single-digit nanodiamonds, with the latter covering the range bellow 10 nm [75]

Carbon nanostructures including fullerenes, CNTs, nanocones, nanopeapods, nanotorii and carbon onions have received much attention because of their unique properties, such as their high flexibility, their high thermal conductivity and they are presently the strongest material know [76]. This carbon nanostructures made of concentric graphitic shells, owing to their curvature, moderately high specific surface area of $\sim 500 \mathrm{m}^2/\mathrm{g}$, and electrical conductivity of $\sim 4\ \mathrm{S/cm}$, are attractive for high power applications because of their high charge-discharge rate capabilities [77].

CNOs are a member of the fullerene family, and they consist of quasi-spherical- and polyhedral shaped graphitic layers close to one another. The diameter of the CNOs nanomaterial depends of the synthetic protocol, but nevertheless, CNOs exhibit in general a high area to volume ratio [68].The distance between the graphitic layers is 0.335 nm in agreement with experiments [78] which suggest a distance of ~ 0.336 Å, and it is approximately equal to the distance between two graphitic planes (0.334 nm) [79]. Moreover, the π states near the HOMO-LUMO gap and more strongly bound σ states have also a similar character as the corresponding states in graphite [80]. In a report from 1995, Ugarte refers to CNOs as onion-like graphitic particles, which display a wide range structures, explicitly including polyhedral to nearly spherical morphologies in his definition of CNOs [81]. The OLCs polygonised shells contains fullerene-like spheres with twelve pentagons, which preferentially responsible for the formation of polygonised structure. It is worth to mention, that in some reports the authors utilize the term OLCs, when referring to CNOs. The structure of CNOs contains hexagonal and pentagonal rings with carbon atoms located at the vertices forming two single bonds and one double bond with neighboring carbon atoms with delocalized π-electrons across the molecule [82-83]. Graphitic layers in the structure of this

nanomaterial consist of a significant number of defects and holes [84]. The holes can be filled in a variety of ways with heptagonal and pentagonal carbon rings, creating amorphous or crystalline quasi-spherical onions [85]. However, CNOs discovered by Iijima in 1980 [70], did not garner as much interest as carbon nanotubes (CNTs) discovered at the same time. The Figure 1.15 shows spherical and polyhedral fullerenes and double layer CNOs.

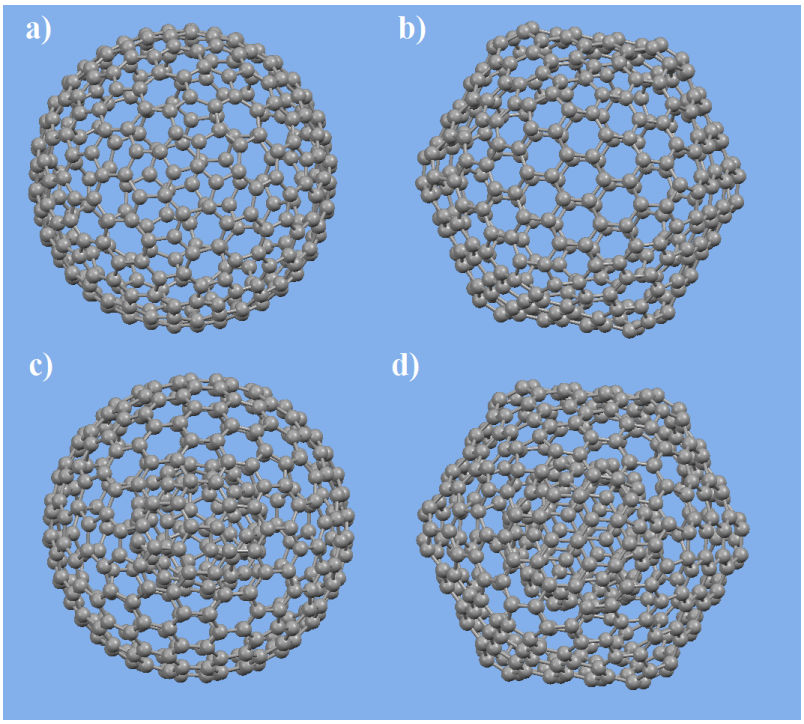

Figure 1.15: Fullernes and double layer CNOs: a) C_{320} spgerical fullerene, b) C_{320} polihedral fullerene, c) $C_{60}@C_{240}$ double layer spherical CNOs and d) $C_{80}@C_{320}$ double layer polihedral CNOs

Transmission electron microscopy (TEM), electron energy loss spectroscopy (EELS), Raman Spectroscopy and scanning electron spectroscopy (SEM) are generally used to characterize CNOs. Of these, Raman spectroscopy is the most useful non-destructive technique capable of differentiating between these various structures [86-90]. High-resolution transmission electron spectroscopy (HRTEM) has been widely employed to visualize CNOs and to study the mechanism of CNO formation and their structural properties [Figure 1.16]. Raman spectroscopy is another useful technic for the structural characterization of CNOs and corroborates the basic graphical structure of COs [67]-[91-93].

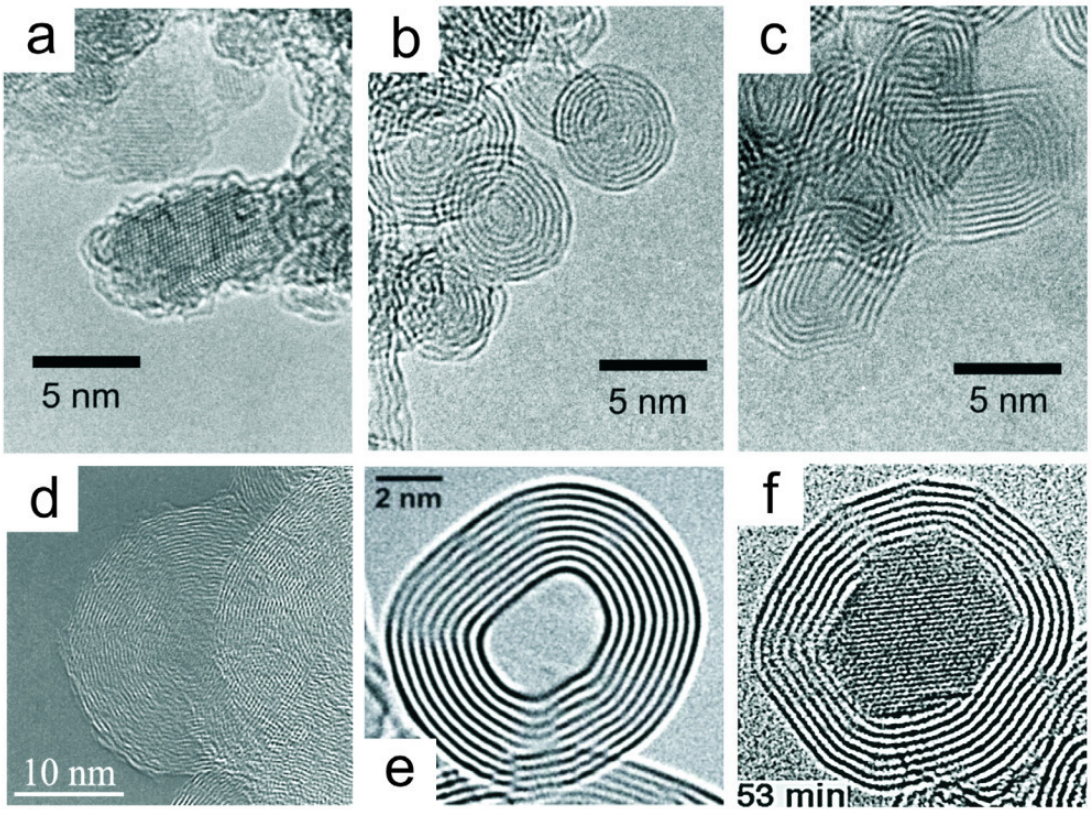

Figure 1.16: HRTEM images, high-resolution of a) NDs, b) sphericla small CNOs, c) polihedral CNOs, d) spherical big CNOs, e)spherical hollow-core CNOs, and f) metal-core CNOs [94]

Electronic structure calculations of fullerenes suggest that they are semiconducting [95]. On the contrary, multi-shell fullerenes have a decreasing HOMO-LUMO gap with increased size [96-97]. Electronically, the CNOs structure is metallic with a large pseudo-gap near the Fermi energy. This is an agreement with conductivity measurements [78]. While a $N \sim 730$ carbon atom multi shell defect less fullerene in seen to be semiconducting with a gap slightly less than 1 eV [97].

Different methods can be used for the synthesis of carbon onions, such as decomposition of carbon-containing precursors, including combustion and detonation methods [98–105], mechanical milling [106-107], carbon ion implantation [108-109], underwater arc discharge between graphite electrodes [110-112], annealing of acetylene black in the presence of an iron catalyst [113] or heating of a carbon filament in liquid alcohol [114]. Alternatively, carbon onions can also be derived via phase transformation of nanodiamonds by annealing in vacuum [115-120], argon [121-124], nitrogen [125], hydrogen [126] or helium [127-130] [Figure 1.17] (slight variations occur depending on the annealing atmosphere, especially when

comparing vacuum with an inert gas atmosphere), plasma spraying of nanodiamonds [131], laser irradiation of nanodiamonds in liquid alcohol [132], electron beam irradiation of carbon materials[72]-[133-134] or direct plasma treatment of coal [135].

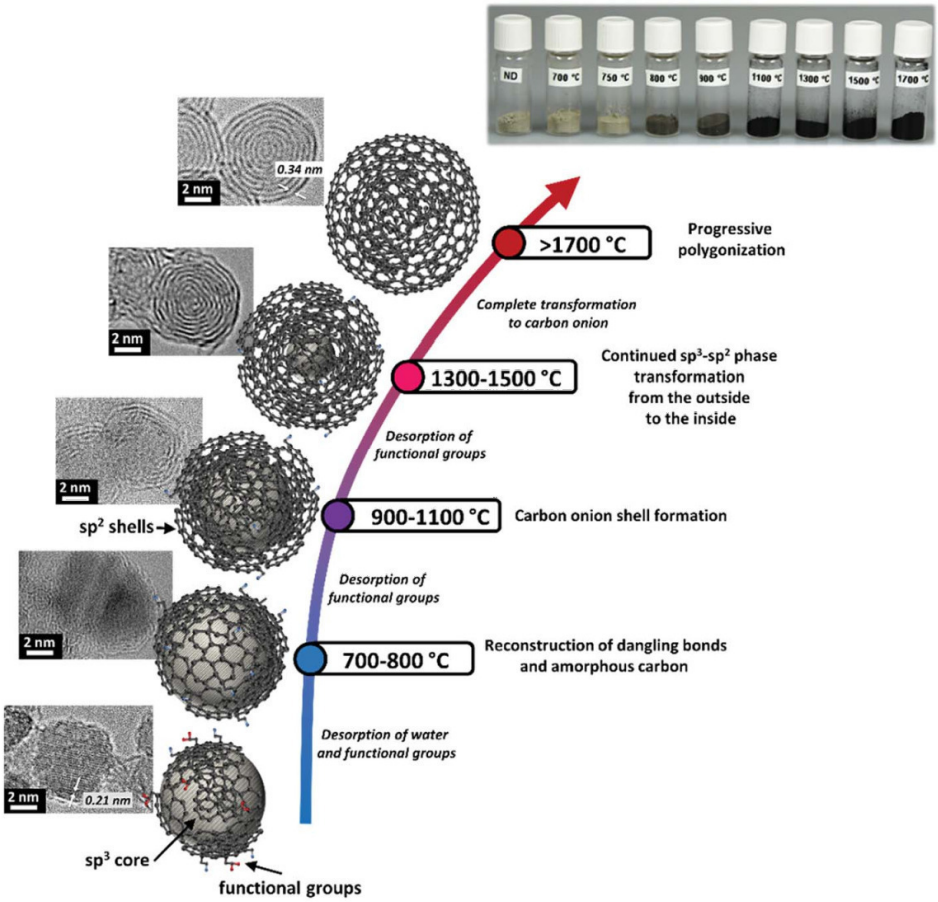

Figure 1.17: Transformation from nanodiamonds to COs by annealing show using transmission electron micrographs, optical images, schematic illustrations of intermediate steps, and the assignment of physical effects depending on the annealing temperature [73]

The type of precursor and the synthesis conditions have a strong impact on the structure, as seen from transmission electron micrographs of different types of carbon onions given in Fig. 1.18, but all carbon onions share the multi-shell fullerene-like architecture.

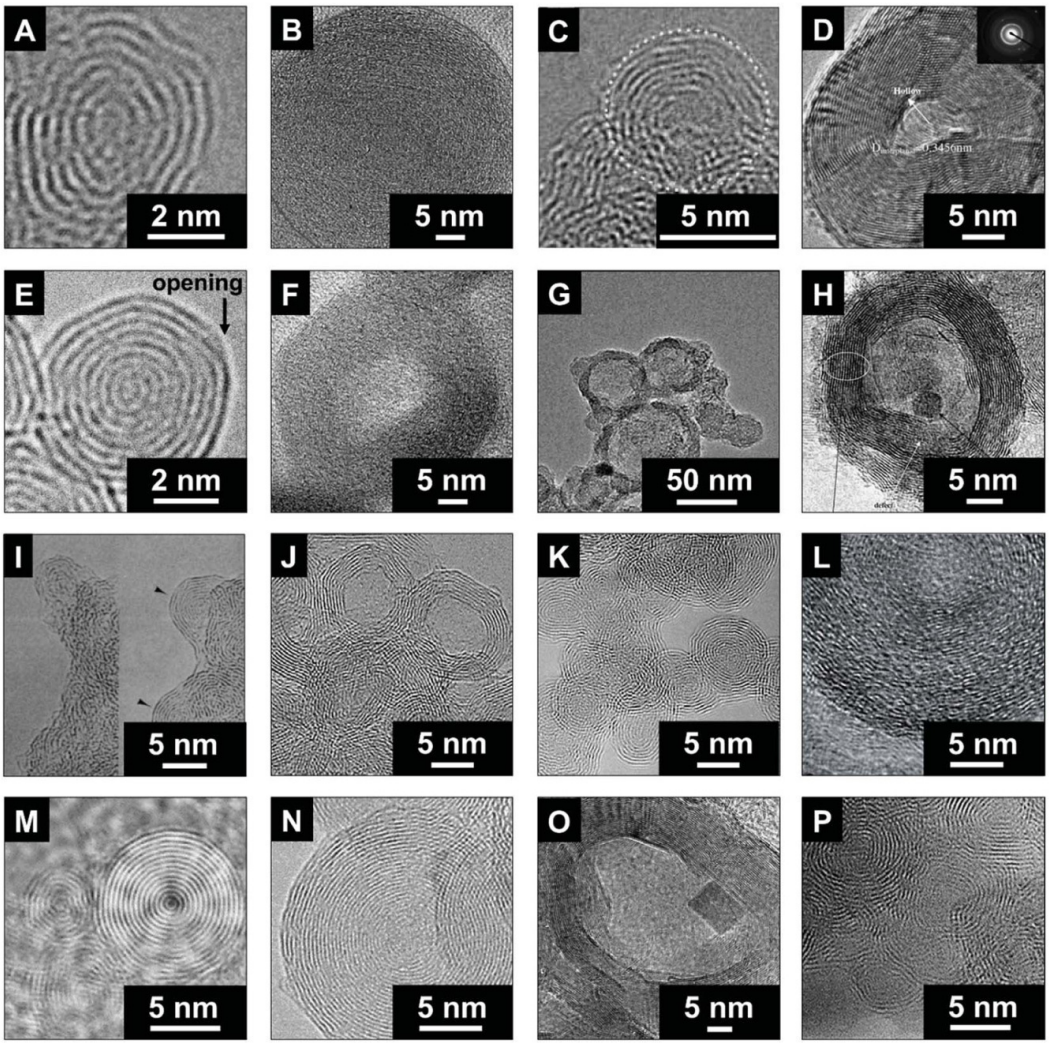

Figure 1.18: Transmission electron micrographs of carbon onions synthesized using different methods: (A) counterflow diffusion flame method, (B) pyrolysis of naphthalene, (C) laser-assisted combustion process using C_2H_4 and O_2, (D) catalytic decomposition of C_2H_4 on Ni/Al, (E) annealing of nanodiamonds, (F) carbonization of phenolic resin in the presence of ferric nitrate, (G) thermolysis of a NaN_3–C_6Cl_6 system under argon or air atmosphere, (H) annealing of acetylene black in the presence of ferric nitrate, (I) electron-beam irradiation of amorphous carbon, (J) radio frequency plasma treatment of coal, (K) laser irradiation of nanodiamonds in liquid alcohol, (L) burning ghee, (M) arc discharge between graphite rods in water, (N) carbon ion implantation in copper and silver, (O) ball milling of graphite, (P) chemical vapor deposition using BCl_3, C_2H_2, and H_2 [73]

In 1992, Ugarte observed the formation of carbon onions during electron beam irradiation of amorphous carbon particles in a (TEM) [136]. Due to irradiation-stimulated graphitization, amorphous carbon can be transformed to nanometer-sized carbon onions with

clearly visible nucleation centers (Figure 1.18I). While scientifically intriguing, this method is limited in terms of the yield of synthesized carbon onions [136]. The production of carbon onions via decomposition of carbon-containing precursors like CH_4 in the presence of Ni/Al composite catalysts (Figure 1.18D) can be accomplished at rather moderate temperatures of 600 °C in hydrogen [98]. The resulting carbon onions showed a hollow structure with several carbon shells and a diameter larger than 30 nm. The catalytic decomposition enabled the formation of carbon onions with a metallic core. Hou et al. used a counterflow diffusion flame method (Figure 1.18A) to obtain carbon onions on a nickel catalyst [99]. By mixing ethylene, methane, nitrogen, and oxygen, it was possible to control the yield as well as the size of carbon onions [98]. These synthesis methods, together with boron-doped carbon onions from chemical vapor deposition (Figure 1.18P) [137], the carbonization of phenolic resin with ferric nitrate (Figure 1.18F) [102], and carbon ion implantation in copper and silver (Figure 1.18N) [103], present facile ways for the production of carbon onions, but may be disadvantageous due to a high amount of heteroatoms in the product. In a study by Choucair et al. (Figure 1.18B), high purity carbon onions with more than 90 mass % of carbon and no metal impurities were produced by a catalyst-free flash pyrolysis of naphthalene [100]. The particles of *ca*. 50 nm diameter were composed of highly defective carbon shells, as shown by Raman spectroscopy and TEM. Gao et al. (Figure 1.18C) used a laser-assisted combustion of C_2H_4 in air [138]. The resulting high purity carbon onions with a diameter of *ca*. 5 nm exhibited a high degree of sintering and the KOH activated materials showed a promising super capacitor performance with a capacitance of up to 126 F g^{-1} in 2 M KNO_3 and a relatively high surface area of up to 804 m^2 g^{-1} [138].

Underwater arc discharge-derived carbon onions (Figure 1.18M) [111], and nanodiamond-derived carbon onions (Figure 1.18E) have been evaluated as electrodes for supercapacitors. [78]- [139-140]. The advantages of these two synthesis methods are the high yield, the high purity, and the better controllability and reproducibility. Yet, not all synthesis routes reported in the context of carbon onion synthesis actually yielded carbon onions as defined above. For example, Fan et al. synthesized carbon particles by heating carbon in liquid alcohol; these particles had a nanoscopic size of 50 nm, but without a multi-shell structure [114]. Structurally, such carbon nanoparticles are virtually indistinguishable from carbon black. Bystrzejewski et al. used the thermolysis of a NaN_3–C_6Cl_6 mixture to produce different types of carbon onions (Figure 1.18G) [103]. In some of their experiments, the multi-shell structure was clearly produced, but large amounts of carbon byproducts were generated, too

[102]. The same was observed by using ball milling of graphite published by Chen et al. (Figure 1.18O) [107].

Due to the unique physicochemical properties of CNOs, these nanostructures are used in many areas, mainly in electronics [141-143], in optical limiting [144], in catalysis [145-146], in energy conversion and storage [147], in Li-ion electrochemical energy storage devices [148-149], as hyper lubricants [150-152], for sensors [153-154] and for biological and environmental applications [68-156]. One of the most interesting physical properties of CNOs is their conductivity. CNOs formed from nanodiamond particles at high temperatures (1800 °C) have showed his best performance in terms of conductivity. Some studies showed that electron conduction through the junctions occurs by a super exchange mechanism, and the conductance of the CNOs is approximately 71.8 lS, which is close to the metallic behavior [157]. The next very interesting application of CNOs is their catalytic performance. Keller et al. published a study showing the potential of CNOs as catalysts for this reaction with high conversion levels (up to 92%). From these studies, the authors concluded that the catalytic activities depend mainly on the high surface area of CNOs and their functionalities.

Doping of carbon materials with donors or acceptors can improve the electronic performance of CNs [158]. Boron-doped materials with low contents of B (2 wt%) in comparison to other reported heteroatom-doped carbon materials show better physicochemical characteristics and can be applied in semiconductors, quantum dots, supercapacitors and batteries [159]. Properties of cathode materials, such as specific surface area, morphology, porosity and surface chemistry, play a significant role in the charging behavior and the cycling performance of Na-O2 batteries [160]. The influence of heteroatoms on the catalytic activity of carbons was interpreted in terms of semiconductor properties. N-doped onion-like carbon materials were also applied as catalysts for catalytic ORR in photon-exchange-membrane fuel cells [161].

Carbon nano-onions with metal oxide cores, such as Co_3O_4 [162] and NiO [163], are great candidates as anode materials for lithium ion batteries due to their improved electrochemical and cyclic performance, high reversible capacity, safety [161], excellent discharge capacity and high rate charge-discharge capability [164]. The spherical structure of CNOs also allows for use in tribological studies [108]- [150-151]. These studies have been conducted mainly with ‘‘small” CNO structures. Hirata et al. examined balloon-disc-type friction testing of the tribological properties of CNOs. Their studies showed that CNOs exhibited a low, stable friction coefficient (<0.1) both in air and in vacuum at room

temperature, which was lower than graphite powder [151]. Both experimental and computational investigations clearly showed that CNOs used as lubricant additives led to a strong reduction of friction and wear, even at low temperatures, due to rolling and sliding processes inside the contact area [153]. The high surface areas of CNOs play a main role in many areas of their potential uses. Oxidized CNOs were used as platforms for the adsorption of heavy metal ions [164]. Drug targeting applications frequently requires developed surface areas and nontoxicity of nanoparticles. Investigations concerning cytotoxicity and resulting biological and medical applications of CNOs are also very promising. CNOs, oxidized CNOs and PEGylated nanostructures over a wide range of concentrations. This study also showed that CNOs can be used as a platform for the immobilization of biomolecules while keeping their bioactivity. This showed that these nanoparticles may be applied in magnetic hyperthermia and in cancer therapies with minimum side effects. Due to their efficient cellular uptake, weak inflammatory potential and low cytotoxicity of the fluorophores-functionalized CNOs, these fluorescent derivatives are promising materials for biomedical applications. Another condition necessary for the use of nanoparticles in biosensors is the ability to interact or form chemical bonds with biological compounds without a decrease of biological activity. A biosensor containing CNOs as one of the layers changed the structural properties of the surface, causing reinforcement of the analytical signal.

Chapter 2

Density Functional Theory

2.1 Theoretical Background of DFT

The choice of theoretical and computational procedure strictly depends on the target property that need to be assessed. Moreover, the definition of structural models is another crucial aspect that has to be considered. Quantum Mechanics (QM) approaches allow the evaluation of chemical-physical quantities that could not have been estimated by experimental tests, or only with remarkable inaccuracy. For example, binding energies, molecular electrostatic properties such as dipole, partial charges and electron density distribution, as well as orbital configurations must be evaluated by QM calculations. In addition, QM allows to be free from adjustable or fitting parameters resulting in a general approach. However, as above-mentioned when computational procedures are used particular attention has to be paid to the structural chemical models. Molecular models are dependent on the properties to be assessed and consequently by the computational procedure. For example, QM methods are not applicable to the optimization of macromolecules geometries such as polymers or systems containing thousands of atoms (such as biological systems). Molecular Dynamics (MD) methodologies or Monte Carlo can be used in these cases. However, the MD approaches cannot be used to describe the breaking or/and formation of bonds. Although large structural models cannot be used in conjunction with accurate QM approaches, such as correlated Hartree-Fock [167], Density Functional Theory (DFT) [168] allows obtaining different electronic properties in a relatively short computational time with respect to the mentioned methods. Thus, this theoretical approach is a powerful tool to investigate large chemical systems at QM level [169]. In this thesis DFT calculations were carried out on systems having large number of atoms (up to 700 atoms), and though sometimes high computational time was required, an accurate evaluation of the energies associated with nonco-valent interactions involved in the target systems was achieved. In addition, Molecular Mechanics calculations were carried out on flexible molecules in order to have an accurate description of the conformational space. Since the noncovalent interactions play important role on chemical

systems analyzed in this work, after a brief introduction on the DFT, a section of this kind of interactions will be provided.

The principles of Density functional theory (DFT) are conveniently expounded by making reference to conventional wave function theory [168].

Any problem in the electronic structure of matter is covered by the Schrödinger's equation including the time, but in most cases, this problem is concerned with atoms and molecules without time-dependent interactions: the time-independent Schrödinger equation.

DFT replaces the complicated N-electron wave function Ψ ($\mathbf{x}_1$, $\mathbf{x}_2$, . . ., $\mathbf{x}_N$) which describes a many-electron system and the associated Schrödinger equation by one much simpler electron density $\rho(r)$ and its associated Khon-Sham equation.

For an isolated N-electron atomic or molecular system in the Born-Oppenheimer nonrelativistic approximation, the time-independent Schrödinger equation is given by:

$$\hat{H}\Psi = E\Psi \tag{2.1.1}$$

Where E is the electronic energy, $\Psi(\mathbf{x}_1, \mathbf{x}_2, \ldots, \mathbf{x}_N)$ is the wave function, and $\hat{H}$ is the Hamiltonian operator,

$$\hat{H} = \hat{T} + \hat{V}_{ne} + \hat{V}_{ee} \tag{2.1.2}$$

Here.

$$\hat{T} = \sum_{i=1}^{n} \left(-\frac{1}{2}\nabla_i^2\right) \tag{2.1.3}$$

Is the kinetic energy operator

$$\hat{V}_{ne} = \sum_{i=1}^{n} v(r_i) \tag{2.1.4}$$

Is the electron-nucleus attraction energy operator where $v(\mathbf{r}_i) = -\sum_\alpha \frac{Z_\alpha}{r_{i\alpha}}$ is the 'external' potential acting on electron *i*, the potential due to nuclei of charges Z_α, and

$$\hat{V}_{ee} = \sum_{i<j}^{n} \frac{1}{r_{ij}} \tag{2.1.5}$$

Is the Coulomb electron-electron repulsion energy operator.

$$|\Psi(\mathbf{r}^N, s^N)|^2 dr^N = \text{probablility of finds the system with the position coordinates between } \mathbf{r}^N \text{ and } \mathbf{r}^N + d\mathbf{r}^N \text{ and spin coordinates equal to } s^N \tag{2.1.6}$$

When a system is in the state Ψ, which may or may not satisfy Eq. (2.1.1), the average of many measurements of the energy is given by the formula

$$E[\Psi] = \frac{\langle \Psi | \hat{H} | \Psi \rangle}{\langle \Psi | \Psi \rangle} \tag{2.1.7}$$

Since, furthermore, each particular measurement of the energy gives one of the eigenvalues of $\hat{H}$

$$E[\Psi] \geq E_o \tag{2.1.8}$$

The energy computed from a guessed Ψ is an upper bound to the true ground state energy E_o.

In an electronic system, the number of electrons per unit volume in a given state is the electron density for that state. This quantity will be of great importance in the DFT. Is a nonnegative simple function of three variables, *x*, *y* and *z*.

In the Hartree-Fock method the N-electron wave function of the system can be approximated by a Slater determinant of N mono electron orbitals depending on the single electron position.

$$\Psi_{HF} = \frac{1}{\sqrt{N!}} \begin{vmatrix} \Psi_1(\mathbf{x}_1) & \Psi_2(\mathbf{x}_1) & \dots & \Psi_N(\mathbf{x}_1) \\ \Psi_1(\mathbf{x}_2) & \Psi_2(\mathbf{x}_2) & \dots & \Psi_N(\mathbf{x}_2) \\ \vdots & \vdots & & \vdots \\ \Psi_1(\mathbf{x}_N) & \Psi_2(\mathbf{x}_N) & \dots & \Psi_N(\mathbf{x}_N) \end{vmatrix} = \frac{1}{\sqrt{N!}} [\Psi_1 \Psi_2 \dots \Psi_N] \tag{2.1.9}$$

The Hartree-Fock method is a nonlinear "self-consistent-field" method. The energy of the ground state is found in agreement with the **variational principle for the ground state** by minimizing the functional Eq. (2.1.7) subject to the orthonormalization conditions of the mono electron orbitals.

The original idea for the DFT begins with the Thomas-Fermi model in the 1920s. This model establishes that statistical considerations can be used to approximate the distribution of electron in an atom. Thomas (1927) assumes that: "Electrons are distributed uniformly in the six-dimensional phase space for the motion of an electron at the rate of two for each h^3 of volume" and that there is an effective potential field that" is it self-determined by the nuclear charge and this distribution of electrons". If the space is divided into many small cubes (cells), each of side l and volume $\Delta V = l^3$, each containing some fixed number of electrons ΔN (which may have different values for the different cells), the electrons in each cell behave like independent fermions at the temperature 0K, with the cells independent of one another.

The Tomas-Fermi model defines the concept of the *density of states of energy* ε, and using the Fermi-Dirac distribution.

$$f(\varepsilon) = \frac{1}{1 + e^{\beta(\varepsilon-\mu)}} \tag{2.1.10}$$

Which at 0 K reduces to a step function:

$$f(\varepsilon) = \begin{cases} 1, & \varepsilon < \varepsilon_f \\ 0, & \varepsilon > \varepsilon_f \end{cases} \qquad \text{as } \beta \to \infty \tag{2.1.11}$$

Where ε_f is the so-called Fermi energy. All the states with energy smaller than ε_f are occupied and those with energy greater than ε_f are unoccupied. The Fermi energy ε_f is the zero-temperature limit of the *chemical potential* μ. This model also states that each energy level is doubly occupied by one electron with spin α and another with spin β, and besides that the Fermi level ε_f has a relation between total kinetic energy and the electron density $\rho = \Delta N/l^3 = \Delta N/\Delta V$ for each cell in the space (Remember that different cells can be have different values of ρ). This model finally introduces two very important concepts: the famous Tomas-Fermi kinetic energy functional, which Tomas and Fermi dared to apply to electrons in atoms and one the most important ideas in the modern density-functional theory, *the local density approximation* (LDA).

The modern foundation of DFT rests on two theorems by Hohenberg and Kohn that legitimizes the use of electron density $\rho(\mathrm{r})$ as basic variable in place of Ψ ($\mathbf{x}_1, \mathbf{x}_2, \ldots \mathbf{x}_N$). The first theorem states:

The external potential $v(\mathbf{r})$ is determined, within a trivial additive constant, by the electron density $\rho(\mathbf{r})$.

and $v(\mathbf{r})$ is a not restricted to Coulomb potential

Since ρ determines the number of electrons, il follows that $\rho(\mathbf{r})$ also determines the ground-state wave function Ψ and all other electronic properties of the system.

The proof of this theorem shows that a contradiction which is achieved if there are two external potentials, $v(\mathbf{r})$ and $v'(\mathbf{r})$ differring by more than a constant, each giving the same $\rho(\mathbf{r})$ for its ground state. Thus $\rho(\mathbf{r})$ determines N by simple quadrature

$$N = N[\rho[\mathbf{r}]] = \int \rho(\mathbf{r}) d\mathbf{r} \tag{2.1.12}$$

Note that $v(\mathbf{r})$ and hence all properties of the ground state, for example the kinetic energy $T[\rho]$, the potential energy $V[\rho]$ and the total energy $E[\rho]$ ($E_v[\rho]$ shows a explicit dependence of v).

The second theorem provides the energy variational principle:

For a trial density $\tilde{\rho}(\mathbf{r})$, such that $\tilde{\rho}(\mathbf{r}) \geq 0$ and $\int \tilde{\rho}(\mathbf{r}) d\mathbf{r} = N$, $E_0 \leq E_v[\tilde{\rho}]$.

$E_v[\rho]$ is the DFT energy functional expressed as sum of the kinetic energy and electrons-nuclei and electron-electron potential energy:

$$\begin{aligned} E_v[\rho] &= T[\rho] + V_{ne}[\rho] + V_{ee}[\rho] \\ &= F_{HK}[\rho] + \int \rho[\mathbf{r}] v[\mathbf{r}] d\mathbf{r} \end{aligned} \tag{2.1.13}$$

Where

$$F_{HK} = T[\rho] + V_{ee}[\rho] \tag{2.1.14}$$

With $V_{ee}[\rho]$ that can be write as sum of the classical repulsion energy, $J[\rho]$, and a nonclassical term

$$V_{ee}[\rho] = J[\rho] + \text{non classical term} \tag{2.1.15}$$

It is important to observe that $v[\mathbf{r}]$ can express the electrons-nuclei interactions as well as any other type of electrostatic potential.

In 1965 Kohn and Sham invented an ingenious indirect approach to the kinetic functional $T[\rho]$ by introducing orbitals into the problem in such a way as to have an exact kinetic energy component leaving a small residual correction that is handled separately. The Kohn-Sham (KS) method there by turned DFT into a practical tool for rigorous calculations. Furthermore, the Kohn-Sham method use the kinetic energy $T_s[\rho]$ that related to an isoelectronic non-interacting system but the quantity $T_s[\rho]$, although uniquely defined for any density, is still not the exact kinetic energy functional $T[\rho]$ defined before. Thus, to obtain the desired separation out of $T_s[\rho]$, Eq. (2.1.14) must be rewrite as:

$$F_{HK} = T_s[\rho] + J[\rho] + E_{xc}[\rho] \tag{2.1.16}$$

Where

$$E_{xc}[\rho] = T[\rho] - T_s[\rho] + V_{ee}[\rho] - J[\rho] \tag{2.1.17}$$

The defined quantity $E_{xc}[\rho]$ is called the *exchange-correlation energy*; it contains the difference between the kinetic energy of interacting system T and the kinetic energy of the non-interacting system T_s and the nonclassical part of the $V_{ee}[\rho]$.

Assuming differentiability of $E[\rho]$, the variational principle (second Hohenberg-Kohn theorem) requires that the ground-state density satisfy the stationary principle

$$\delta\left\{E_v[\rho] - \mu\left[\int \rho[\mathbf{r}]\ d\mathbf{r} - N\right]\right\} = 0 \tag{2.1.18}$$

which gives the Euler-Lagrange equation

$$\mu = \frac{\delta E_v[\rho]}{\delta\rho[\boldsymbol{r}]} = v[\boldsymbol{r}] + \frac{\delta F_{HK}[\rho]}{\delta\rho[\boldsymbol{r}]} \tag{2.1.19}$$

The ground state electron density is the density that minimizes $E[\rho]$ and hence satisfies Eq. (2.1.19).

It should be noted that the functional F_{HK} depends only on the total number of electrons N of the system (independently of the external potential $v(\boldsymbol{r})$) this means that $F_{HK}[\rho]$ is an *universal functional* of $\rho(\mathbf{r})$; while $E_v[\rho]$ depends on N and on the external potential

$v(\boldsymbol{r})$. Thus, by *N* and $v(\boldsymbol{r})$ the system is completely described by solving the Euler-Lagrange equation.

A useful procedure to obtain the $\rho[\boldsymbol{r}]$ of the ground state energy was given by Kohn and Sham that did not resolve directly the above Euler-Lagrange equation. Orbitals were introduced in the problem and the electron density $\rho[\mathbf{r}]$ was defined through a set of basic functions (atomic orbital basis set, $\phi_j(\boldsymbol{r})$ [167] as

$$\rho(\mathbf{r}) = \sum_{i}^{N} |\psi_i(\mathbf{r})|^2 \tag{2.1.20}$$

Where

$$\psi_i(\boldsymbol{r}) = \sum_{j}^{K} C_{ij}\, \phi_j(\mathbf{r}), \qquad i = 1 \ldots N. \tag{2.1.21}$$

Again, the variational principle ensures that the minimum of the functional $E_v[\rho]$, but this time in the space of $\phi(\mathbf{r})$, is the best approximation of the ground state energy. Therefore, for a given $v_{eff}(\mathbf{r})$ the search of this minimum lead to solve the non-linear *Khon-Sham (KS) orbital equations* [168]:

$$\left[-\frac{1}{2}\nabla^2 + v_{eff}(\mathbf{r})\right]\psi_i(r) = \epsilon_i \psi_i(r) \tag{2.1.22}$$

With

$$\begin{aligned} v_{eff}(\mathbf{r}) &= v(\mathbf{r}) + \frac{\delta J[\rho]}{\delta\rho(\mathbf{r})} + \frac{\delta E_{xc}[\rho]}{\delta\rho(\mathbf{r})} \\ &= v(\mathbf{r}) + \int \frac{\rho(\mathbf{r}')}{|\mathbf{r}-\mathbf{r}'|} d\mathbf{r}' + v_{xc}(\mathbf{r}) \end{aligned} \tag{2.1.23}$$

With $v_{eff}(\mathbf{r})$ is the *KS effective potential* and the exchange-correlation potential $v_{xc}(\mathbf{r})$ is defined as $v_{xc}(\mathbf{r}) = \delta E_{xc}[\rho]/\delta\rho(\mathbf{r})$

2.3 The Hartree-Fock Approximation.

The Hartree-Fock Approximation is important because include the effects of electron correlation. These calculations are important because we can perform calculations (total energies, ionization potentials, equilibrium geometries, dipole moments, etc.) using a

standard hierarchy of basis set (STO-3G, 3-21G*, 6-31G*, 6-31G**, etc.) in molecules of interest. This model is perhaps one of the most important means of describing the SCF procedure [167].

We can equate Hartree-Fock theory to single determinant theory to finding a set of spin orbitals $\{\chi_a\}$ such that the single determinant formed from these spin orbitals

$$|\psi_0\rangle = |\chi_1\chi_2 \cdots \chi_a\chi_b \cdots \chi_N\rangle \tag{2.2.1}$$

is the best possible approximation to the ground state of the N-electron system described by an electronic Hamiltonian $\mathcal{H}$. According to the variational principle, the best spin orbitals are those which minimize the electronic energy

$$E_0 = \langle\psi_0|\mathcal{H}|\psi_0\rangle\Big|\psi_0\rangle = \sum_a \langle a|h|a\rangle + \frac{1}{2}\sum_{ab}[aa|bb] - [ab|ba] \tag{2.2.2}$$

It's possible systematically vary the spin orbitals $\{\chi_a\}$constraining them only to the extent that they remain orthonormal

$$E_0 = \langle\chi_a|\chi_b\rangle = \delta_{ab} \tag{2.2.3}$$

Until the energy E_0 is a minimum. In doing so one obtains an equation that defines the best spin orbitals, the ones that minimize E_0.

The equation for the best spin orbitals is the Hartree-Fock integral-differential equation

$$\begin{aligned} h(1)\chi_a(1) + \sum_{b\neq a}\left[\int d\mathbf{x_2}|\chi_b(2)|^2\, {r_{12}}^{-1}\right]\chi_a(1) \\ - \sum_{b\neq a}\left[\int d\mathbf{x_2}\, {\chi_b}^*(2)\chi_a(2){r_{12}}^{-1}\right]\chi_b(1) = \varepsilon_a\chi_a(1) \end{aligned} \tag{2.2.4}$$

Where

$$h(1) = -\frac{1}{2}{\nabla_1}^2 - \sum_A \frac{Z_A}{r_{1A}} \tag{2.2.5}$$

is the kinetic energy and potential energy for attraction to the nuclei, of a single electron chosen to be electron-one. The orbital energy of the spin orbital χ_a is ε_a.The two terms in Eq. (2.2.4) involving sum over b are those that in single determinant Hartree-Fock theory represent electron-electron interactions. Without these terms

$$h(1)\chi_a(1) = \varepsilon_a\chi_a(1) \tag{2.2.6}$$

Would simply be a one electron Schrödinger equation for the spin orbital states of a single electron in the field of the nuclei. The first of the two-electron terms in the coulomb term, which is also present in Hartree theory, a theory which uses a Hartree product (Slater determinant) wave function. The second two-electron term is the exchange term, which arises because the antisymmetric nature of the determinantal wave function.

The coulomb term has a simple interpretation. In an exact theory, the coulomb interaction is represented by the two-electron operator $r_{ij}{}^{-1}$. In the Hartree or Hartree-Fock approximation (Eq. (2.3.4)) electron-one in χ_a experiences a one electron coulomb potential

$$v_a{}^{\text{coul}}(1) = \sum_{b \neq a} \int d\mathbf{x}_2 |\chi_b(2)|^2 \, r_{12}{}^{-1} \tag{2.2.7}$$

The exchange term in Eq. (2.4.4), arising from the antisymmetric nature of the single determinant, has a somewhat strange form and does not have a simple classical interpretation like the coulomb term.

The Hartree-Fock equation (Eq. (2.2.4)) can be written as an eigenvalue equation

$$\left[h(1) + \sum_{b \neq a} \mathcal{J}_b(1) - \sum_{b \neq a} \mathcal{K}_b(1) \right] = \varepsilon_a \chi_a(1) \tag{2.2.8}$$

with

$$\mathcal{J}_b(1) = \int d\mathbf{x}_2 |\chi_b(2)|^2 \, r_{12}{}^{-1} \tag{2.2.9}$$

the *coulomb operator* and $\mathcal{K}_b(1)$ is an exchange operator defined by its effect when operating on a spin orbital $\chi_a(1)$. Unlike the local coulomb operator, the exchange operator is said to be a nonlocal operator, since there does not exist a simple potential $\chi_b(\mathbf{x_1})$ uniquely defined at a local point in space $\mathbf{x_1}$.

If the Fock operator is defined by

$$f(1) = h(1) + \sum_b \mathcal{J}_b(1) - \mathcal{K}_b(1) \tag{2.2.10}$$

the Hartree-Fock equations (this is the usual form the Hartree-Fock equations) become

$$f|\chi_a\rangle = \varepsilon_a |\chi_a\rangle \tag{2.2.11}$$

The Hartree-Fock equation Eq. (2.2.11) is an eigenvalue equation with the spin orbitals as eigen functions and the energy of the spin orbitals as eigenvalues. The exact solution to this integral-differential equation correspond to the *exact* Hartree-Fock spin orbitals. In practice it is only possible to solve this equation exactly (i.e. as an integral-

differential equation) for atoms. *The Hartree-Fock equations are really nonlinear equations and will need to be solved by iterative procedures.*

For an *N*-electron system, minimization of the energy of the determinant $|\psi_0\rangle = |\chi_1\chi_2 \ldots \chi_a\chi_b \ldots \chi_N\rangle$ leads to an eigenvalue equation $f|\chi_a\rangle = \varepsilon_a|\chi_a\rangle$ for the *N* occupied spin orbitals χ_a. The Fock operator has a functional dependence on these occupied spin orbitals, but once the occupied spin orbitals are known the Fock operator becomes a well-defined Hermitian operator, which will have an infinite number of eigenvalues.

In addition, the Hartree-Fock Hamiltonian is defined as an appropriate Hamiltonian for $|\psi_0\rangle$ is an exact eigenfunctions

$$\mathcal{H}_0 = \sum_{i=1}^{N} f(i) \tag{2.2.12}$$

where *f* (i) is a Fock operator for the i*th* electron.

The approximations of $F_{HK}[\rho]$ are expressed as a function of the exchange and correlation functional [170-172]. The form of $E_{xc}[\rho]$ continues to be up-graded although several its approximations have been published. In practical calculations, a large basis set is necessary to obtain high accuracy and convergence of the KS equations. Thus, the accuracy and the computational time of a DFT calculation is affected by the level of theory, i.e. by the choice of functional $E_{xc}[\rho]$ and the choice of an appropriate orbital basis set. In addition, other points have to be taken into account in the QM calculations.

In Eq. (2.1.23) the external potential $v(\mathbf{r})$ depends on the geometrical disposition of the nuclei, considered in fixed positions (Born-Oppenheimer approximation). A specific arrangement of the nuclei defines therefore a particular potential $v(\mathbf{r})$. Nevertheless, it is worth noting that a particular arrangement does not necessarily provide the lowest total energy of the molecular system. Thus, an optimization of the molecular geometry is necessary to find the nuclei arrangement corresponding to the lowest molecular total energy, that is, the minimum. However, in addition to a global minimum, molecular structures may have several local minima (conformational isomers). The research of all the conformational isomers may require high computational time. In this case, the combination of QM methods with other computational approaches should be used. The research of local and global minima is the necessary and the first step to obtaining the chemical and physical properties of the system. The external potential $v(\mathbf{r})$ can also be substituted by an effective potential that replaces the core electrons of the atoms constituting the system with an effective electrostatic potential (ECP); in this case only the electrons of the external orbitals are explicitly considered in the calculation [173]. This procedure decreases the computational

time and allows to take into account relativistic effects, which are important when transition metals are present in the molecule.

Finally, the Coulomb, exchange and correlation potentials, which are the last two terms in the relation Eq. (2.1.23) can be evaluated by a grid of points or expanding these potentials using another set of functions, called the 'auxiliary' basis set. Large atomic orbital basis makes the calculations very time-consuming. Thus, the calculation is faster if auxiliary basis set is used instead of a grid of points to evaluate the Coulomb, exchange and correlation potentials.

Closed-Shell Hartree-Fock: Restricted Spin Orbitals.

A restricted set of spin orbitals has the form.

$$\chi_i(\mathbf{x}) = \begin{cases} \psi_j(\mathbf{r})\alpha(\omega) \\ \psi_j(\mathbf{r})\beta(\omega) \end{cases} \tag{2.2.13}$$

And the closed-shell restricted ground state is

$$|\psi_0\rangle = |\chi_1\chi_2 \cdots \chi_{N-1}\chi_N\rangle = |\psi_1\bar{\psi}_1 \cdots \psi_a\bar{\psi}_a \cdots \psi_{N/2}\bar{\psi}_{N/2}\rangle \tag{2.2.14}$$

Now is necessary to convert the general spin orbital Hartree-Fock equation $f(1)\chi_i(1) = \epsilon_i(1)$ to spatial eigenvalue equation where each of the occupied spatial molecular orbitals $\{\psi_a | a = 1,2, \ldots, N/2\}$ is doubly occupied.

If we let $f(\mathbf{r}_1)$ be closed-shell Fock operator;

$$f(\mathbf{r}_1) = \int d\omega_1 \alpha^*(\omega_1) f(\mathbf{x}_1)\, \alpha(\omega_1) \tag{2.2.15}$$

and, if we have a closed-shell, we need sum over occupied spin orbitals includes an equal sum over those with the α spin function and those with the β spin function. The closed-shell Fock operator will has the form.

$$f(\mathbf{r}_1) = h(1) + \sum_{a}^{N/2} 2J_a(1) - K_a(1) \tag{2.2.16}$$

Where the closed –shell coulomb and exchange operator are defined by

$$J_a(1) = \int d\mathbf{r}_2\, \psi_a^*(2) {r_{12}}^{-1} \psi_a(2) \tag{2.2.17}$$

$$K_a(1)\psi_i(1) = \left[\int d\mathbf{r}_2\, \psi_a^*(2) {r_{12}}^{-1} \psi_i(2)\right]\psi_a(1)$$

These equations are quite analogous to these for spin orbitals, except for the factor of 2 occurring with the coulomb operator.

The closed-shell spatial Hartree-Fock equations is just

$$f(1)\,\psi_j(1) = \varepsilon_j \psi_j(1) \tag{2.2.18}$$

The Hartree-Fock energy is the transition from spin orbitals to spatial orbitals.

Introduction of a Basis: The Roothaan equations.

Without the spin, the calculation of molecular orbitals becomes equivalent to the problem of solving the spatial integral-differential equation

$$f(\mathbf{r}_1)\,\psi_i(\mathbf{r}_1) = \varepsilon_i \psi_i(\mathbf{r}_1) \tag{2.2.19}$$

One might attempt to solve this equation numerically; numerical solutions are common in atomic calculations. For obtain numerical solutions for molecules, the contribution of Roothaan [174] was to show how, by introducing a set of know spatial basis functions, the differential equation could be converted to a set of algebraic equations and solved by standard matrix technics. A set of *K* know basis function $\{\phi_\mu(\mathbf{r}) | \mu = 1, 2, \ldots K\}$ are introduced and thus expanded the unknown molecular orbitals in the linear expansion

$$\psi_i = \sum_{\mu=1}^{K} C_{\mu i}\, \phi_\mu\,, \qquad i = 1, 2, \ldots, K \tag{2.2.20}$$

In the set $\{\phi_\mu\}$ was complete, this would be an exact expansion, and any complete set $\{\phi_\mu\}$ could be used. For practical purposes it's assumed that $\{\phi_\mu\}$ is a set of know functions.

Form the Eq. (2.2.20), the problem of calculating the Hartree-Fock molecular orbitals reduces to the problem of calculating the set of expansion coefficients $C_{\mu i}$.

Now we define two matrices:

1. The *overlap matrix* **S** has elements

$$S_{\mu\nu} = \int d\mathbf{r}_1\, \phi_\mu^*(1)\phi_\nu(1) \tag{2.2.21}$$

and

2. The Fock matrix has elements

$$F_{\mu\nu} = \int d\mathbf{r}_1 \, \phi_\mu^*(1) f(1) \phi_\nu(1) \tag{2.2.22}$$

With these definitions of **F** and **S**, we can now write the integrated Hartree-Fock equation as

$$\sum_\nu F_{\mu\nu} \, \mathrm{C}_{\nu i} = \varepsilon_i \sum_\nu S_{\mu\nu} \, \mathrm{C}_{\nu i} \quad , \quad i = 1, 2, \ldots, K$$
$$\mathbf{F}\,\mathbf{C} = \mathbf{S}\,\mathbf{C}\varepsilon \tag{2.2.23}$$

the Roothaan equations.

The Charge Density.

If we have an electron described by the spatial wave function $\psi_a(\mathbf{r})$, then the probability of finding that electron in a volume element $d\mathbf{r}$ at a point $\mathbf{r}$ is $|\psi_a(\mathbf{r})|^2 d\mathbf{r}$. The probability distribution function (charge density) is $|\psi_a(\mathbf{r})|^2$.

If we have a closed-shell molecule described by a single determinant wave function with each occupied molecular orbital ψ_a containing two electrons, then the total charge density is just

$$\rho(\mathbf{r}) = 2 \sum_a^{N/2} |\psi_a(\mathbf{r})|^2 \tag{2.2.24}$$

such that $\rho(\mathbf{r}) d\mathbf{r}$ is the probability of finding an electron (any electron)I $d\mathbf{r}$ a $\mathbf{r}$. The integral of this charge is just the total number of electrons,

$$\int d\mathbf{r} \, \rho(\mathbf{r}) = 2 \sum_a^{N/2} \int d\mathbf{r} \, |\psi_a(\mathbf{r})|^2 = 2 \sum_a^{N/2} 1 = N \tag{2.2.25}$$

For a single determinant, these equations show that the total charge density is just a sum of charge densities for each of the electrons.

Orthogonalization of the Basis.

The bases sets that are used in molecular calculations are not orthonormal sets. The bases functions are normalized, but they are not orthogonal to each other.

If we have a set of functions $\{\phi_\mu\}$ that are not orthogonal, i.e.

$$\int d\mathbf{r}\, \phi_\mu^*(\mathbf{r}) f(1) \phi_\nu(\mathbf{r}) = S_{\mu\nu} \tag{2.2.26}$$

Then it will always be possible to find a transformation matrix $\boldsymbol{\mathcal{X}}$ (not unit) such that a transformed set of functions $\{\phi'_\mu\}$ given by.

$$\phi'_\mu = \sum_\nu \mathcal{X}_{\mu\nu} \phi_\nu \quad , \qquad \mu = 1, 2, \ldots, K \tag{2.2.27}$$

They do form an orthogonal set, i. e.,

$$\int d\mathbf{r}\, \phi'^*_\mu(\mathbf{r}) \phi'_\nu(\mathbf{r}) = \delta_{\mu\nu} \tag{2.2.28}$$

There are two ways of orthogonalizing the basis set $\{\phi_\mu\}$ in common use.
The first procedure, called *symmetric orthogonalization*, uses the inverse square root of **S** for $\boldsymbol{\mathcal{X}}$

$$\boldsymbol{\mathcal{X}} \equiv \mathbf{S}^{-1/2} = \mathbf{U}\mathbf{s}^{-1/2}\,\mathbf{U}^\dagger \tag{2.2.29}$$

A second way of obtain an orthonormal set of bases functions is called *canonical orthogonalization*. It uses the transformation matrix

$$\boldsymbol{\mathcal{X}} = \mathbf{U}\mathbf{s}^{-1/2} \tag{2.2.30}$$

The SCF Procedure.

With the background of this chapter we are now in a position to describe the actual computational procedure for obtaining restricted closed-shell Hartree-Fock wave functions for molecules, i.e. $|\psi_0\rangle$.

Some authors restrict the term Hartree-Fock solution to one that is at the Hartree-Fock limit, where the basis set is essentially complete, an use the term self-consistent-field (SCF) solution for one obtained with a finite possibly small, basis set. We use the terms Hartree-Fock and SCF interchangeably, however, and specifically refers to the Hartree-Fock limit when necessary. The SCF procedure is as follows:

1. Specify a molecule (a set of the nuclear coordinates $\{\mathbf{R}_A\}$, atomic numbers $\{Z_A\}$, and number of electrons *N*) and a basis set $\{\phi_\mu\}$.
2. Calculate all required molecular integrals $S_{\mu\nu}, H_{\mu\nu}^{\text{core}}$ and $(\mu\nu|\lambda\sigma)$.
3. Diagonalize the overlap matrix S and obtain a transformation matrix $\boldsymbol{X}$ from Eq. (2.3.30).
4. Obtain a guess at the density matrix **P**.
5. Calculated the matrix G of the $F_{\mu\nu} = H_{\mu\nu}^{\text{core}} + G_{\mu\nu}$ form the density matrix **P** and the two-electron integrals $(\mu\nu|\lambda\sigma)$.
6. Add G to the core-Hamiltonian to obtain the Fock matrix $\mathbf{F} = \mathbf{H}^{\text{core}} + \mathbf{G}$.
7. Calculate the transformed Fock matrix $\mathbf{F}' = \boldsymbol{X}^{\dagger}\mathbf{F}\boldsymbol{X}$.
8. Diagonalize F´ to obtain C´ and ε.
9. Calculate $\mathbf{C} = \boldsymbol{X}\mathbf{C}'$
10. From new density matrix **P** from **C** using $P_{\mu\nu} = 2\sum_a^{N/2} C_{\mu a}C_{\nu a}^*$
11. Determine whether the procedure has converged, i.e. determine whether the new density matrix of step (10) is the same as the previous density matrix within a specified criterion. If the procedure has not converged return to the step (5) with the new density matrix.
12. If the procedure has converged, then use the resultant solution, represented by C, P, F, etc., to calculate expectation values and other quantities of interest.

Chemical Potential and Electronegativity.

We use the density-functional theory to obtain the equations governing the change from one ground state to another. These results have a splendid relevance for the chemical properties of the molecules.

The fundamental differential expression of density-functional theory, for the change from one ground estate to another for some electronic system, is the formula

$$dE = \mu\, dN + \int \rho(\mathbf{r}) dv(\mathbf{r}) d\mathbf{r} \qquad (2.2.31)$$

Where dE is the electronic energy, the coefficient μ is the chemical potential, *N* is the electron number in the system, $\rho(\mathbf{r})$ is the electron density (the density ρ is just the three dimensional single-particle density evinced in diffraction experiments and so readily

visualized and the quantum theory for ground states can be put in terms of it) and $v(\mathbf{r})$ is the nuclear potential.

In the Eq. (2.2.31) the ground state $\rho(\mathbf{r})$ must satisfy the Euler equation $\left[\frac{\delta E}{\delta \rho(\mathbf{r})}\right]_v = \mu$; while from the first-order perturbation to energy change we have $\left[\frac{\delta E}{\delta v(\mathbf{r})}\right]_\rho = \left[\frac{\delta E}{\delta v(\mathbf{r})}\right]_N = \rho(\mathbf{r})$. Now if $dN = \int d\rho(\mathbf{r}) d\mathbf{r}$ we obtain

$$\mu = \left(\frac{\partial E}{\partial N}\right)_v \tag{2.2.32}$$

Similarly the change in chemical potential associated with a change in N and/or v is $d\mu = \left(\frac{\partial \mu}{\partial N}\right)_v dN + \int \left[\frac{\delta \mu}{\delta v(\mathbf{r})}\right]_N d\boldsymbol{v}(\mathbf{r}) d\mathbf{r}$, introducing the symbols

$$2\eta = \left(\frac{\partial \mu}{\partial N}\right)_v \tag{2.2.33}$$

and

$$f(\mathbf{r}) = \left[\frac{\delta \mu}{\delta v(\mathbf{r})}\right]_N = \left(\frac{\partial \rho(\mathbf{r})}{\partial N}\right)_v \tag{2.2.34}$$

we arrive at the formula

$$d\mu = 2\eta dN + \int f(\mathbf{r}) dv(\mathbf{r}) d\mathbf{r} \tag{2.2.35}$$

The second part for $f(\mathbf{r})$ in the Eq. (2.2.34) is a "Maxwell Relation" following from the fact that dE is a exact differential.

The density-functional Eq. (2.2.35) is highly pertinent for chemical concepts. As already stated, μ is the negative of the *electronegativity* χ of the species $\mu = \left(\frac{\partial E}{\partial N}\right)_v = -\chi$, η is the *hardness* of the species. Both μ and η are numbers, *global* properties of the species [168]. The quantity $f(\mathbf{r})$ is a local property that depends on $\mathbf{r}$ (the *Fukui function* for the species [175]).

Considering the physical meaning of the chemical potential χ as a global property of a ground state, constant from point to point in the atom or molecule, in principle calculable

for each N and v in terms of the fundamental constants of physics as $\mu = [N, v]$. For a change from one ground state to another, $d\mu$ is given by Eq. (2.2.35). Then when atoms (or other combining groups) of different chemical potential unite to form a molecule with its own characteristic chemical potential, to the extent that the atoms (groups) retain their identity, their chemical potentials must equalize [176-177]. Thus

$$\mu = \left(\frac{\partial E}{\partial N}\right)_v = -\chi \tag{2.2.36}$$

The following basic properties of χ are: 1) The electronegativity (chemical potential) is a property of the state of the system, calculable in terms of the constants of physics from density functional theory. 2) Electronegativity differences (chemical potential differences) drive electron transfer. 3) On formation of a molecule, electronegativities (chemical potentials) of constituent atoms or groups equalize (neutralize), all becoming equal to the electronegativity of the final molecule.

Finally, the chemical potential is the negative of the electronegativity the Pauling and Mulliken [178]. For, the three point finite-difference approximation to $\partial E/\partial N$ for a species S is:

$$\mu \approx -\frac{I + A}{2} \tag{2.2.37}$$

where $I = E_s^+ - E_s$ (the Highest Occupied Molecular Orbital, HOMO) and $A = E_s - E_s^-$ (the Lowest Unoccupied Molecular Orbital, LUMO) are respectively the ionization potential and electron affinity for the species. And Mulliken formula for electronegativity is [179]:

$$\chi = \frac{I + A}{2} \tag{2.2.38}$$

Therefore $\mu \approx -\chi$ (similarly to Eq. (2.2.36) and the chemical potential concept is the same as the electronegativity concept.

Harness and Softness.

Now turn to the derivatives of the chemical potential $\mu = [N, v]$. The first is what may be called absolute hardness of a species [180]

$$\eta = \frac{1}{2}\left(\frac{\partial \mu}{\partial N}\right)_v = \frac{1}{2}\left(\frac{\partial^2 E}{\partial N^2}\right)_v \tag{2.2.39}$$

The inverse of hardness is softness [181]

$$S = \frac{1}{2\eta} = \left(\frac{\partial N}{\partial \mu}\right)_v \tag{2.2.40}$$

The first property we have, from the convexity assumption is $\eta \geq 0$. The second property, the finite-difference approximation for hardness is the formula,

$$\eta = \approx \frac{I - A}{2} \tag{2.2.41}$$

For an insulator or semiconductor, hardness is half of the bandgap. In the context of molecular orbital theory, using Koopman's approximation, Eq. (2.2.40) can be further simplified using the negative of the eigenvalues (ϵ) of the highest occupied (ϵ_{HOMO}) and lowest unoccupied (ϵ_{LUMO})) orbitals instead of I and A. Therefore, the previous definitions, hardness and softness, become [182]

$$\begin{aligned} \eta = \approx \frac{\epsilon_{\mathrm{LUMO}} + \epsilon_{\mathrm{HOMO}}}{2} \\ \mu \approx \frac{\epsilon_{\mathrm{LUMO}} - \epsilon_{\mathrm{HOMO}}}{2} \end{aligned} \tag{2.2.42}$$

Multiplicity.

In spectroscopy and quantum chemistry, the multiplicity of an energy level is defined as $2S+1$, where S is the total spin angular momentum[183-184]. States with multiplicity 1, 2, 3, 4, 5 are respectively called singlets, doublets, triplets, quartets and quintets.

The multiplicity is often equal to the number of possible orientations of the total spin relative to the total orbital angular momentum L, and therefore to the number of near–degenerate levels that differ only in their spin–orbit interaction energy.

Chapter 3

Experimental Methods

3.1 Transmission Electron Microscopy (TEM)

A transmission electron microscope (TEM) is an analytical tool allowing visualization and analysis of specimens in the realms of microspace (1 micron/1μm = 10^{-6}m) to nanospace (1 nanometer/nm = 10^{-9}m). The TEM reveals levels of detail and complexity inaccessible by light microscopy because it uses a focused beam of high-energy electrons. It allows detailed micro-structural examination through high-resolution and high magnification imaging. It also enables the investigation of crystal structures, specimen orientations and chemical compositions of phases, precipitates and contaminants through diffraction pattern, X-ray and electron energy analysis.

Transmission electron microscopy is used to produce images from a sample by illuminating the sample with electrons (i.e. the electron beam) within a high vacuum, and detecting the electrons that are transmitted through the sample.

TEM is a microscopy technique whereby a beam of electrons is transmitted through an ultra-thin specimen, interacting with the specimen as it passes through. An image is formed from the interaction of the electrons transmitted through the specimen; the image is magnified and focused onto an imaging device, such as a fluorescent screen, on a layer of photographic film, or to be detected by a sensor such as a CCD camera.

Max Kroll and Ernst Ruska built the first TEM in 1931, with this group developing the first TEM with resolution power greater than that of light in 1933 and the first commercial TEM in 1939. TEM can be used to study the growth of layers, their composition and defects in semiconductors. High-resolution can be used to analyze the quality, shape, size and density of quantum wells, wires and dots.

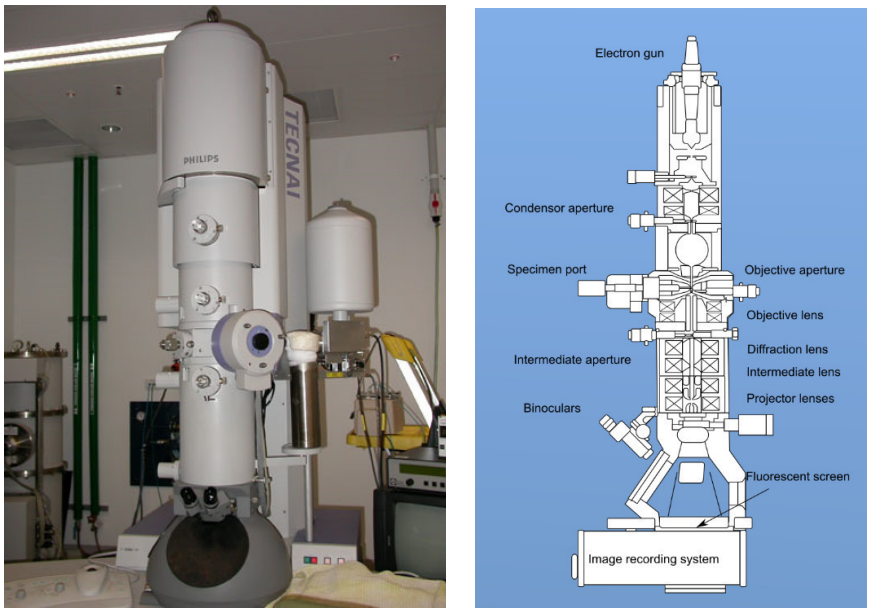

Figure 3.1. The Transmission Electron Microscope (TEM) in laboratory [185]

The word “transmission” means “to pass through”. Essentially, the way the transmission electron microscope creates a conventional image (usually termed a bright-field image) of a sample can be compared to shadow puppetry. Imagine a torch beam shone through a lattice on a window. The light passes through the transparent parts of the window, but is stopped by the lattice bars. On a wall beyond, we see the lattice bars as shadows. The TEM uses a beam of highly energetic electrons instead of light from a torch. On the way through the sample some parts of the material stop or deflect electrons more than other parts. The electrons are collected from below the sample onto a phosphorescent screen or through a camera. In the regions where electrons do not pass through the sample the image is dark. Where electrons are unscattered, the image is brighter, and there is a range of grays in between depending on the way the electrons interact with and are scattered by the sample.

TEM examine the structure, composition, and properties of specimens in submicron detail. Aside from using it to study general biological and medical materials, transmission electron microscopy has a significant impact in fields such as: materials science, geology, environmental science, among others. The investigation of the morphology, structure, and local chemistry of metals, ceramics, and minerals is an important aspect of contemporary materials science. It also enables the investigation of crystal structures, orientations and chemical compositions of phases, precipitates and contaminants through diffraction pattern, characteristic X-ray, and Electron Energy Loss Analysis.

TEM **can**:

- Image morphology of samples, e.g. view sections of material, fine powders suspended on a thin film, small whole organisms such as viruses or bacteria, and frozen solutions.
- Tilt a sample and collect a series of images to construct a 3-dimensional image.
- Analyze the composition and some bonding differences (through contrast and by using spectroscopy techniques: microanalysis and electron energy loss).
- Physically manipulate samples while viewing them, such as indent or compress them to measure mechanical properties (only when holders specialized for these techniques are available).
- View frozen material (in a TEM with a cryostage).
- Generate characteristic X-rays from samples for microanalysis.
- Acquire electron diffraction patterns (using the physics of Bragg Diffraction).
- Perform Electron Energy Loss Spectroscopy of the beam passing through a sample to determine the sample composition or the bonding states of atoms in the sample.

TEM **can't do:**

- TEM cannot take color images. Color is sometimes added artificially to TEM images.
- TEM cannot image through thick samples: the usual sample thickness is around 100-200nm. Electrons cannot readily penetrate sections much thicker than 200nm.
- A standard TEM cannot image surface information.
- The TEM cannot reliably image charged molecules that are mobile in a matrix. For example, some species (e.g. Na+) are volatile under the electron beam because the negative electron beam exerts a force on charged material.

Electron images from the TEM can be used to achieve different information, for example for morphological, crystallographic or compositional studies. It is also possible to label molecules with electron dense particles (e.g. nano-sized gold spheres that attach to molecules through immunolabeling techniques) or construct 3-dimensional images of particle, structures or cells through tomography.

The fundamental basis of electron microscopy is the use of an electron beam. It is for this reason that the TEM requires a vacuum. If air were present, the molecules would cause the beam to scatter. It is also imperative to understand the interactions between the electron beam and the sample so as to interpret the resulting images. The use of electrons has an impact on image resolution and absence of color, and explains the two-dimensional nature of micrographs (images/photographs) [185].

Fundamental Theory of TEM

The Concept of Resolution

The smallest distance between two points that we can resolve by our eyes is about 0.1-0.2 mm, depending on how good our eyes are. This distance is the resolution or resolving power of our eyes. The instrument that can show us pictures revealing detail finer than 0.1 mm could be described as a microscope.

The Rayleigh criterion defines the resolution of light microscope as:

$$\delta = \frac{0.61\,\lambda}{\mu\, sin\beta}, \tag{3.1.1}$$

Where λ is the wavelength of the radiation, μ is the refractive index of the view medium and β is the semi-angle of collection of the magnifying lens. The variable of refractive index and semi-angle is small; thus the resolution of light microscope is mainly decided by the wavelength of the radiation source. Taking green light as an example, its 550 nm wavelength gives 300 nm resolution, which is not high enough to separate two nearby atoms in solid-state materials. In fact, the distance between two atoms in solid is around 0.2nm.

Based on wave-particle duality, we know that electron has some wave-like properties:

$$\lambda = \frac{h}{p} \tag{3.1.2}$$

If an electron is accelerated by an electrostatic potential drop eU, the electron wavelength can be described as:

$$\lambda = \frac{h}{\sqrt{2m_{\circ}eU\left(1 + \frac{eU}{2m_{\circ}c^2}\right)}} \tag{3.1.3}$$

If we take the potential as 100keV, the wavelength is 0.0037nm. The resolution of electron microscope should be better than that of light microscope.

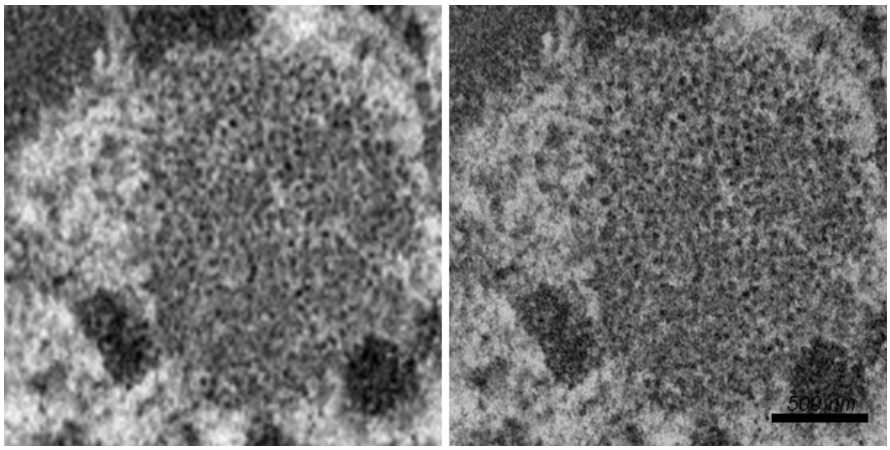

Figure 3.2. Low resolution and high-resolution of a cell nucleus (rat's liver cell). The left image is an enlargement of a low magnification image whereas the right image is taken at the higher magnification [185].

The Instrument of Transmission Electron Microscope

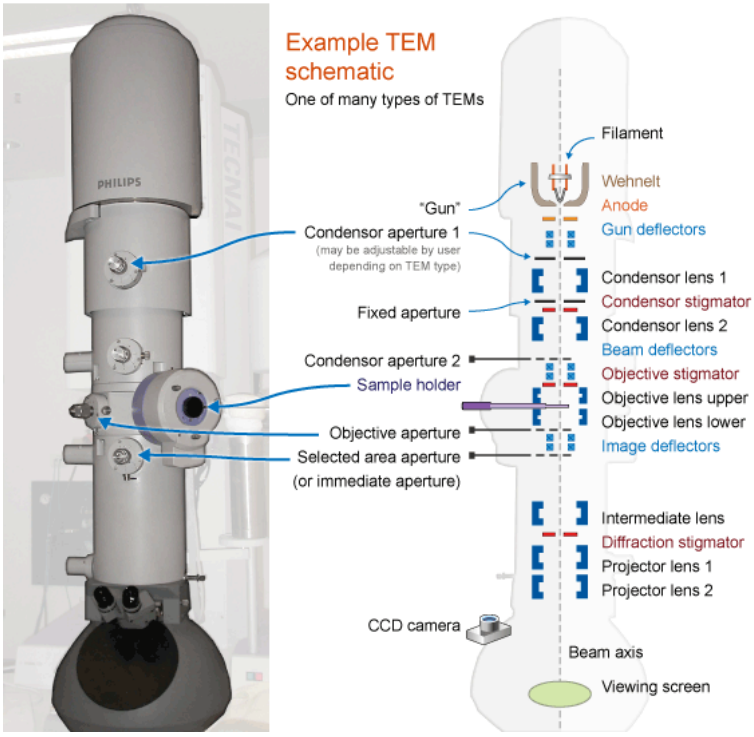

Figure 3.3. A generalized cut-away diagram of the internal structure of a transmission electron microscope alongside an example of a modern instrument [185]

- Illumination system. It takes the electrons from the gun and transfers them to the specimen giving either a broad beam or a focused beam. In the ray-diagram, the parts above the specimen belong to illumination system.
- The objective lens and stage. This combination is the heart of TEM.
- The TEM imaging system. Physically, it includes the intermediate lens and projector lens.

The diffraction pattern and an image are formed at the back focus plane and an image plane of the objective lens. If we take the back focus plane as the objective plane of the intermediate lens and projector lens, we will obtain the diffraction pattern on the screen. It is said that the TEM works in diffraction mode. If we take the image plane of the objective lens as the objective plane of the intermediate lens and projector lens, we will form an image on the screen. It is the image mode.

The Interaction between Electrons and Specimen

Because the average distance between two successive incident electrons is around 0.15mm (taking 100keV as the accelerate potential), which is far greater than the TEM specimen thickness (~100-500 nm), we can consider the interaction between electrons and specimen as a single electron scattering event. From the wave-particle duality point of view, the incident electron can be expressed as a plane wave $\Psi(r) = e^{2\pi i k_0 r}$. Resolving the Schrödinger equation, we can get the departure electron wave function as:

$$\Psi(r) = \Psi_0(r) + \frac{me}{2\pi\hbar^2}\int dr' \frac{e^{2\pi ik|r-r'|}}{|r-r'|} V(r')\,\Psi(r') \tag{3.1.4}$$

Taking Mutt approximation:

$$\Psi(r) = e^{2\pi i k_0 r} + \frac{me}{2\pi\hbar^2}\frac{e^{2\pi ikr}}{r}\int dr' e^{-2\pi i(k-k_0)} V(r') \tag{3.1.5}$$

The amplitude of the scattering beam is the Fourier transform of the specimen's potential.

If we considering perfect crystal, its potential can be described as:

$$V(r) = \sum_n \sum_r V_\alpha(r - R_n - r_\alpha) S_p(r) \tag{3.1.6}$$

$S_p(r)$ is the shape factor of crystal.

The Fourier transform of the potential is:

$$\Phi(u) = \sum_{g} \delta(u-g)V_g \tag{3.1.7}$$

Where V_g is the structural factor and

$$V_g = \sum_{\alpha} e^{-2\pi i g r} f_\alpha(g) \tag{3.1.8}$$

The diffraction intensity can be calculated as:

$$|\Phi(u)|^2 = \left| \{ \sum_{g} \delta(u-g)V_g \} \otimes S_p(u) \right|^2 \tag{3.1.9}$$

Diffraction Contrast

There are two basic modes of TEM operation, namely the bright-field mode, where the (000) transmitted beam contributes to the image, and the dark-field imaging mode, in which the (000) beam is excluded. The size of the objective aperture in bright-field mode directly determines the information to be emphasized in the final image. When the size is chosen so as to exclude the diffracted beams, one has the configuration normally used for low resolution defect studies, so-called *diffraction contrast*. In this case, a crystalline specimen is oriented to excite a particular diffracted beam, or a systematic row of reflections, and the image is sensitive to the differences in specimen thickness, distortion of crystal lattices due to defects, strain and bending.

Phase Contrast

Diffraction contrast is a dominant mechanism for imaging dislocations and defects in the specimen. However, the resolution of this imaging technique is limited to 1-3 nm. Diffraction contrast mainly reflects the long-range strain field in the specimen and it is unable, however, to provide high-resolution information about the atom distribution in the specimen.

The diffraction of electrons is purely a result of the wave property of particles. The *wavelength* of an electron is a typical quantity for characterizing an incident plane wave.

The calculation of electron wavelength has been performed previously, however, without consideration the perturbation of the crystal potential on the electron kinetic energy. If the electron is traveling in a crystal, which is characterized by an electrostatic potential field V(x, y, z), the equation should be modified as

$$eU_0 = K.E. + P.E = \left(\sqrt{m_\circ^2 c^4 + p^2 c^2} - m_\circ c^4\right) + (-eV) \tag{3.1.10}$$

Therefore, the structure perturbed electron wavelength can be obtained. The effective *wave number* is

$$\begin{aligned} K_{eff} = \frac{1}{\lambda_{eff}} = \frac{p}{h} = \frac{1}{h}\left[2m_\circ e(U_0 + V)\left(1 + \frac{e(U_0 + V)}{2m_\circ c^2}\right)\right]^{1/2} \\ = \frac{1}{\lambda}[(1 + \frac{V}{U_0})(1 + \frac{eV}{2m_\circ c^2 + eU_0})]^{1/2} \\ \approx \frac{1}{\lambda}[1 + \frac{V(r)}{U_0}]^{1/2} \\ \approx \frac{1}{\lambda}[1 + \frac{V(r)}{2U_0}] \end{aligned} \tag{3.1.11}$$

Where an approximation of $V << U_0$ is made. We now consider a case in which the specimen covers only half space and leave the other half as vacuum. Thus the relative phase shift of the wave traveling in the crystal field relative to the wave traveling in the absence of a field for a specimen thickness d is

$$\begin{aligned} \int_0^d dz\, 2\pi\left(\frac{1}{\lambda_{eff}} - \frac{1}{\lambda}\right) \approx \sigma V_p(b) \\ \sigma = \frac{\pi}{\lambda U_0} \end{aligned} \tag{3.1.12}$$

The *projected potential* of the crystal is

$$V_p(b) = \int_0^d dz\, V(r) \tag{3.1.13}$$

Therefore, the effect of the potential field is represented by multiplying the wave function by a phase grating function

$$Q(b) = \exp[i\sigma V_p(b)] \tag{3.1.14}$$

This is known as the *phase object approximation* (POA), in which the crystal acts as a phase grating filter. From this expression, it can be seen that the effect of the crystal potential is to modify the phase of the incident electron wave. The variability of the projected crystal potential results in the change of electron phase. The contrast produced by this mechanism is called *phase contrast* [185-186].

3.2 Thermogravimetric Analysis (TGA)

Thermal methods of investigation, generally referred to as thermo- or thermal analysis or thenno-analytical techniques, have found wide application in recent years1 These may be defined as experimental methods for characterising a system (element, compound or mixture) by measuring changes in physico-chemical properties at elevated temperatures as a function of increasing temperature. The two chief methods are (a) differential thermal analysis, in which changes in "heat content" are measured as a function of increasing temperature and (b) thermogravimetric analysis, in which changes in weight are measured as a function of increasing temperature. Other methods that come within this definition involve the use of changes in gas volume or pressure; changes in solid volume; changes in electrical resistance ; changes in ultraviolet, visible or infrared transmission or reflectance[187].

Thermogravimetry is a method of thermal analysis in which the mass of a sample, is measured over time as the temperature changes in a controlled atmosphere. The TGA is therefore a classical technique that allows a quantitative thermal analysis of a sample, without however identifying the nature of the components and only by measuring how much weight is lost from the sample to a certain temperature. From this analysis we obtain spectra (mass as a function of temperature) called thermogravimetric curves.
The instrumentation used for the TGA consists of four components:

- Thermal balance;
- Oven
- A purge gas system that ensures an inert or reactive atmosphere as appropriate;
- Processor for instrument control, data acquisition and visualization;

The scales available for this type of analysis have an operating range between 5–20 *mg*. In the thermal balance the sample is placed in the oven, equipped with an accurate temperature

regulation, which generally operates in the range 20 - 1500 ˚*C*. The system as a whole is managed by a computer that simultaneously weighs and heats the sample in the manner desired by the operator, recording the values of mass and temperature over time. The sample is placed inside a containment system that also allows the control of the press and of the surrounding atmosphere.

The weighing mechanism.

There are different mechanisms for measuring mass variation as a function of temperature. Fixed point systems are usually favored as they ensure the constant position over time of the sample subjected to mass variations. Different types of sensors are used to measure the displacement of the scale arm. For example, as shown in (Figure 3.4) in photoelectric systems, an opaque obstacle is used, which is integral with the arm and interposed in the optical path between LED and photocell. The obstacle attenuates the light beam to the photocell, which emits a signal used to bring the system back to its fixed point, at the same time providing a measure of the mass variation.

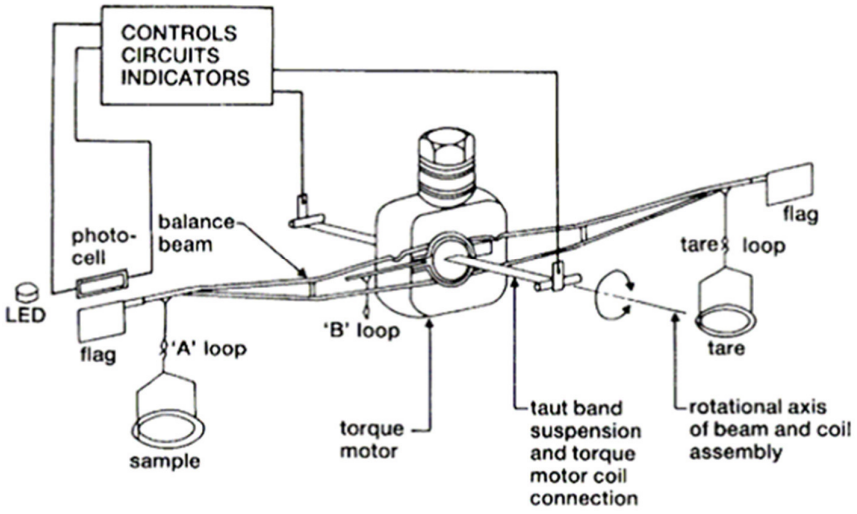

Figure 3.4. The mechanism of the thermogravimetric balance [188].

The mechanism is usually electromagnetic. The sensitivity of the scale and the maximum load that can bear without damage are linked to each other; typical values see maximum loads of grams with microgram sensitivity. There are systems based on quartz crystals that reach sensitivity of the order of nanograms. The control software provides for the

tare operation and the calculation of the scaling factor in order to provide the mass loss in terms of percentage of the initial mass.

Sample heating: in more conventional systems, there are three main methods of positioning the sample inside the oven (Figure 3.5):

- The sample is placed on a support that hangs from the scale arm inside the oven;

- The sample can be placed on a rigid support placed above the scale arm and placed in the oven.

- A third configuration is provided as a support for the sample a horizontal arm which extends the balancing mechanism. In this case also the oven is positioned horizontally

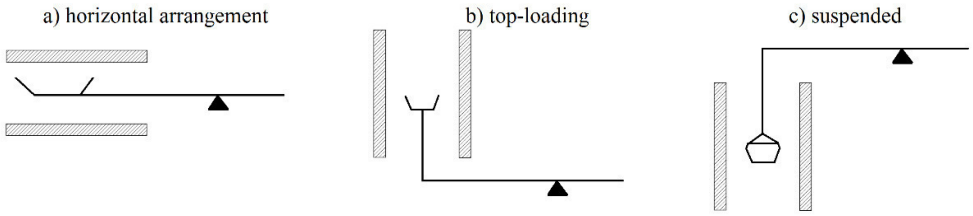

Figure 3.5. Different configurations to heat the sample.

The oven is generally equipped with an electric heating system installed inside or outside the containment system. Systems that use heating with electrical resistors heat the sample mainly by conduction through solids or gases with temperature gradients that are inevitably high, especially when working with samples with low thermal conductivity. The choice of resistance materials is influenced by the maximum temperature and the type of working atmosphere. Beyond the characteristic limit of resistances in Rhodium (1800 ° *C*) Molybdenum (2200 ° *C*) and Tungsten (2800 ° *C*) are used but only in non-oxidizing atmospheres. Alternative systems consider heating with infrared or microwave. In the first case we use the concentration of the radiation coming from different halogen lamps made through parabolic reflectors. Heat transmission is virtually instantaneous assumed that the path between source and sample is transparent to radiation. Temperatures above 1400 ° C can be reached with a heating rate of 1000 ° C / min with an error on the temperature control of about 0.5 ° C. If gases that absorb the infrared are released while heating the sample, the heat flow to the sample changes; especially in the case where there is condensation on the containment surface

of the scale involved in the optical path of the radiation. Several proposals have been made to use a microwave-based system to generate uniform temperature fields. There would be the significant advantage of being able to use larger samples, but there are significant complications in terms of power and temperature control due to the difficult placement of the thermocouples.

Working atmosphere: normally the measuring mechanism is inserted inside a glass or metal containment system in such a way as to allow operation with different types of atmosphere (inert, oxidizing, reducing or corrosive) to values of pressure ranging from the vacuum field up to 70 atm.

Temperature measurement and control: The sample temperature is usually lagging behind the oven temperature, and cannot be measured very easily without interfering with the weighing process. The delay can be up to 20-30 ° C depending on the operating conditions. The delay is greater the more you work in a vacuum, in rapid fluxing or with a high rate of heating. The measurement of the temperature is usually carried out with the help of separate thermocouples for measuring the temperature of the furnace and for that of the sample. Factors such as stability, sensitivity (V / ° *C*) and cost determine the choice of thermocouples. Stability can be improved, to the detriment of an increase in response time, by placing the thermocouple in a sheath of inert material. Response time and thermocouple duration are strongly influenced by the wire diameter. It goes on higher diameters to improve mechanical strength and durability, but also decrease sensitivity and increase response time. The long-term stability of a thermocouple also depends on maintaining its composition over time. At very high temperatures, in fact, diffusion and / or vaporization phenomena can lead to mutual contamination of the two metals constituting the joint, decreasing the sensitivity.

The sample: Even in the case of solid samples that nominally have the same chemical composition, there may be considerable differences in the behavior in the heating phase due to some structural differences, such as the presence of voids, porosity and surface properties, which they depend on how the sample is prepared and treated after preparation. For example, the behavior of a sample made up of single crystals will generally be very different from that of finely ground materials. Moreover, the influence of the defects on the reactivity generally increases with the dimensions, so the thermal properties of the powders differ significantly from those of materials with a larger size. In general, the sample must be in powder form so

that the heat can diffuse in the most uniform way possible and must be placed inside a very thin container.

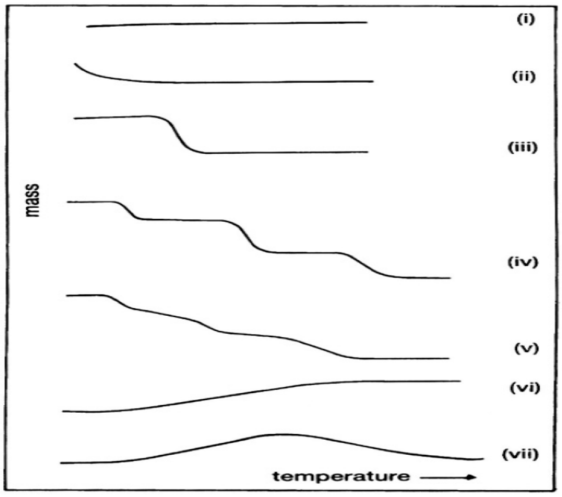

Figure 3.6. Thermogravimetric curves [188].

The interpretation of the obtained curves can be classified into different types, for example the possible interpretations, of the curves, shown in (Figure 3.6), are the following:

(I) The sample does not undergo any decomposition with loss of volatile products in the indicated temperature range;

(II) The rapid initial mass loss observed is characteristic of a desorption or drying phenomenon;

(III) This curve represents the decomposition of the sample in a single phase. The curve can be used to define the stability limits of the reagent, to determine the stoichiometry of the reaction, and to investigate the reaction kinetics;

(IV) This curve indicates multiple decomposition steps. Also in this case, the temperature of the stability limit of the reagent and of the intermediate phases can be determined by the curve;

(V) Also represents multiple decomposition phases, but in this example a stable intermediate phase did not develop;

(VI) This curve shows an increase in mass, due to the reaction of the sample with the surrounding environment. A typical example, could be the oxidation of a metal sample;

(VII) This curve shows the presence of a maximum such as in the case of an oxidation reaction where the product decomposes again at high temperatures.

Chapter 4

Synthesis of Carbon Nano-onions

4.1 Introduction

Although various methods have been published for the synthesis of CNOs, the main synthetic methods have been thermal annealing of ultradispersed nanodiamonds (NDs) [189], arc-discharge between two electrodes submerged in water [190-192], pyrolysis [193], ion implantation [194], chemical vapour deposition [195], or electron-beam irradiation [196]. Depending on the preparation method of the onion-like structures, different types of nanostructures can be achieved with varying sizes (‘‘big” [192]- [197] and ‘‘small” [189]-[198]), shapes (spherical [198-199]-[197]-[200] and polyhedral [198-199]), and types of cores (dense [192]-[197-198] and hollow [199-200]-[182]) (Figure 1.16). Figure 1.16 presents images obtained with high-resolution transmission electron microscopy (HRTEM) representing the different types of onion-like carbon nanostructures. The dimensions of the nanostructures fluctuate within the range of 2 and 200 nm.

Small amounts of spherical and polyhedral CNOs with diameters ranging from 8 to 15 nm were created in vacuum (106 Torr) [184]. Amorphous carbon layers were deposited on the surface of carbon rods and nanoparticles consisting of concentric multi-shells inside an amorphous carbon film. Iijima observed that the distance between the layers is approximately 3.44 Å, and the angles between graphitic planes is approximately 120 ± 20 [184]. About a decade later in 1992, Daniel Ugarte examined the formation of CNOs at 300-kV HRTEM by irradiating a carbon soot material and observing the formation of quasi-spherical onion-like particles with diameters ranging from 6 to 47 nm that were composed of concentric graphitic shells (70 shells) [136]. Large-scale production (gram quantities) of CNOs was realized through a method proposed by Kuznetsov et al. [189]. The method is based on annealing of nanodiamond (ND) particles (average diameter of 5 nm) at high temperatures in an inert atmosphere under high vacuum (Figure. 1.16a). The diameter of the formed CNOs is analogous to the diameter of the used NDs (Figure 1.16b). The transformation of NDs to CNOs is a multistep process and is schematically presented in Figure 1.17 [73]. The distance between the diamond planes in bulk diamond is 0.205 nm [201]. The interlayer distance is close to 0.35 nm,

i.e. typical for bulk graphite (d002=0.334 nm) [189]. Thermal annealing of NDs up to 1900 C leads to the formation of polyhedral nanostructures (Figure 1.16c) [198]. Currently, the method for the production of CNOs from the annealing of NDs is one of the most economical methods of synthesis for spherical CNOs and has potential for industrial applications, as the onion yield is close to 100% (the amount of non-carbon material is typically in the range of 1–2 wt) [73].

Synthesis of CNOs with few layers is highly desired to increase the ability to modify them using chemical reactions, since this type of CNO has greater surface curvature and strain energy, which leads to higher chemical reactivity [202]. Another method for the preparation of CNOs was proposed by N. Sano, which is based on an arc-discharge (voltage was 16 V and current was 30 A) between two graphite electrodes submerged in water [192]. This method resulted in the creation of hollow-core, bigger onion-like nanostructures with 20–30 graphene layers with particle diameters between 15 and 25 nm (Figure 1.16d) [203].

The method is ion implantation of carbon ions into copper [204] or silver substrates [205]. Depending on the implantation parameters (temperature, substrate concentration, implanted dose, and grain size of substrate), the created CNOs can have different size distributions, homogeneities and microstructures (defects, spherical shape, etc.). Higher temperatures lead to the formation of a more ideal structure of the carbon nanoparticles [206]. The carbon nanostructures obtained from a low implanted dose have more defective structures with small sizes (2–5 nm) [207]. Chemical vapour deposition was also considered as a viable method of the production of CNOs [195]- [208]. This process was performed in the presence of a metal catalyst, high temperature and high pressure. From this method, pristine (undoped) spherical nanoparticles with diameters between 5 and 50 nm were obtained in large quantities.

There are many other methods for the production of CNOs, including catalyst-free thermolysis using sodium azide (NaN3) and hexachlorobenzene (C6Cl6) [209], laser ablation [210], solid-state carbonization of phenolic resin [211], halogen gas treatment [212], high-energy ball milling [213] and heavy shock compression [214].

The size, number of layers, physical and chemical properties of CNOs depend on the synthetic conditions of their preparation. Due to the advantages of ND-derived CNOs, i.e. small size, spherical and polyhedral shapes, high reactivity, and high yield during synthesis, a great interest in these materials was created among scientists in the last 10 years. Annealing NDs at temperatures between 800–2100 C in vacuum results in the formation of CNOs with the different graphene-like structures (spherical, polyhedral or ellipsoidal nanoparticles) that were demonstrated by experimental [215-216] and theoretical [217] evidence. The Figure 4.1 sows these CNOs in spherical and polyhedral forms.

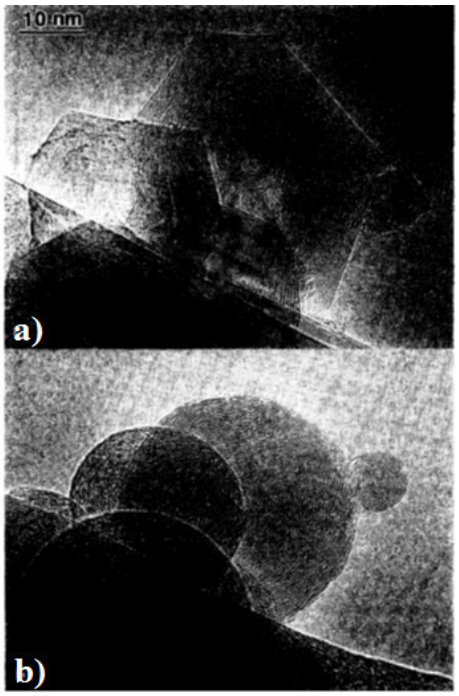

Figure 4.1: High-resolution electron micrographs of graphitic particles: a) polyhedral and b) quasi spherical (Bucky-Onions) [81]

4.2 Arc discharge synthesis of carbon nano-onions

Arc Discharge.

The Arc Discharge process is based on the application of a potential difference of 12-25V with a current between 50-120A between two graphite electrodes spaced 1mm from each other [218]

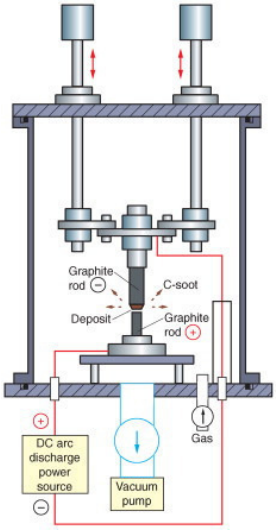

Figure 4.2: Schematic Diagram of arc discharge method [219]

The temperatures reached above 4000 K, in the atmosphere of helium, cause the evaporation of the anode, subsequent deposition on the surface of the cathode, which, after a rapid cooling, crystallizes in the form of CNO, CNT and carbon fibers depending on the synthesis conditions [219].

Underwater Arc Discharge.

Generally, the production of carbon nanomaterials requires a very expensive vacuum system and a valve system to insert the inert gas into the reaction chamber. In 2001 Sano [191] proposes a method for producing CNOs in large quantities without using vacuum systems and equipment. These nanoparticles are produced by an arc discharge between two graphite electrodes pure to 99.99% in deionized water.

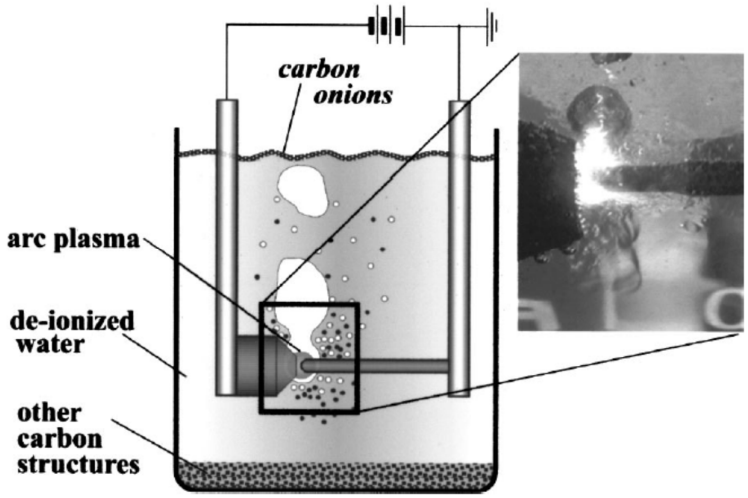

Figure 4.3: Experimental apparatus of the underwater arc discharge [191]

At the end of the process, the authors report that the surface-picked material contained CNOs and CNTs.

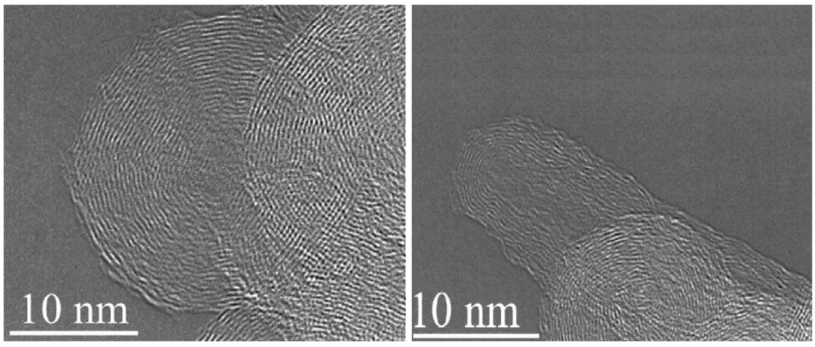

Figure 4.4: HRTEM images depicting CNOs and CNTs [191]

In 2002, Sano and his collaborators submitted a second work on the synthesis of CNOs through underwater arc discharge. In this article, they propose a model, to explain the synthesis mechanism of the two observed nano structures. Figure 4.5 describes this model in detail. It can be seen that the plasma environment formed around the electrodes is surrounded by a bubble of gas due to the vaporization of the surrounding water, as the arc temperature is about 4000 ˚K, the melting point of the graphite is T_f = 3823 ˚K. The gas bubble can be considered as a cooling chamber that allows a rapid shutdown of the arc discharge.

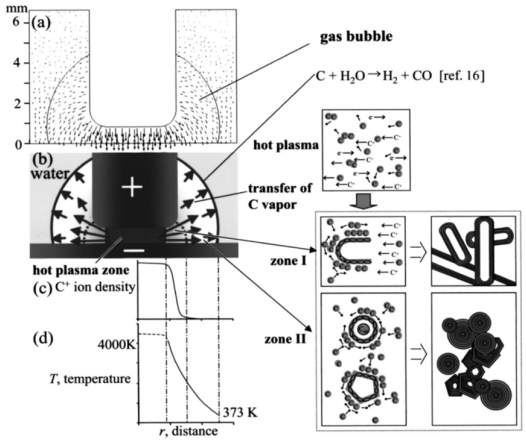

Figure 4.5: CNOs formation mechanism through underwater arc discharge; (a) direction of the electric field between anode and cathode in the gas bubble in water, (b) plasma expansion direction at the interface with water, (c) ion density distribution, and (d) temperature gradient its CNTs and CNOs [191]

They found found CNOs with an average diameter of 25-30 nm floating on the water surface after a 16-17 V, 30 A DC discharge between 5/12 mm diameter anode/cathode graphite electrodes. In 2002, the same group proposed a formation mechanism of CNOs and carbon nanotubes (CNTs) in a water arc [191].

In such model, the solidification of carbon vapor in the bubble surrounding the plasma zone is attributed to the temperature gradient present in the bubble from the plasma region to the gas-water interface. The synthesis of CNOs was as supposed to form in the peripheral zone of the bubble, far from the hot plasma zone. According to this model, this is precisely this temperature gradient that causes the vaporized carbonization to solidify, resulting in the formation of carbon nanotubes. An estimate of the temperature gradient can be made, assuming that the transfer of heat takes place radially from the center of the plasma.

In a successive investigation, the same group obtained CNOs by grinding the solid deposits found mostly at the bottom of the reactor [220]. In 2004, the Sano group compared the nanomaterials obtained by arc discharge between graphite electrodes in water and in liquid nitrogen [221]. Rettenbacher et al. [222] found no differences in the percentage of CNOs between samples floating or recovered on the bottom of the reactor. It appears clearly that some aspects of the technique have to be clarified, also considering that that the model proposed by Sano et al. [220] is still the only cited mechanism for the formation of CNOs in underwater arc discharge experiments [223-224].

In arc discharge experiments aimed at the production of CNOs, the samples were obtained as a mixing of dispersed nanomaterials, and fragments coming very likely from cathodic deposits. This fact has generated confusion in the interpretation of the results, and has not permitted to reveal possible differences between CNOs dispersed or contained in the deposits. It has to be noted that the model proposed by Sano et al. [191] only explains the formation of nanomaterials suspended in water, but cannot apply to the formation of nanomaterials contained in the deposit. With the purpose to clarify the above points, and with the aim of improving the efficiency of the production of CNOs, we have performed arc discharge experiments in water, paying particular attention to the cathodic deposits and to the differences between the CNOs present in the deposits and those dispersed in water. We improved the stability of the discharge by a particular experimental arrangement, in which the anode has been not only translated to approach the cathode, but also rotated to minimize the effects of local discontinuities in the arc.

In 2003 Lange and Walton [225] reported that they produced carbon nanoparticles using the arc discharge technique in water. Unlike the other work mentioned above, where the cathode has a larger diameter of the anode, in this, the two electrodes are equal (6 mm).

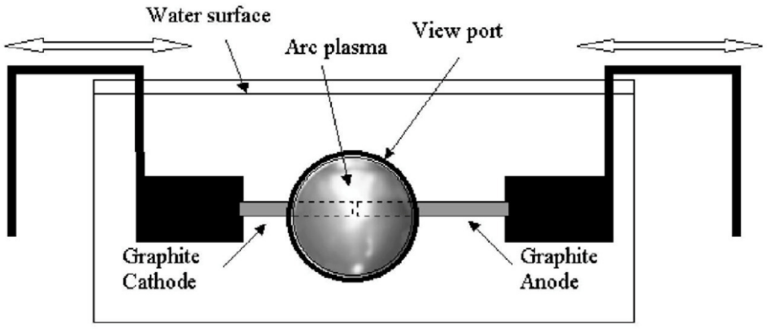

Figure 4.6: Electron arrangement for arc discharge in water [225]

Lange and Walton, carry out a detailed study of the plasma region by performing comparative work between arc discharge in helium atmosphere and an arcuated discharge in deionized water. As the plasma reaction environment can efficiently lead to cooling reagents and to intensifying coalescence processes, these authors have determined spectroscopically the temperature distribution and identified the intermediate species present in the plasma. They also determined the selectivity of this process in the generation of nanomaterials, i.e. which types of nanostructures are formed simultaneously during CNO production.

The average temperature inside the plasma bubble in deionized water is very high, with values ranging from 4000 to 6500 K. While in the arc discharge in it, under the same experimental conditions, the temperature was found to be about 1500 K lower than that of the arc discharge in water. Authors attribute the upper plasma temperature to water in the presence of bubbles, which being smaller in volume and number, lead to a high-energy density. At atmospheric pressure, the degree of water dissociation, in atomic and hydrogen oxygen, is higher than 99% at a temperature of 5000 K.

Imasaka in 2006 [226] presents a work involving intermittent arc discharge in water for the production of CNOs and CNTs

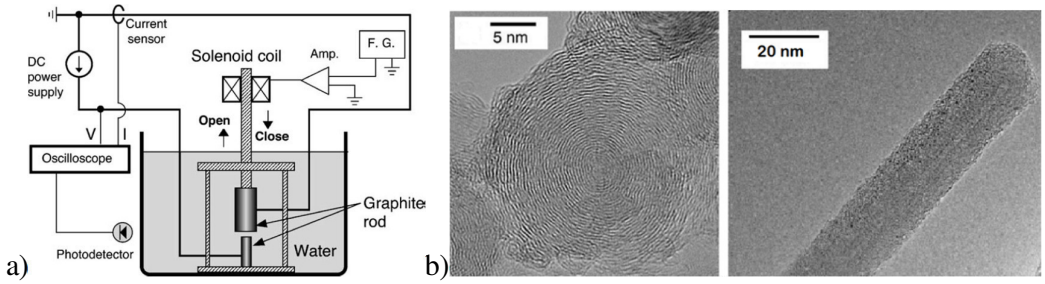

Figure 4.7: a) Experimental apparatus of intermittent arc discharge, b) TEM images showing the presence of CNOs and CNTs [228]

In this particular case, the anode (6 mm diameter) is kept fixed, while the cathode (diameter 10 mm) moves up and down. The intermittent discharge is mechanically obtained by touching the cathode at the fixed anode and then disconnecting it. This vertical motion is maintained by the electromagnetic force produced by a solenoid coil. The motion repetition rate is 15-20 pps (pulses per second). Again, the samples taken on the surface of the water inside the reaction chamber show the presence of CNOs and CNTs (Figure 4.7). During the discharge process, the graphite electrodes evaporate and consume gradually. The (Figure 4.8) shows the relationship between the mass of electrodes consumed during discharge as a function of the total energy of the intermittent arc. What is being observed, and that both electrodes are consumed during discharge

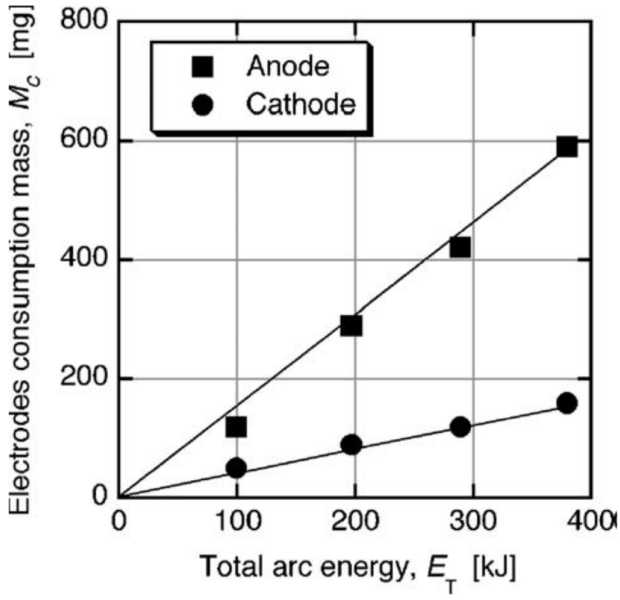

Figure 4.8: Dependence on the consumption of electrodes mass by intermittent arc energy [226]

In 2007, Palkar [227] presented a work in which it compares CNOs obtained from Nano dynamic spotting (NDs) and arc discharge into water. Samples obtained by arc discharge, were subjected to thermal treatment (400 ° C) for 1h to eliminate amorphous carbon. Most of the CNOs show a nucleus higher than that of fullerene C_60 (1 nm) (Figure 4.9).

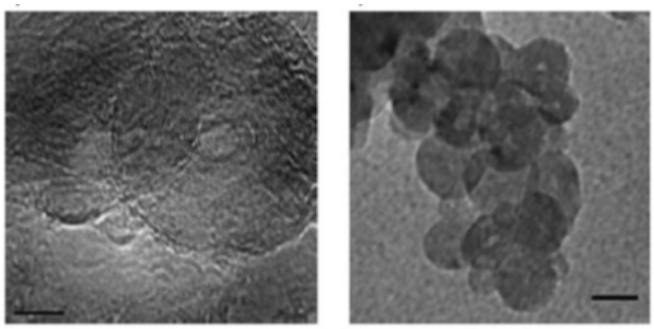

Figure 4.9: A-CNO TEM images after treatment at 400 ° C for 1h [227]

Synthesis of Carbon Nano-onions.

The technique used for the production of CNOs is the Arc Discharge in deionized water (Underwater Arc Discharge). This technique has made it easy to simplify the synthesis process, eliminating the use of vacuum systems and catalysts, which were then eliminated through a purification process, thus extending the time and production costs.

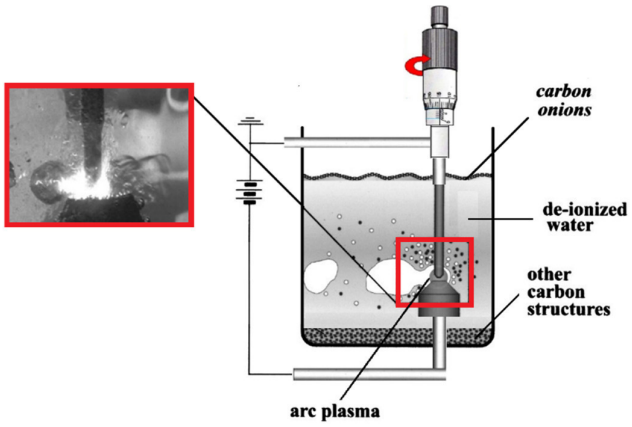

Figure 4.10: Scheme of the experimental apparatus used for the synthesis of CNOs (the digital image showing the formation of the plasmatic environment).

In the underwater arc discharge synthesis process, the plasma-generated bubble acts as a reaction chamber where the carbon atoms evaporated from the anode surface cluster near the surface of the water forming carbon nanostructures. Plasma parameters determine the type of structure that is formed and the amount of defects.

We created a metallic structure, consisting of two stainless steel flanges held together by three threaded columns (Figure 4.11). The upper plate was drilled in the center to allow assembly of the micrometer that would allow a good accuracy of advancement of the anode towards the cathode. Therefore, the micrometer allows the translation towards the cathode during discharge, which is indispensable in maintaining the *gap* constant. The lower plate, instead, is characterized by a ceramic zone which isolates it electrically from the rest of the chassis; the cathode stands, made of copper, was precisely mounted on this area [229].

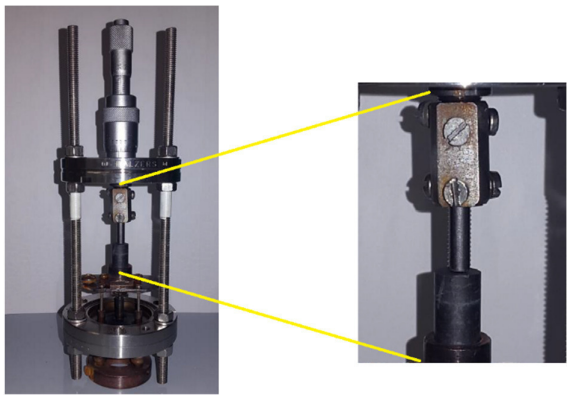

Figure 4.11: Mechanical component of experimental apparatus (the enlarged image shows anode and cathode positioned in their respective electrodes).

The electrical component consists of a power supply of 5 Kw of power which allows us to reach a current of 80 A and a potential difference in the 0-24 V range and at the output of the rectifier bridge we have two cables to connect to the anode and cathode. This is very important for maintaining the constant current arc during discharge Figure 4.12.

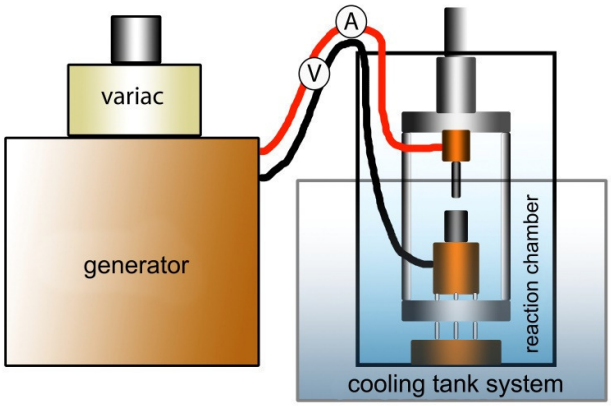

Figure 4.12: Diagram of apparatus for synthesis of CNOs by arc discharge in water

Two high purity graphite rods (Sigma Aldrich) were approached in deionized water (1.4 MOhm) while applying a bias potential between them. The electrode diameters were 5 and 10 mm for the anode and the cathode, respectively, and they were mounted on an apparatus submerged in a 1000 cm^3 beaker. The apparatus allowed to translate the anode and to rotate it along its axis at about 20 rounds per minute. The roto-translation allowed to approach the anode to the fixed cathode, and to maintain a stable discharge on time intervals of the order of 3 minutes. We found the best discharge conditions for a bias potential of 12 V and a current of 30 A. The arc discharge in water was stable maintained anode-cathode gap of about 1 mm. The discharge can be characterized as an anodic arc as the smaller anode electrode is consumed. The discharge proceeds until the almost total consumption of the anode, maintaining the synthesis chamber temperature under control: in our case, starting from a temperature equal to the ambient temperature (T=25°C) after approximately 70 seconds, a temperature of 83°C was reached, which was kept constant until the end of the discharge [229].

Figure 4.13: Digital image of the experimental process during arc discharge between anode and cathode of graphite.

A cylindrical-shaped black hard deposit of about 3 mm diameter was weakly bound to the surface of the cathode, and it was possible to remove it by applying a weak lateral force as shown in Figure 4.14.

Figure 4.14: Discoid formed on the cathode after arc discharge process.

The discoid sample was divided to two pieces, one heated to 400 °C (2 hours) and the other without heating, then they have been converted to powder using a grinding machine, and the resulting powder materials of discoid samples were collected (Figure 4.15).

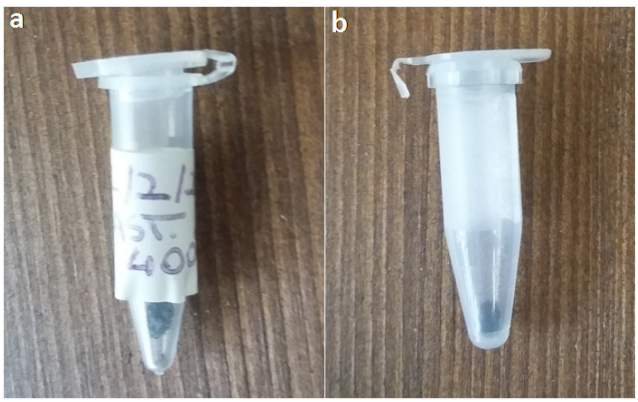

Figure 4.15: Agglomerates formed on the cathode, a) heated to 400 °C, b) without heating.

Other three sample groups were individuated from the synthesis chamber: powder floating on the water surface, the material precipitated on the bottom of water, and discoid formed on the cathode. Thus, a powder dispersed in water was formed, partially floating and partially dropping at the bottom of the beaker as shown in Figure 4.16.

Figure 4.16: Powder dispersed and floating in water after by Arc Discharge process.

The floating material was recoiled by a microscope slide, while the bottom material was obtained by evaporating water at 80 °C. A cylindrical-shaped black hard deposit of about 3 mm diameter was weakly bound to the surface of the cathode, and it was possible to remove it by applying a weak lateral force. The dispersed samples (floating and bottom) were ultrasonicated in ethanol (Hielsher P100, 30 KHz, 100 W, 100%) for 30 minutes. To study the materials contained in the hard deposit it was necessary to grind it for four hours in a boiling mill machine (Fritsch Analisette 3, 3000 oscillations per minute). The resulting dust was suspended in ethanol [229].

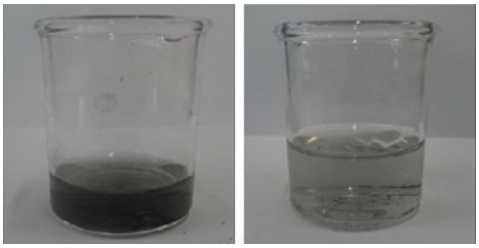

Figure 4.17: Suspensions obtained after sonication of material collected in reaction chamber: (left) collected on bottom of reaction water (right) from the surface the reaction water.

4.3 Results and discussion

The experimental arrangement, which allows the rotation of the anode when approaching the cathode, is probably the key point to obtain stable discharges. In fact, the rotation prevents

the stabilization of strong local discontinuities in the arc, allowing the formation of well-defined cathodic deposits [229].

All samples were studied by transmission electron microscopy (Jeol JEM 1400 Plus, 80 kV). TEM images reveal that the surface and bottom samples are conformed by same CNPs, although they were obtained from different zones of synthesis chamber clearly showing the presence of carbon nano-onions (CNOs) and carbon nanotubes (CNTs) of various dimensions, and also some thin structures. Figure 4.18 shows agglomerates of CNTs with CNOs surrounding. The CNOs present dimensions of the order of tens of nanometers and CNTs with diameters of the order of some nanometers.

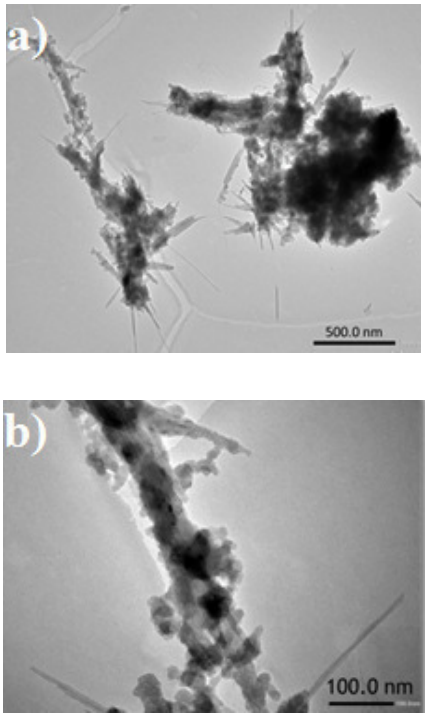

Figure 4.18: a) TEM image shows agglomerates of different carbon nanoparticles: CNTs, CNOs and lamellar structures, b) Zoom image shows agglomerates formed only of CNOs and CNTs.

TEM results showed that dispersed nanomaterials collected floating or at the bottom of the beaker, have the same properties, for this reason it´s called DISP samples. On the contrary, the samples obtained by grinding the deposit, that it´s called DEP samples, were homogeneous. The TEM image in Figure 4.19a is representative of the DISP samples, showing CNOs with other nanoparticles, mainly CNTs and layered structures. The image in Figure 4.19b shows that the DEP samples are made almost only of CNOs, with average radius of the order of tens of nanometers [229].

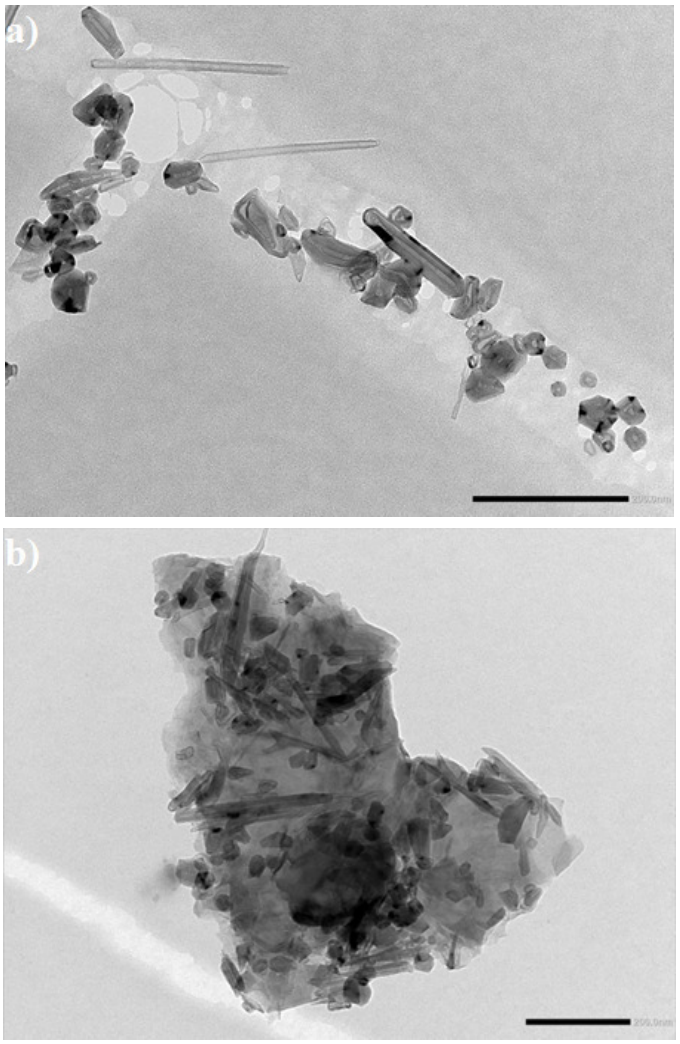

Figure 4.19: TEM images of a) DISP and b) DEP samples, both dispersed in ethanol.

Different results respect to the discoid was observed on samples obtained by the grinded dust of the solid discoid fragmentation formed in the plasmatic zone. The TEM characterization of this discoid sample (Figure 4.20), shows the presence of fragments consists a large proportion of CNOs with dimensions estimated at tens of nanometers.

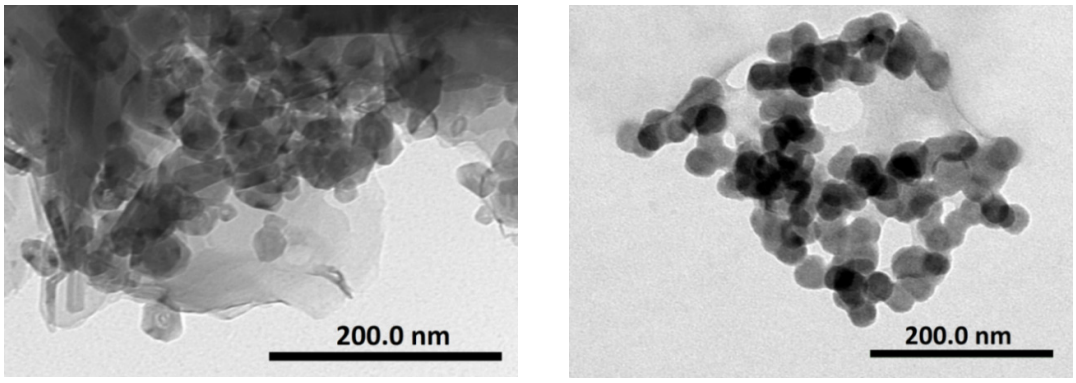

a) b)

Figure 4.20: TEM images: a) agglomerates of different CNPs (with CNOs in larger quantities). b) agglomerates formed only of CNOs.

The best results have been obtained when we heated a part of the discoid fragment at 400°C by 2 hours; subsequently, they were milled for 4 hours using a planetary milling machine (Fritsch Pulverisette), and then sonicated in distilled water for 30 minutes (Hielscher UP100H, 100 W, 30 kHz, 100%) to obtain a fine powder of the CNPs. The TEM characterization of this sample (Figure 4.21), shows the presence of fragments consisting exclusively of CNOs. More precisely, it can be observed in some fragments a polyhedral structure of CNOs with dimensions estimated at tens of nanometers [229].

a) 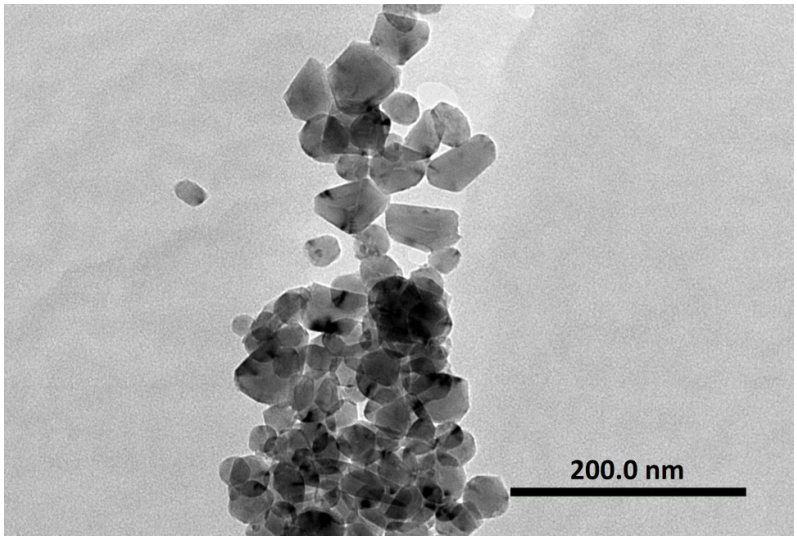

b)

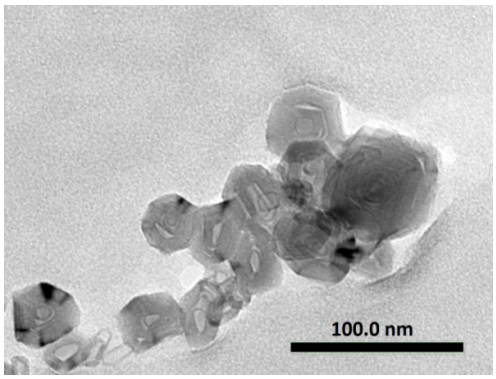

c)

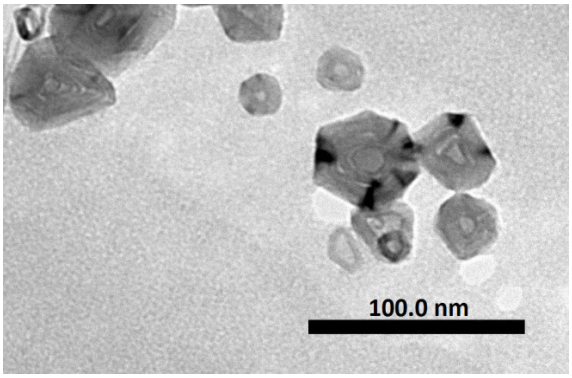

Figure 4.21: TEM images of grinded discoid sample: a) Fragment consisting of only CNOs, b) here it showed clearly polyhedral structures of CNOs and c) polyhedral CNOs with dimensions between 30 and 50 nm.

The average radius of 245 CNOs has been measured in some TEM images as the Figure 4.22 shows.

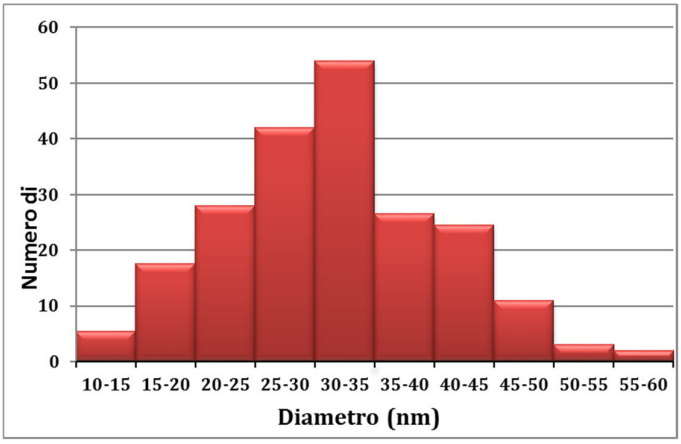

Figure 4.22: Histogram of the distribution of 245 CNOs diameters observed at TEM on the sample Dep.

The difference between CNOs suspended in water and those found in the deposit is evidenced in Thermogravimetric Analysis (TGA) measurements, shown in Figure 4.23. Full line in Figure 4.23a is the curve obtained in the DISP sample. The whole sample is burned at 850 °C, and the slope changes indicate the inhomogeneity also observed by TEM in Figure 4.19a. The dashed curve in Figure 4.23a, obtained on the DEP sample, indicates a much higher stability, that allows almost 30% of the initial mass to be still present at 850 °C. Moreover, the regular shape of the curve confirms the sample homogeneity observed in Figure 4.23b. Figure 4.23 also show the TGA results of Palkar et al. [227] on CNOs obtained by purification of the material collected either on the top or the bottom of the water vessel after underwater arc discharge. Full- and dashed-line refer to pristine CNOs and to CNOs annealed at 2300 K in it atmosphere, respectively. The comparison of the two dashed curves in Figure 4.23 shows that CNOs dispersed in water reach a thermal stability comparable to that of DEP CNOs only after thermal annealing in it, which very likely allows to decrease the density of defects in graphitic planes [229].

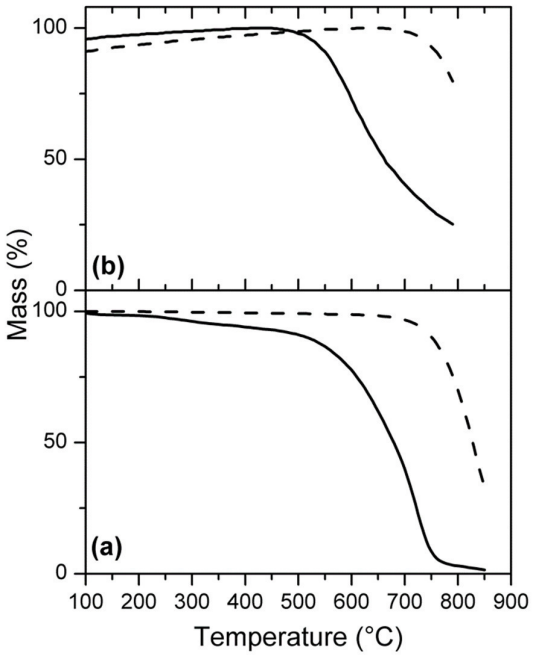

Figure 4.23: a) TGA measurements obtained with the DISP sample (full curve) and on the DEP sample (dashed curve). b) TGA results for CNOs obtained by purification of dispersed materials in arc discharge experiments, without thermal treatment (full line) and with a thermal treatment at 2300 K in the atmosphere (reproduced from ref., permission to be obtained).

The above results show that in underwater arc discharge experiments two kinds of CNOs are formed, found dispersed in water (DISP) and in the cathodic deposit (DEP). The

formation of the DISP- and DEP-type CNOs can be explained by the model proposed by Sano et al. [191], although some points regarding that model have to be addressed.

Lange et al. [228] have shown by plasma spectroscopy that in arc discharge in water between graphite electrodes, the strongest bands are those coming from C_2 radicals, carbon atoms and ions, atomic hydrogen and oxygen. The model supposes that CNTs are formed in the zone very close to the plasma, but this hypothesis is in contrast with the existence of the cathodic deposit. In fact, the deposit is formed in the hotter zone of the discharge, and is composed mainly of CNOs. The crystallization of such CNOs cannot be ascribed to a temperature gradient due to the presence of surrounding water. It is hard to measure the local temperature of the cathode surface, but clearly it is always lower with respect to the anode, due to the fact that the anode is bombarded by electrons, and also due to the dimensions of the cathode. For this reason, the cathode is not eroded during the discharge, and its surface remains unaltered after the removal of the deposit. Moreover, during and immediately after the discharge the cathode does not emit in the visible. Taking in mind that the surface of the cathode is very close to the plasma zone, in which the temperature can be higher than 6000 K [228], a strong temperature gradient must exist in the space very close to that surface. Carbon ions evaporated from the anode and coming onto the cathode, very likely crystallize in this temperature gradient. The resulting nanoparticles are formed in an environment with temperature much higher than the environment in which particles dispersed in water crystallize. The high temperature environment could also explain why the cathodic deposit contains mainly 0D nanoparticles. In fact, it has been shown that under intense electron beam irradiation, tubular carbon structures convert in quasi-spherical particles made of concentric graphitic shells [136].

Figure 4.24 shows the mechanism we propose for the formation of the discoidal agglomerate made of CNOs. Such formation can only be explained if we assume that the synthesis of the nanostructures occurs in the plasmatic zone because of the temperature gradient very close to the cathode surface, and that such nanostructures are deposited on the cathode, forming the discoid of CNOs [229].

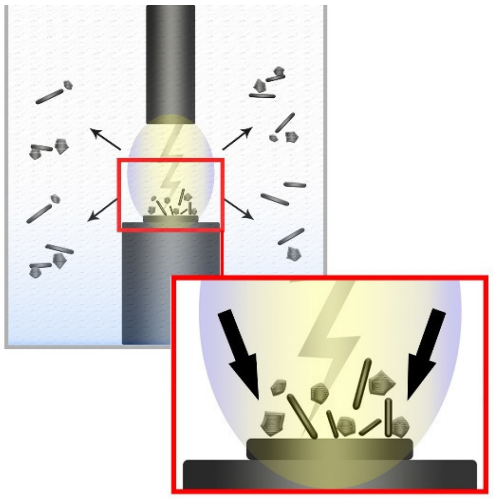

Figure 4.24. Schema of the mechanism of formation of CNPs in our synthesis.

4.4 Conclusions

We have shown that using a novel experimental apparatus, we obtain cathodic deposits in underwater arc discharge between graphite electrodes composed mainly of OD CNOs, with high level of order on the graphitic planes, whereas the latter are randomly stacked. The mechanical fragmentation of the deposits allows to obtain CNOs without any purification procedure. Our results indicate that these CNOs have different properties with respect to CNOs dispersed in water, mainly regarding the structural order in the graphitic planes. We have proposed a model for the formation of the deposit, in which the crystallization is driven by an intense temperature gradient in the space very close to the cathode surface.

Chapter 5

Theoretical Modelling and Electronic Properties of Carbon Nano-onions

5.1 Introduction

Since the discovery of the fullerene C_{60} in 1985 [230], carbon materials have attracted the interest of physical chemists. In the follow years, several other carbon nanomaterials were discovered as carbon nanotubes (CNTs), carbon nanohorns, nanodiamonds, as well as graphene. Sumio Iijima discovered multi-shell fullerenes, named carbon nano-onions (CNOs)or onion-like carbon, in 1980 looking at a sample of carbon black in a transmission electron microscope [231]. The multi-shell icosahedral fullerenes are often smaller than 10 nm and consisting of various carbon shells enclosed each into another, in addition, they could be classified in spherical or polyhedral fullerenes, depending on the curvature of the graphene faces in the optimized structures.

Mordkovich and Takeuchi produced double and triple-shell fullerenes with diameters of 1.4 nm and 2 nm with high yield [232] by the laser evaporation method at 0.1 Torr. Another way for preparing CNOs is by annealing ultra-disperse nanodiamonds at temperatures above 1200 K [234]. However, the most common method for carbon onions synthesis is the graphitization of nanodiamonds at high temperatures (>1700°C) in an inert gas or vacuum. The resulting CNOs show typical sizes smaller than 10 nm and present a high degree of carbon ordering [233]. Although TEM imagines and Raman spectra are available in literature, crystallographic patterns necessary, to resolve the CNOs structures as well as to elucidate the relationships between the CNOs structures and preparation routes are rare or absent. L. Hawelek *et al.* [235] studied the transformation of ultradispersed diamond nanoparticles with diameters of 5 nm into CNOs by high-energy X-ray diffraction and molecular dynamics simulations (MD). Structural models have been proposed for nanodiamonds annealed at 1673 K, 1973 K and 2273 K. The structure factors and the pair correlation functions obtained by these structural models are in agreement with experimental data, providing valuable information about the geometries of such complicated carbon nanoparticles. The authors reported that defected icosahedral fullerenes describe satisfactorily the atomic arrangements of the annealed samples. The conversion of the outer diamond-like part into the icosahedral or

quasi-icosahedral fullerenes can be considered as confirmation that the graphitization process kicks off from the outer part of nanodiamonds at higher temperatures. Then, the initial diamond atomic arrangement is completely converted into the sequence of the quasi-icosahedral polyhedral carbon shells. Giant polyhedral carbon nanoparticles exhibit large graphene facets connected with curved or sharp zones, clearly visible by the high-resolution transmission electron microscopy (TEM) imagines and Raman spectroscopy [236].

Spherical or polyhedral multi-shell fullerenes are widely studied thanks to their interesting electronic and mechanical proprieties. Several theoretical works investigated the structures and the electronic proprieties of multi-shell icosahedral fullerenes [237-242]; however, comparative studies on their electronic features as function of particle sizes and number of concentric shells are scarce. The valence electronic properties of models in a smaller scale of the structures shown in the Pujals et al. [236] paper were studied in this work. As result, validated structures [243-244] of icosahedral polyhedral fullerenes were used herein to get some electronic proprieties such as H-L gap, electron affinity, ionization potential, electronegativity, global hardness and DOS in the frame of the Density Functional Theory (DFT). To study the effect of an additional shell on the electronic features of a smaller polyhedral fullerene as function of the particle size, the computed aforementioned proprieties were compared.

5.2 Modelling of Polyhedral Carbon Nano-onions

The formation of polyhedra has attracted much interest as an attractive research topic that is connected with computational chemistry. Here, we focus on the grow law of so-called Goldberg method based on Platonic polyhedra. The elegant structure of polyhedra makes it one of the basic forms of physical existence in nature. Platonic solids, the five simplest polyhedra with all faces regularly, have attracted the special attention of physicits and chemists as structural models time and again since antiquity. The five Platonic polyhedra are tetrahedron, cube, octahedron, dodecahedron and icosahedron.

There are several ways to build cages of CNOs. For example, in the Goldberg method proposed in ref. [245], which consists of three steps: splitting, adding and assembling. The first step is splitting, which means to break a dodecahedron down into twelve regular pentagonal pieces, as shown in Figure 5.1.

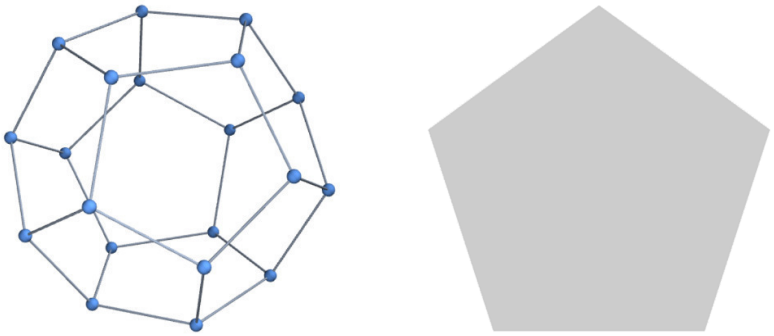

Figure 5.1: The operation of breaking a dodecahedron into twelve regular pentagonal pieces

The second step is adding, which refers to inserting several hexagons in twelve pentagons of a dodecahedron in a coherent way. The fact that hexagons are added to one pentagon of a dodecahedron regularly is shown in Figure 5.2

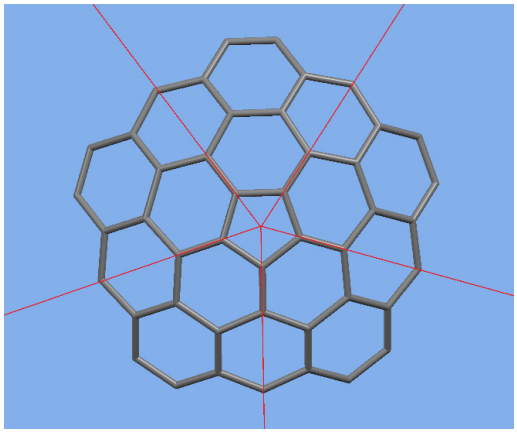

Figure 5.2: Adding hexagons to a pentagon in a coherent way.

The third step is assembling, which indicates that assemble all twelve parts in which hexagons are added to pentagons regularly.

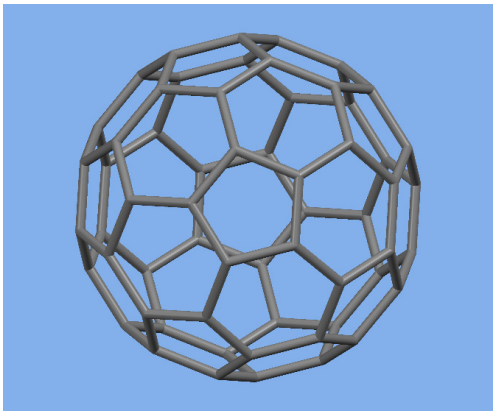

Figure 5.3: The 60-hedron contains 12 pentagons and 20 hexagons, with diameter of 0.64 nm.

The study of the Goldberg method, from Figure 5.1 to Figure 5.3, reveals two outstanding properties:

a. The resulting polyhedral are vertex regular and the degree of vertex remains unchanged during the construction. For example, the degree of extended dodecahedron is three, the same as the initial dodecahedron.
b. The symmetrical property of the Platonic polyhedral is one which remains unchanged when adding regular polygons. Given an extended dodecahedron with I or I_h, the initial pentagons lie on the axes of rotation of order 5, while the positions of 2- and 3- fold the axes are at the edges and centers of hexagons.

On the other hand, two series of extended Goldberg polyhedral were constructed from Goldberg polyhedral, which preserve icosahedral symmetry. The Greeks described two classes of convex equilateral polyhedron with polyhedral symmetry, the Platonic (including the tetrahedron, octahedron, and icosahedron) and the Archimedean (including the truncated icosahedron with its soccer-ball shape). Johannes Kepler discovered a third class, the rhombic polyhedral. Some carbon fullerenes, inorganic cages, icosahedral viruses, protein complexes, and geodesic structures resemble these polyhedral. Here we add a fourth class, **"**Goldberg polyhedral.**"** Their small (corner) faces are regular 3gons, 4gons, or 5gons, whereas their planar 6gonal faces are equilateral but not equiangular. Unlike faceted viruses and related carbon fullerenes, the icosahedral Goldberg polyhedral are nearly spherical.

Stan Schein and James Maurice Gayed [246] recently published the structures of merely equilateral single-wall icosahedral cages having a nonplanar 6gons boat-shaped. The optimized structures of the merely equilateral icosahedral fullerenes, proposed Schein and Gayed, were used herein as benchmark since these show morphologies in a smaller scale very similar to the aforementioned giant polyhedral carbon nanoparticles reported in the TEM images of the Pujals *et al*. paper having diameters greater than 50 nm and many thousands of carbons. [236].

The considered merely equilateral icosahedral fullerenes are quasi-polyhedral models where flat facets and the curved zones are clearly visible in agreement with the mentioned TEM images [247]. Schein and Gayed to achieve their optimized merely equilateral icosahedral cages used initial geometries obtained with two different procedures. For cages with less than 250 vertices they used Carbon Generator code (CaGe) [248-249], while for structures with vertices greater than 250 they followed the algorithm shown in Figure 5.1 of

their work in conjunction with Adobe Illustrator and UCSF Chimera [250-251] scripts. Both procedures yield the pdb files used in subsequent optimizations in order to obtain the merely equilateral icosahedral structures carried out with Spartan code [252].

Unlike Schein and Gayed, here, just a homemade algorithm [282] has been implemented in Wolfram Mathematica v.11 [252] to build equilateral icosahedral single and multi-wall fullerenes having any vertices number following the procedure illustrated in Figure 5.4 of Schein and Gayed's work [246]. In detail, icosahedral polyhedral fullerenes can be built starting from a two-dimensional graphene sheet, without resorting data to other codes or database. Each of the triangular facets of an icosahedron has been decorated by the Goldberg's triangles with T vertices connecting them according to the subsequent geometric constraints. The C-C bond lengths must be equal to the carbon-carbon experimental length as found in a graphene sheet or in the pentagonal carbon ring of fullerenes, i.e. in well-established carbon nanostructures, while the bond angles were defined equal to 120° (hexagonal ring) or 108° (pentagonal rings) [246]. Goldberg triangles with indexes (*h*, 0), i.e. equilateral triangles as shown in the Figure 5.4a, were used to decorate each 20 triangular facets of the icosahedra with increasing sizes. Each Goldberg triangle contains a number of vertices given by the well-known relationship $T=h^2+hk+k^2$; triangles with vertices ranging from 1 to 81 were used herein.

a)

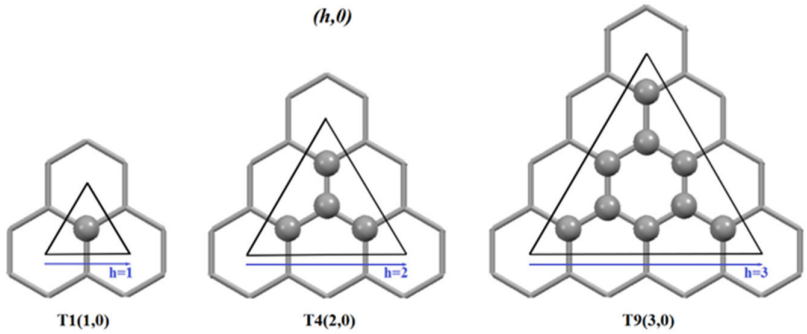

b)

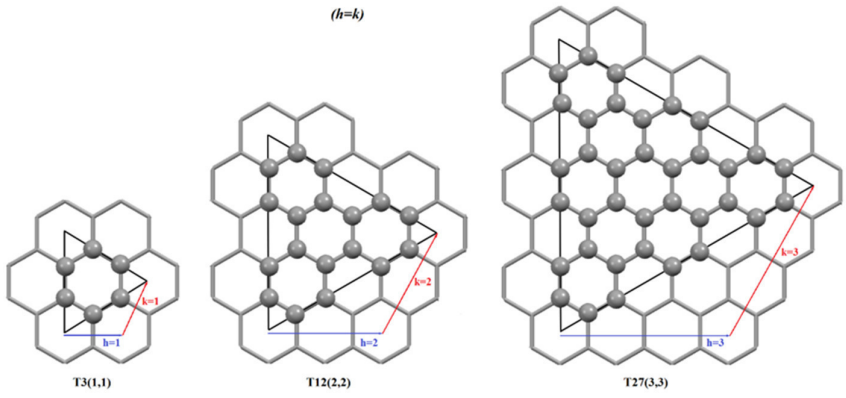

c)

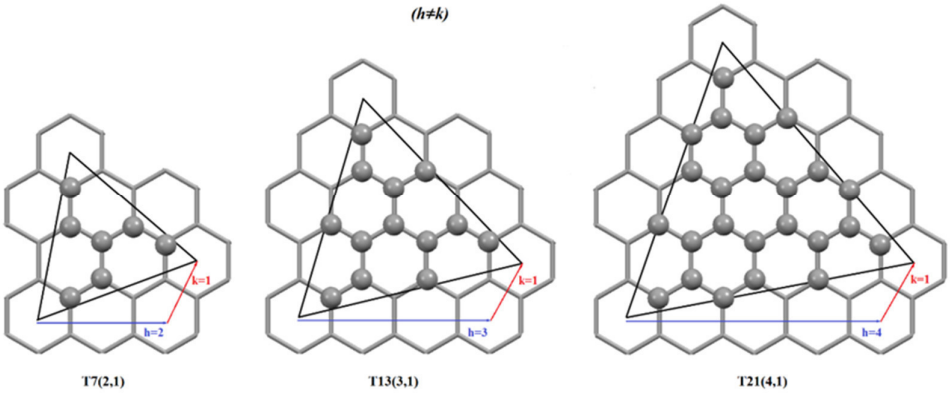

Figure 5.4: Goldberg triangles: a) (*h*, 0) family with T = 1, 4, and 9,b) h = k family with T = 3, 12 and 27, and c) h ≠ k family with T = 7, 13 and 21.

The process to assemble an icosahedral cage with this algorithm is simple:

a. A regular icosahedron is constructed

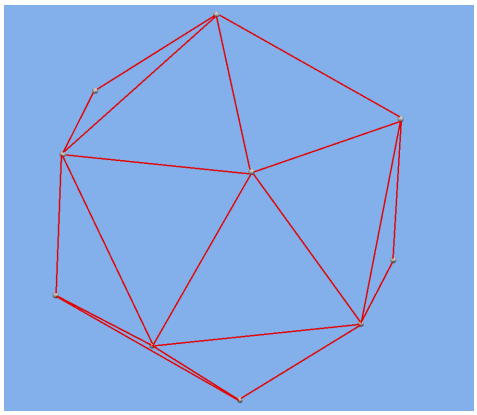

Figure 5.5: Regular Icosahedron

b. The Goldberg´s triangle is constructing (for example T=16; (4,0)) from a graphene sheet.

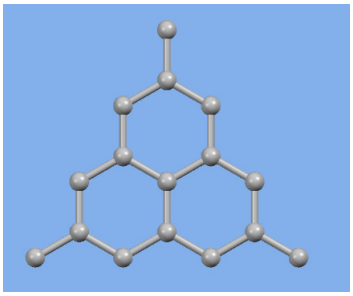

Figure 5.6: Goldberg´s triangle for T=16.

c. A *rotation matrix,* rotates the Goldberg´s triangle

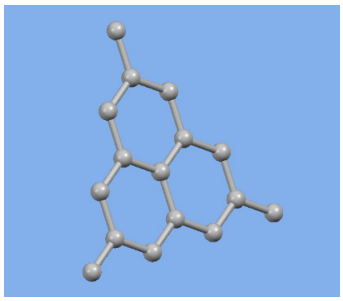

Figure 5.7: Goldberg´s triangle is rotated in the space.

d. A second matrix is used, a *translation matrix*, to move the Goldberg´s triangle over an icosahedron face

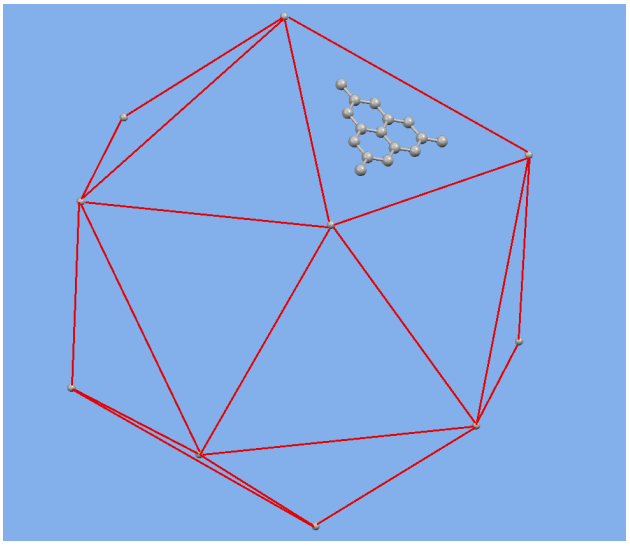

Figure 5.8: Goldberg´s triangle over an icosahedron face.

e. This process is repeated for all icosahedron faces.

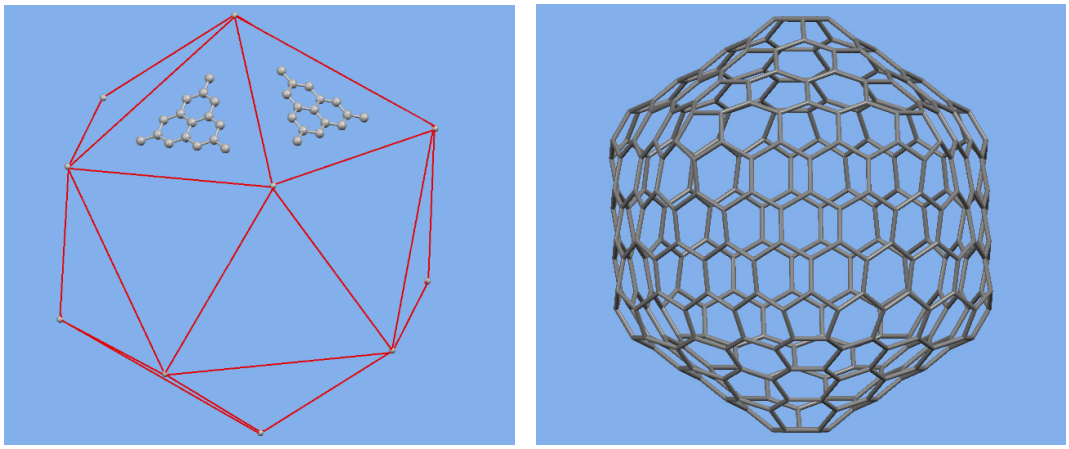

a) b)

Figure 5.9: a) Goldberg´s triangle over two icosahedron faces b) Single-Wall Polyhedral icosahedral fullerene C_{320}, (T=16; (4,0)), merely equilateral with diameter of 1.50 nm.

The resulting icosahedral cages show 20T vertices, 6gonal faces and 12 pentagons as corner faces. The structures derived by the aforementioned algorithm show planar faces with equal bond lengths (equilateral) and equal angles in the *internal* 6gons, hence they are geometrically polyhedral although the 6gons joining two triangular icosahedron facets display a boat-shape. It is worth noting that the 6gon faces in icosahedral Goldberg polyhedral are equilateral and planar, but not equiangular.

In the Figure 5.10 is showed some cages of polyhedral fullerenes for different (h, k) index.

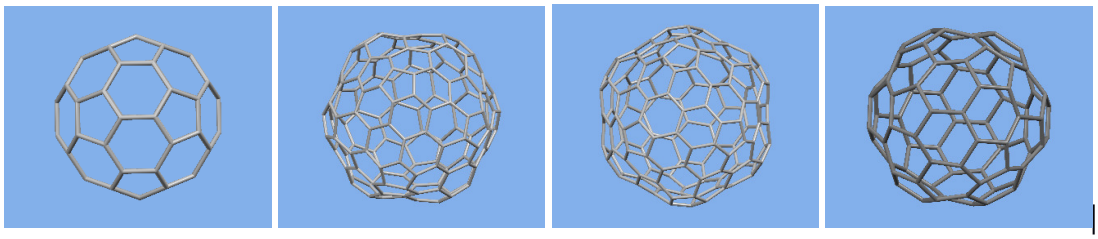

a) b) c) d)

Figure 5.10: Single-Wall icosahedral polyhedral Fullerenes (SWipF): a) T=3, (1,1); b) T=7, (1,2); c) T=7, (2,1); d) T=4, (2,0) with diameters of 0.64, 1.06, 1.06 and 0.76 nm respectively.

The Table 5.1 shows the first results for the (h, 0) Index and $C20N^2$ family.

Table 5.1. SWipF geometrical properties

Index (h,0)	T	Atoms Number	Dimension (nm)	6gons Number
(1,0)	1	20	0.39	0
(2,0)	4	80	0.76	0
(3,0)	9	180	1.13	1
(4,0)	16	320	1.49	3
(5,0)	25	500	1.86	6
(6,0)	36	720	2.23	10
(7,0)	47	980	2.59	15
(8,0)	64	1280	2.96	21
(9,0)	81	1620	3.32	28
(10,0)	100	2000	3.69	36
	h^2	$20h^2$		

The graphene facets with T=4, 9, 16, 25, 36 and 49 of single-walled fullerenes as obtained by the homemade algorithm were compared with those of the merely equilateral

fullerenes optimized by Scheina and Gayed and hence used as benchmark. The Root Mean Square Displacement, referred to the angles ($RSMD_{angles}$) shown in the relative figures of Appendix A, were calculated, in addition to the differences between the dihedral angles, ΔD, whose definition, is showed in Appendix A. The highest $RSMD_{angles}$ was 2.98° while the ΔD difference was 1.57° for the T=4, therefore the comparison resulted good that means that the structures used here are very close to the optimized merely equilateral icosahedral fullerenes.

A single-wall icosahedral fullerene with diameter equal to 2.59 nm obtained using the homemade algorithm is shown in Figure 5.11.

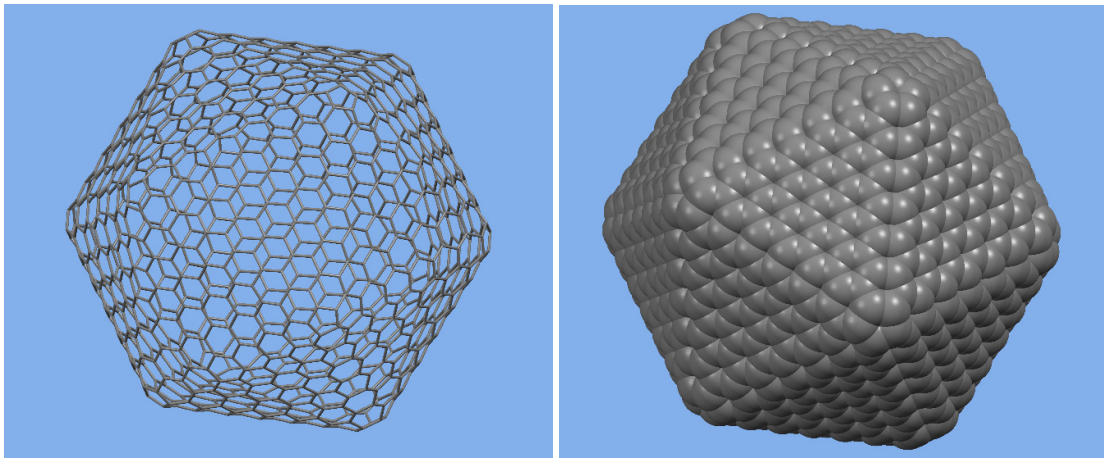

Figure 5.11: Single-wall icosahedral fullerene obtained by assembling of Goldberg's triangles with T= 49 with diameter of 2.59 nm

It is worth noting that, various public distributed utilities can be used for building icosahedral fullerenes, e.g. Fullerene [254-256] and Crystal [256] as well as Turbomole [257], however, considering the good agreement between the merely equilateral icosahedral fullerenes, proposed Scheina and Gayed, and the structures obtained through the homemade algorithm, the latter were used in this work. It is interesting to note that Yves Noël et *al.* [258] built single-wall icosahedral fullerenes starting from Goldberg's triangles but with $h = k$ indexes using the Crystal code [256]. After geometry optimizations, they compared the positions of atoms on each nanoparticle face with an ideally flat graphene triangle appropriately collocated. For (8,8) (9,9) and (10,10) fullerenes they obtained marked differences between the face Goldberg's triangles and the ideal graphene triangle; less marked differences were obtained for (5,5) (6,6) and (7,7) single-walled nanoparticles. Noël et *al.* evaluated also the distribution of the C-C bond lengths in the investigated fullerenes. The authors found a wider distribution around to the graphene C-C lengths as the fullerene size grows. These data demonstrate that significant distortions from flat triangular faces are present in the analysed (*n,*

n) single-wall fullerenes unlike the structures optimized by Schein and Gayed, very similar to those used herein. In the literature, a long discussion is addressed about the question of the giant fullerenes prefer a faceted (polyhedral shape) or a spherical shape [259-260]. As pointed out Calaminici et al. [260], their first-principle based structure optimizations predict that larger fullerenes, C_{240}, C_{320}, and C_{540}, prefer a faceted shape.

Moreover, even for the smallest fullerene, i.e. C_{180}, there is clear evidence that the faceted shape is preferred over a spherical shape if all-electron optimizations without any symmetry restriction are performed [261]. These conclusions are in agreement with most of the previous reported theoretical studies [260] [262-263]. However, the question is not the aim of this study because the electronic proprieties of smaller models similar to the structures shown by the TEM images in the Pujals et al. [236] paper were analysed herein.

The assembling of Goldberg's triangles on accumulated dodecahedron following the illustrated procedure was also carried out herein and the obtained single-walled accumulated dodecahedron fullerene was shown in Figure 5.12 [282].

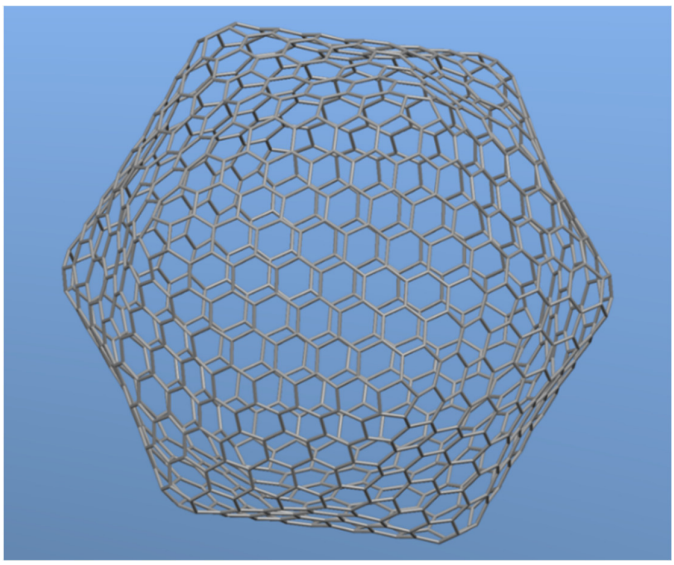

Figure 5.12: Single-wall accumulated dodecahedron fullerene with a diameter of 3.23 nm obtained by assembling Goldberg's triangles with T=16

With the assembly of Goldberg's triangles, it is possible to construct a class of fullerenes where between two adjacent faces, there is a curved sheet of graphene, i.e. a piece of nanotube, and

where the five faces converge there is a curved capped, i.e. a piece of spherical fullerene as the Figure 5.13 shows. These last two cases are particular cases of the same algorithm.

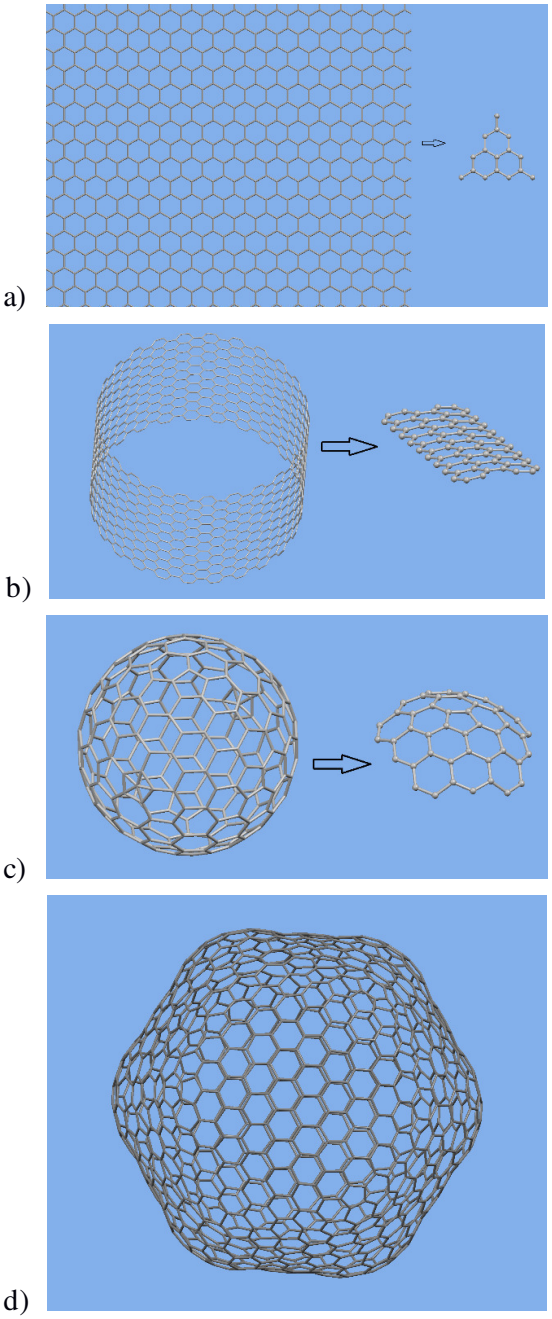

Figure 5.13**:** Single-wall curved fullerene with diameter of 2.96 nm obtained by assembling: a) Goldberg's triangle (3,0); b) a piece of CNT (15,15) and c) a caped of a spherical fullerene C240; d) curved fullerene C_{980} with diameter of 2.96 nm.

Once built the icosahedral single-wall nanoparticles, the assembling of concentric fullerenes is also possible, as pointed out in the Doore *et* al. [237] work whom defined carbon nano-onions by concentrically stacking of individual single-walled spherical fullerenes with

optimized geometry. A three-wall icosahedral fullerene was also built and shown in Figure 5.14. The interlayer distance between two concentric shells was 0.36 nm. This result is in excellent agreement with the experimental graphene interlayer distance, i.e. 0.34 nm [270-271] and it was obtained by the assembling of concentric shells once verified that each of them are in good agreement with the structures proposed by Schein and Gayed, without subsequent adjustments.

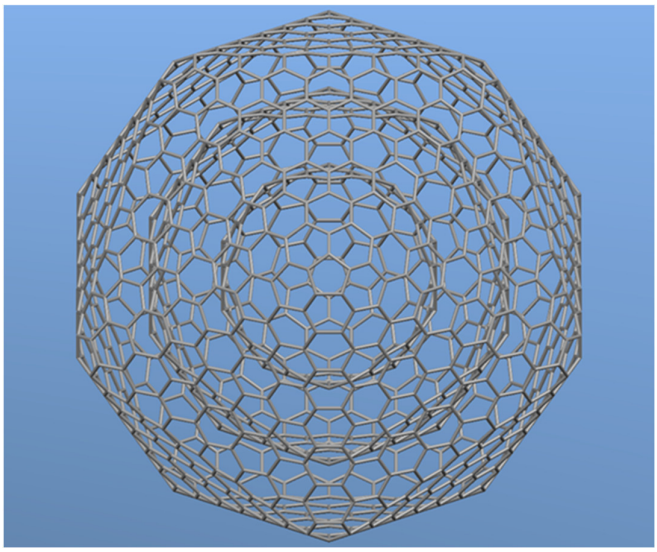

Figure 5.14: Three-wall icosahedral fullerene obtained by assembling of Goldberg's triangles with T=9, T=25 and T=49 vertices for the smaller, medium and larger shell, respectively. The external diameter is 2.59 nm.

5.3 Computational Details

The models of the single and double wall icosahedral fullerenes were used to evaluate some key electronic proprieties. The Quantum Mechanics calculations were carried out in the framework of Density Functional Theory using the Northwest Computational Chemistry Package (NWChem) [270-271]. All calculations were performed for closed-shell electronic configuration using the exchange-correlation PBE functional [272], in a Generalized Gradient Approximation. This functional has been widely used in several density functional calculations concerning graphene structures with a good reliability [273-275]. Linear combinations of Gaussian-type orbitals with Coulomb and exchange-correlation potentials numerically

integrated on an adaptive grid with accuracy equal to 10^{-5} were used. A double-ζ orbital basis set augmented with a valence polarization function for all the electrons of the carbon atoms was employed. The energy convergence threshold for the self-consistent field procedure and for the root mean square of the electron density were set to 10^{-6} (a. u.) and to 10^{-5} (a. u.), respectively. No level shift or smear values were imposed to accelerate the convergence of the Kohn-Sham equations and any symmetry constraint. Recently, A. Erba *et al.* [275] reported large-scale DFT calculations on a giant single-wall icosahedral fullerene. They used the same functional and double-ζ orbital basis set, but with two polarization functions. Also P. Calaminici *et al.* [260] carried out fully geometry optimizations of single-walled fullerenes (i.e. C_{180}, C_{240}, C_{320}, and C_{540}), using a linear combination of Gaussian-type orbitals in the frame of density functional theory. Their calculations were performed for singlet configuration with double-ζ plus valence polarization (DZVP), but in the Local Density Approximation. Although the level of the theory used herein and the above works are very similar, however, these authors analyzed only single-wall fullerenes obtained from Goldberg's triangles with different indices.

5.4 Results and Discussion

Shown in Figure 5.15 are nine single-walled icosahedral polyhedral fullerenes (SWipF) with diameters between 0.39 nm and 3.69 nm. For the first eight nanoparticles, a good convergence of the Khon-Shams equations was obtained, while for the largest nanoparticle with T=100 and diameter equal to 3.69 nm, a huge computation time was required to reach the energy convergence using tight criteria. All the structures in Figure 5.14 belong to $20N^2$ family [282].

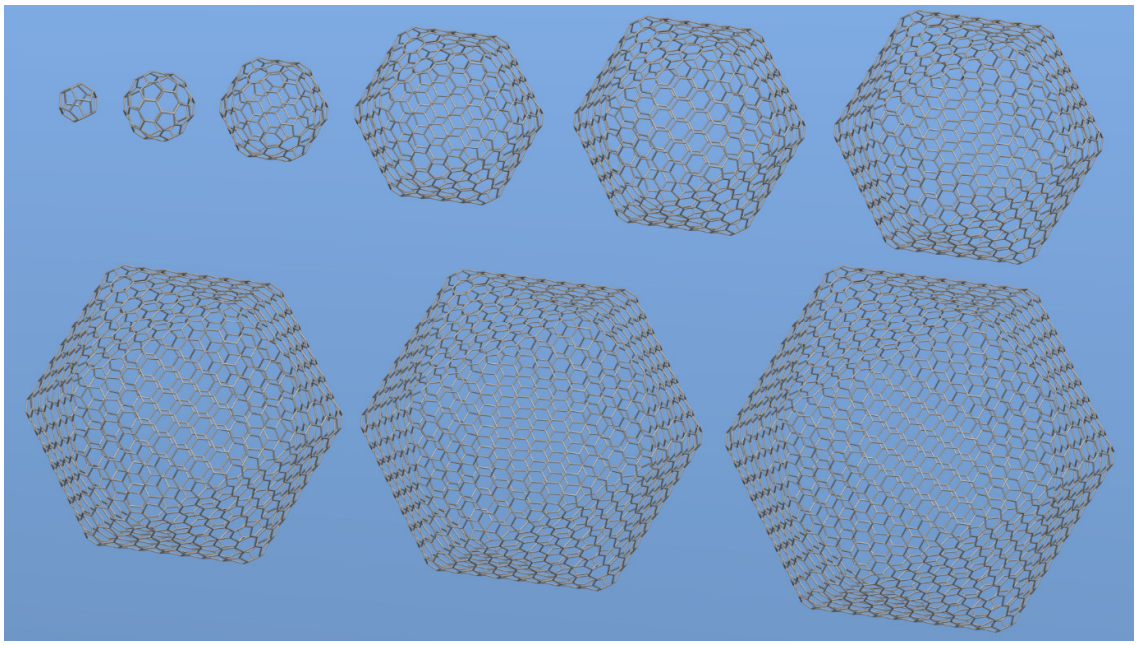

Figure 5.15: Nine single-wall polyhedral nanoparticles obtained by an icosahedron model with diameters ranging from 0.39 nm to 3.69 nm.

In addition, three double-wall icosahedral polyhedral fullerenes (DWiF), with external diameter ranging between 1.13 nm and 2.59 nm, were assembled and shown in Figure 5.16 [282]. The distance between two concentric layers, i.e. distance between two interlayer face, resulted equal to 0.36 nm for all the double wall nanoparticles. This distance is very similar to the interlayer distance of graphene-based structures 0.334nm [268-269].

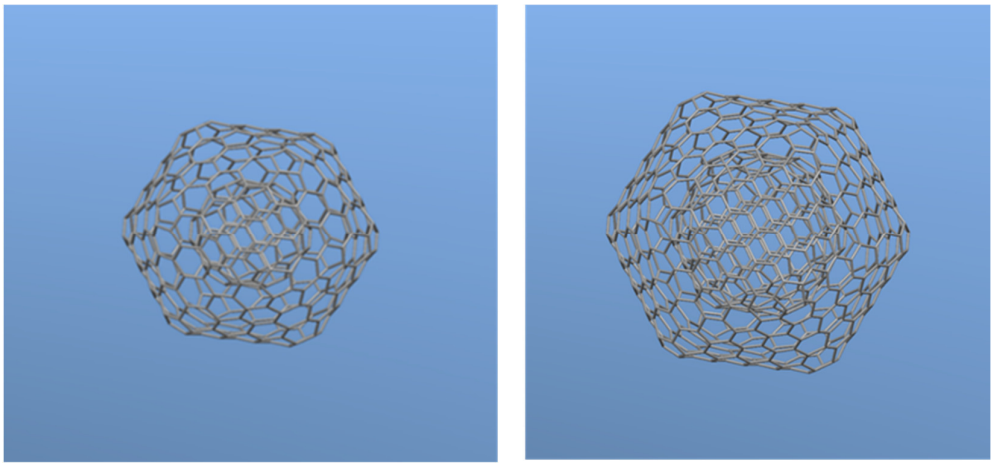

(a) (b)

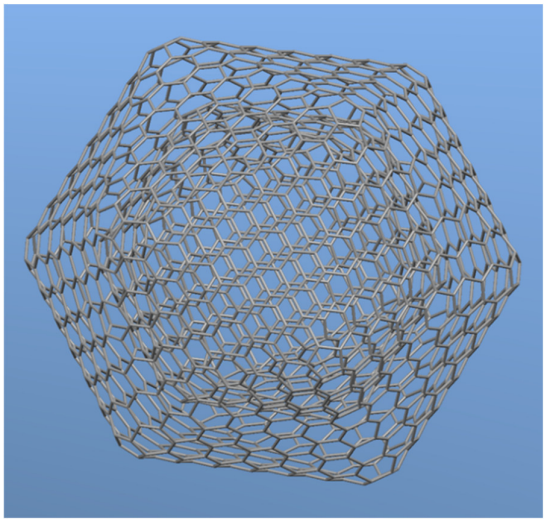

(c)

Figure 5.16: Double wall polyhedral fullerenes obtained by icosahedron model. The Goldberg's triangle vertices of the concentric layers are: (a) T_{inner}= 1, T_{outer}= 9; (b) T_{inner}= 9, T_{outer}= 25; (d) T_{inner}= 25, T_{outer}= 49.

The structures shown in Figure 5.15 and Figure 5.16 were used to calculate the H-L gap, Fermi levels, electron affinity, first ionization potential and the electronegativity as well as the global Hardness and DOS. The Homo and Lumo energies, H-L gap and Fermi levels of the first eight SWipF were listed in Table 5.2, while the same features for three DWipF were showed in Table 5.3. The vertices of the Goldberg's triangles were reported in the first column of these Tables. The particle diameters were evaluated as the distance from the center of an inscribed sphere and the center of the Goldberg triangle on a side of the icosahedron cage. This definition provides a simple way to calculate the distance between successive layers of multi-shell nanostructures. The number of carbons in the icosahedral polyhedral fullerenes studied here are different to those of the multi-walled spherical fullerenes having a similar diameter and reported in Fig. 3, Fig. 4 and Fig. 5 of ref. [237], or in the single-wall (*n, n*) nanoparticle showed in ref. [255].

Table 5.2. Density-functional calculated valence electronic properties and Fermi levels for the studied SWipF.

T	Carbon Atoms	Diameter (nm)	ε_{HOMO} (eV)	ε_{LUMO} (eV)	H-L gap (eV)	Fermi level (eV)
1	ipC_{20}	0.39	-4.179	-2.273	1.91	-3.226
4	ipC_{80}	0.76	-5.150	-2.912	2.24	-4.031
9	ipC_{180}	1.13	-5.703	-4.311	1.39	-5.007
25	ipC_{500}	1.86	-4.861	-3.875	0.99	-4.368
36	ipC_{720}	2.23	-5.243	-4.397	0.85	-4.820
49	ipC_{980}	2.59	-4.724	-4.079	0.65	-4.401
64	ipC_{1280}	2.96	-4.743	-4.118	0.63	-4.430
81	ipC_{1620}	3.33	-5.026)	-4.433	0.59	-4.730

Table 5.3. Density-functional calculated valence electronic properties and Fermi levels for the DWipF.

T_{inner} , T_{outer}	Carbon Atoms	Diameter (nm)	ε_{HOMO} (eV)	ε_{LUMO} (eV)	H-L gap (eV)	Fermi level (eV)
1, 9	$ipC_{20}@C_{180}$	1.13	-4.624	-4.318	0.31	-4.471
9, 25	$ipC_{180}@C_{500}$	1.86	-4.855	-4.407	0.45	-4.631
25, 49	$ipC_{500}@C_{980}$	2.59	-4.794	-4.070	0.72	-4.432

The H-L gaps of single-wall nanoparticles decrease with the increasing of particle's diameters; a maximum value was found for ipC_{80} (T=4). On the contrary, the gaps of the double walled fullerenes show an opposite behavior: The H-L gap increases as the DWipF grows. The Fermi levels of single and double walled nanoparticles as a function of the particles' sizes are not linear: The Fermi levels of the SWipF increase as the particle sizes increase while the DWipF levels oscillate around a constant value. For a clearer comparison between single and double-wall icosahedral polyhedral fullerenes, summarized in Figure 5.17 are their H-P gaps. The SWipF gaps decrease markedly and not linearly as the nanoparticle's sizes increase whereas the opposite trend of the DWipF H-L gaps appears clear. The SWipF gaps with respect to the nanoparticle's diameter (d), without considering ipC_{80}, were interpolated by a decreasing monotone curve [282]:

$$E_{\text{gap}}^{\text{SWipF}} = (-3.97 + 3.24\, d^{-1.14} + 2.20\, d^{-0.15}) \qquad (5.4.1)$$

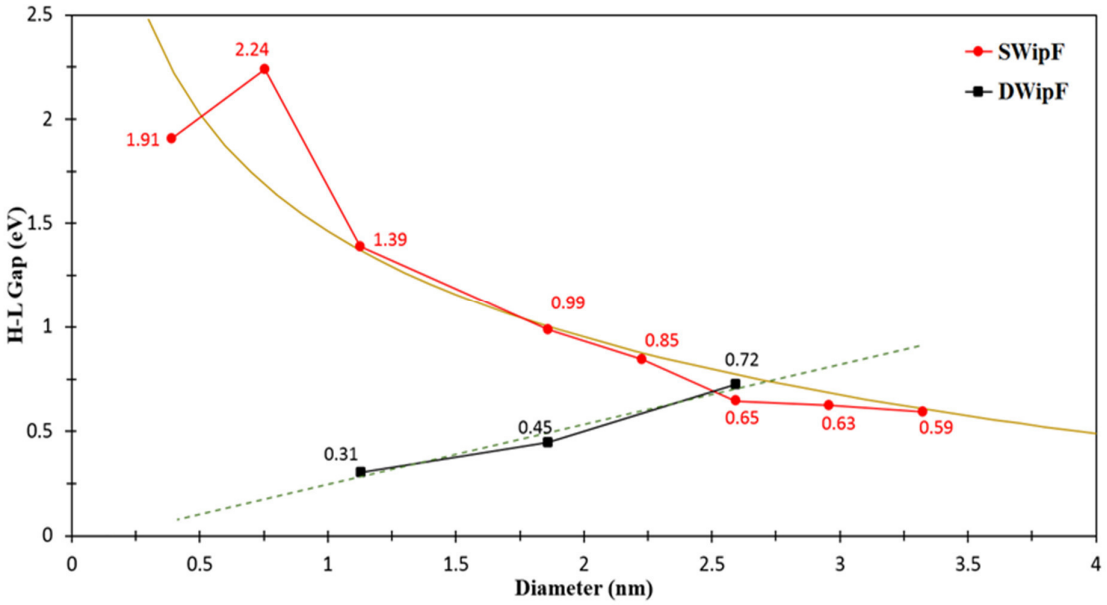

Figure 5.17: H-P gaps of SWipF and DWipF as function of the nanoparticles size.

whereas the gaps of DWipF were fitted by the following linear curve:

$$E_{gap}^{DWipF} = (-0.041 + 0.29\, d) \qquad (5.4.2)$$

The R coefficients associated with the curve (5.4.1) and (5.4.2) are equal to 0.9857 and 0.9836 respectively. Noël *et al.* [258] also reported the H-L gaps of single-wall icosahedral fullerenes as function of their sizes (see Table 2 of Ref. [258]). These gaps were obtained for (*n, n*) single-wall fullerenes using the highly symmetric icosahedral point group at all stages of the quantum calculations (Symmetry Adapted Molecular Orbitals), reducing considerably the dimensions of the matrices to be diagonalized. Noël *et al.* carried out a satisfactory fit of the H-L gaps as function the Goldberg's triangle index, *n*, by a three parameters expressions similar to the above relationship (5.4.1). The n index is directly proportional to the fullerene sizes, thus also for (n, n) single-wall icosahedral fullerenes the H-L gaps decrease not linearly as the nanoparticles mean diameters increase as found for the single-walled fullerenes analyzed herein. Interestingly, in the Noël *et al.* work, the Homo and Lumo energies show always a

degeneracy of 5 and 3, respectively, herein the degeneracy of the Homo and Lumo orbitals was found to equal 4 [282].

Recently, Doore et al. [237] carried out a comparative study on the electronic proprieties of various single and double-walled carbon fullerenes. The studied structures are spherical-like double walled fullerenes and although the outer shells of the double-wall nanoparticles tend to form facets with vertices at the pentagon rings after optimizations, these are different from those investigated here. They reported that the optimized structure of $C_{60}@C_{240}$, with an external diameter equal to 1.38 nm shows semiconducting behavior and a band gap of approximately 0.75 eV. This value is very similar to the gap of the $ipC_{500}@C_{980}$, i.e. 0.72 eV (as shown in Figure 5.17, Table 5.3) having an external diameter equal to 2.59 nm. Interestingly, very similar gaps are displayed by $C_{60}@C_{240}$ and $ipC_{500}@C_{980}$ double-wall nanoparticle with different sizes, thus a larger polyhedral double-wall fullerene shows the same H-L gap of a small double-walled fullerene having a spherical-like shape, or at least with a different shape. Zope R R [275] also reported an energy gap of 0.93 eV for the same small double-walled nanoparticle.

The effect of a second shell on the H-L gap of the SWipF appears clear comparing the values of the red and black curves in Figure 5.17. Following the growth sequence proposed by Mordovic and Takeuchi [232] a second shell is formed on a single-wall embryo, then the repetitive sequence leads in a natural way to giant multi-shell fullerenes. Going from single to double walled polyhedral fullerenes, a drop of the H-L gaps is found up to the $ipC_{180}@C_{500}$ with a diameter of 1.86 nm, whereupon the H-L gap of the double wall nanoparticle ($ipC_{500}@C_{980}$) becomes slightly larger than that of the single-wall fullerene showing same outer diameter. Moreover, Doore et al. concluded that multi-walled carbon fullerenes show semiconducting feature depending on the electronic structure of all underlying fullerene layers: their DFT calculations indicated that carbon onions exhibit non-zero H-L gap only when all constituents of the multi wall fullerenes are non-metallic. Although a systematic reduction of the H-L gap was obtained, the results shown in Figure 5.17 are in agreement with the above Doore's conclusion. The effect of a second wall on the electron affinity (A), first ionization potential (I) and electronegativity was also analyzed; the results were shown in Figure 5.18[282].

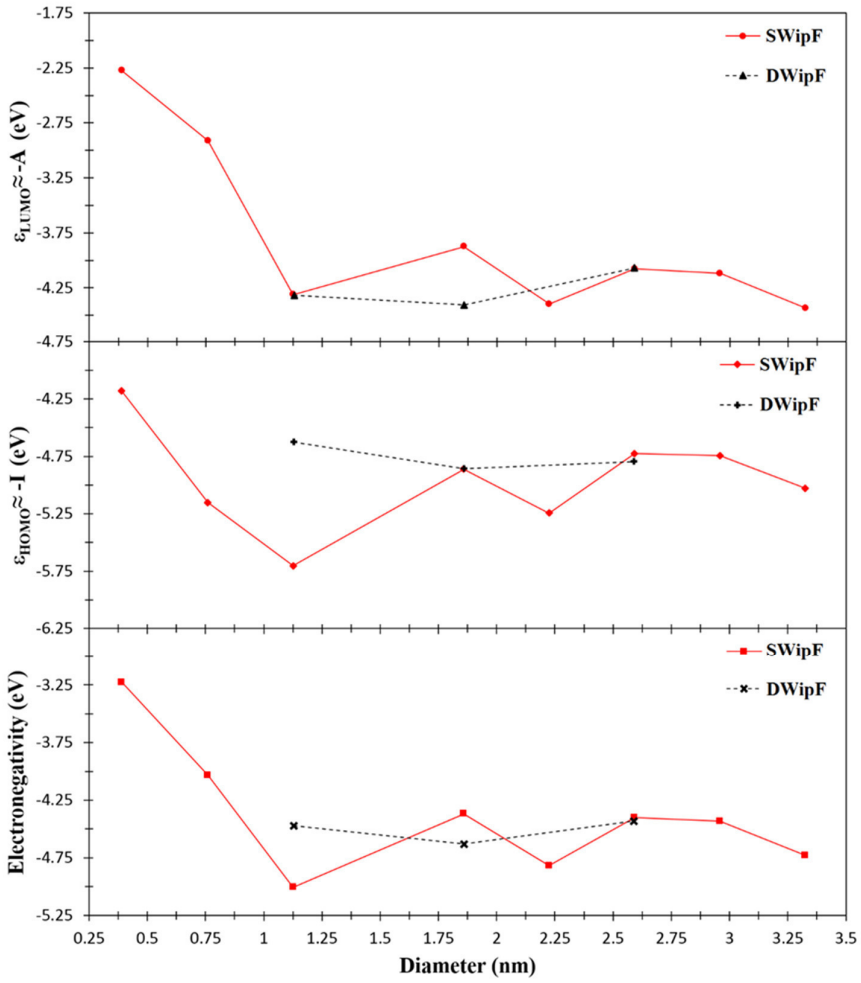

Figure 5.18: Electron affinity, ionization potential and electronegativity of SWipF and DWipF *versus* particle diameters.

Although, Kohn-Sham orbitals are different from the canonical molecular orbitals, using Koopmans's approximation the negative values of *A* and *I* can be approximated with the Kohn-Sham ε_{HOMO} and ε_{LUMO} eigenvalues, [276]. The electronegativity was also evaluated through the three point finite-difference approximation of the $\left(\frac{\partial E}{\partial N}\right)_v$ where N and v are the total number of electrons and the nuclear potential, respectively, of the quantum system with total energy E [277]. As shown in Figure 5.17, the electron affinity, ionization potential and the electronegativity of SWipF decrease up to the fullerene with a diameter of 1.13 nm. Different behaviours have been found after this nanoparticle: electronegativity and *A* are almost constant as a function of the nanoparticle sizes (electronegativity is slightly growing), whereas *I* increase as the sizes of single-wall icosahedral polyhedral fullerenes increases. Comparing the values in the red and black curves it is clear that adding a second wall to the smaller ipC20

nanoparticle, the electron affinity and electronegativity of the corresponding ipC_{20}@C_{180} fall markedly while the ionization potential decreases slightly. On the contrary, going from ipC_{180} to the larger ipC_{180}@C_{500} double wall nanoparticle, the ionization potential and electronegativity increase whereas the electron affinity remain substantially constant. The electronegativity and *I* of the ipC_{500} and corresponding ipC_{500}@C_{980} nanoparticles remain almost constant, whereas again the electron affinity decreases. Finally, it is worth noting that the electron affinity, ionization potential and electronegativity of double-wall nanoparticles with sizes equal to the SWipF are not always equal.

Greyson R. Lewis *et al.* [278] carried out the reoptimization of previously determined icosahedral single-wall fullerenes by Zope et. al. [279] in the framework of DFT. In particular, they optimized the structures of six icosahedral fullerenes of the $60N^2$ family and the C_{320}, in addition to two structures belonging to the family of $180N^2$ (C_{180} and C_{720}). The differences between the cations energies, $E_n(N-1)$ and those of the optimized neutral geometries, E (N), were achieved to evaluate the first ionization potential, while for the electron affinity the difference between the anions energy, $E_n(N+1)$ and E (N) were performed. The values obtained by R. Lewis *et al.* were 6.92 eV and 3.45 eV for the ionization potential and electron affinity of its C_{180}, respectively, while 5.93 eV and 4.03 eV for *I* and *A* of the C_{720}. Comparing I_{180} and A_{180} with the values for single-walled fullerenes with the same atoms number, evaluated in this paper, results that the difference between the ionization potentials is 1.2 eV while between the electron affinities is -0.8 eV. Comparing the I_{720} and A_{720} values with the corresponding values, shown in Figure 5.19, results that the difference between the ionization potentials is 0.7 eV while between the electron affinities is -0.3 eV. The diameters of the investigated single-wall nanoparticles are 1.13 nm and 2.23 for ipC_{180} and ipC_{720}, respectively, while the diameters of the fullerenes analyzed in the Greyson's work are 1.22 nm and 2.42 nm respectively, i.e. very similar. The difference between the *I* and *A* values may be due to the approximation adopted here i.e. ε_{HOMO} =- I and ε_{LUMO}= -A, but also to the fact that the fullerenes the initial structures used in the optimizations are different, as reported in the original work Zope et. [275]- [279], from those studied herein (i.e. isomers) although these structures have the same number of carbons and icosahedral symmetry.

The global hardness was defined as the second derivative of total energy of the system with respect to the number of electrons, i.e. $\eta = \frac{1}{2}\left(\frac{\partial^2 E}{\partial N^2}\right)_v$, while the softness was calculated as

the inverse of the hardness, $S = \frac{1}{2\eta}$. For calculating the global hardness as function of the KS eigenvalues, various relationships can be find in literature, [281]. Herein, the general equation $\eta = \frac{I-A}{2}$ was adopted [277]-[280], which can be considered as the average value between ionization potential and electro affinity. As result, the numerator of this relationship is equal to the H-L gap, nevertheless, these proprieties were plotted in Figure 5.18, to clearly highlight the differences among the softness going from single to double-walled icosahedral polyhedral fullerenes as function of the nanoparticles sizes. In fact, comparing the values of the red and black lines in this Fig., the effect of a second larger shell on the hardness and softness of the SWipF can be easily analyzed. Adding a second wall, the softness of the SWipF increases markedly, albeit this enhancement depends again by their sizes. From a physical point of view, this means that a second shell makes the double walled nanoparticle more softness (i.e. more polarizable) with respect to the corresponding single-wall nanoparticles. Instead, if the softness is analyzed as function of nanoparticles sizes, the Figure 5.19 shows that the double-wall ipC$_{500}$@C$_{980}$ fullerene is less soft than ipC$_{980}$ single-wall nanoparticles having the same external diameter [282].

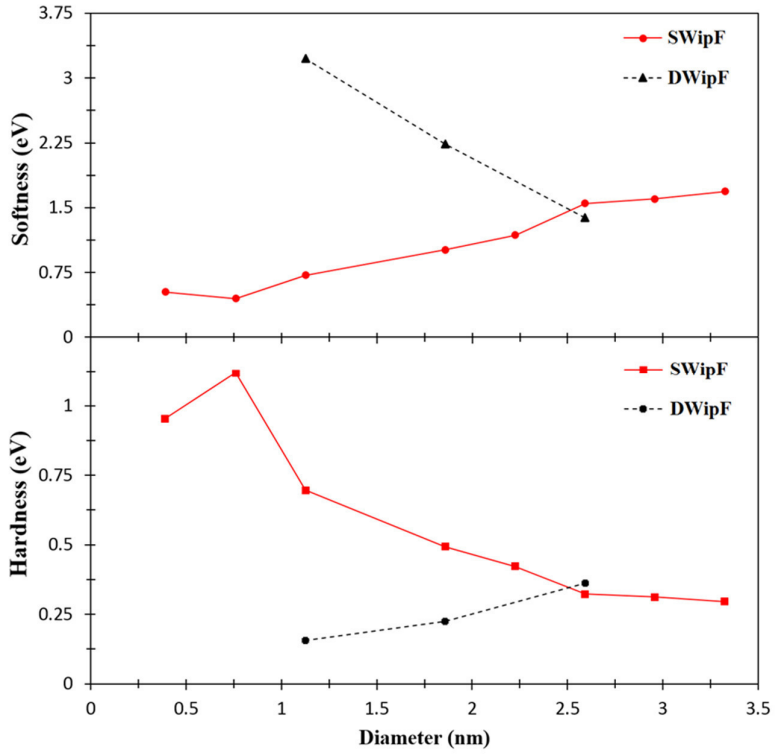

Figure 5.19: Global hardness and softness as function of the SWNPs and DWNPs sizes.

The DOS of the single and double wall nanoparticles were compared in the last Figure 5.20, It is important to anticipate that linear combinations of Gaussian-type orbitals and non-periodic calculations were performed in this case thus the calculated molecular orbitals do not show band structures. DOS were obtained by computing the number of the molecular orbitals falling in a small range equal to 0.001 a. u (0.03 eV) and considering a window around the Fermi level was -6 eV; +6 eV of each nanoparticles.

a)

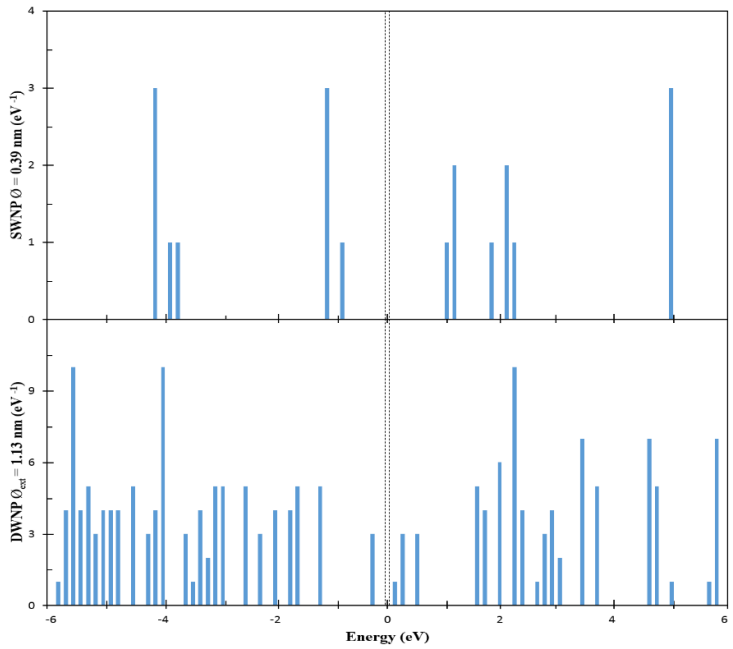

b)

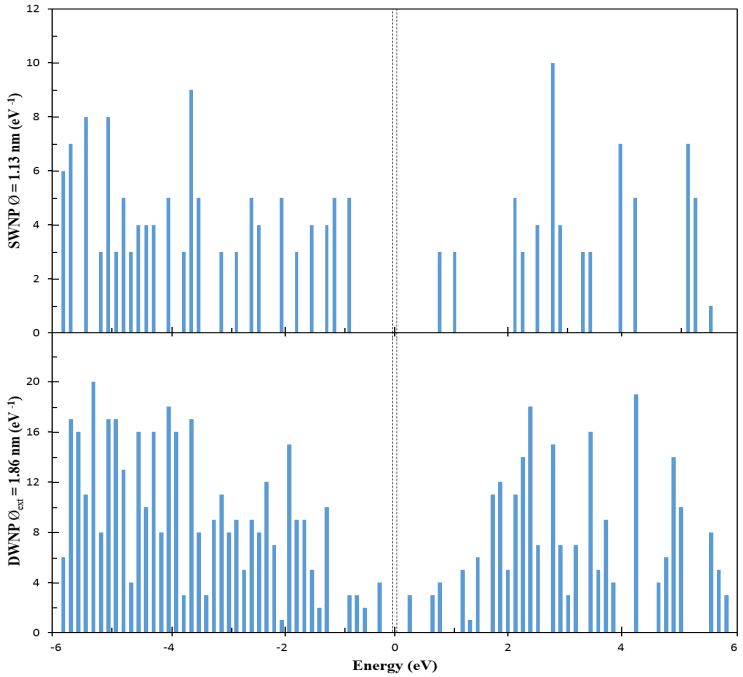

c)

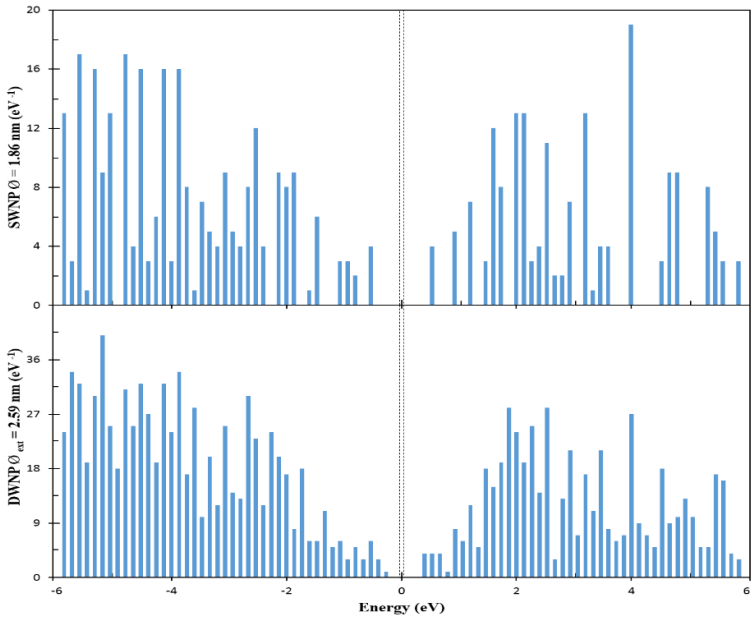

Figure 5.20: Calculated DOS of single and double wall icosahedral polyhedral fullerenes: a) ipC_{20} and $ipC_{20}@C_{180}$ (T_{inner} =1 T_{outer} =9); b) ipC_{180} and $ipC_{180}@C_{500}$ (T_{inner} =9 T_{outer} =25); c) ipC_{500} and $ipC_{500}@C_{980}$ (T_{inner} =25 T_{outer} =49).

The calculated DOS highlight that both single and double-walled fullerenes should show semiconductor features unlike the double-walled fullerenes. A second shell modifies the DOS of the corresponding single-wall nanoparticle; the modification depends again on the nanoparticle sizes; it is marked for single and double wall fullerenes with small sizes. For ipC_{20} and $ipC_{20}@C_{180}$ discrete peaks (molecular-like states) were obtained, as expected, instead, continuous peaks are found increasing the size of the single and double wall fullerenes. DOS of the $pC_{180}@C_{500}$ and $pC_{500}@C_{980}$ show less molecular-like states and more band structures, although the molecular-like states for single-walled structures still persist. This implies that the number of the molecular orbitals per energy unit near to the Fermi level increases when a second shell is added to a smaller corresponding nanoparticle while the H-P gap decreases. As pointed out, the semiconductor feature depending on the electronic structure of the underlying fullerene layers, even if a decreasing of H-L gaps occurs going from the SWipF to DWip, however, the DOS of the studied double walled nanoparticles show a denser electronic structures. In addition, the peaks distribution changes around Fermi level: the double wall fullerenes show less symmetrical distributions than the single-wall nanoparticles. Noël *et al* [258] plotted the degeneracy of the K-S eigenvalues with respect to the energy for (*n, n*) single-wall fullerenes, besides the graphene density of the states as reference. Noël also found that by

increasing the size of the single-wall fullerenes a denser orbital structure and peaks distribution not symmetrical was got as highlighted in this work [242].

5.5 Conclusions

Significant amount of works are devoted to the calculations of the electronic properties of multi shell fullerenes, however, calculations on multi-walled icosahedral polyhedral fullerenes are not many. In this work, some key electronic proprieties of single and double-walled carbon fullerenes with different sizes were calculated in the frame of the DFT and compared. Structures of icosahedral polyhedral fullerenes, previously validated by Scheina and Gayed were used to get the H-L gaps, electron affinity, ionization potential, electronegativity as well as the Density of the electronic States.

The effect of a second wall on the features of corresponding single-wall nanoparticles was investigated. This study shows that the H-L gaps of single-wall fullerenes decrease as the particles sizes increase, whereas an opposite trend was found for the double-wall nanostructures. Moreover, going from single to double wall nanoparticles a systematic and marked decrease of the H-L gap was found up to the $ipC_{180}@C_{500}$ double-wall fullerene then an inversion was obtained. The trend of softness (correlated to system polarizability) versus nanoparticle sizes and number of shell is physically consistent.

The DOS analysis reveals that the semiconductor character of the double-walled nanoparticles is conserved, unlike analogues of DW fullerenes with different shapes. The DOS structures of SW nanoparticles changes radically adding a second shell, and the extent of these changes depends on the sizes of the investigated fullerenes, although this conclusion should be confirmed by quantum periodic calculations with plane wave functions.

References

[1] M. A. Bhat, A. Nanda (2014) Nanotechnology, Metal Nanoparticles, and Biomedical Applications of Nanotechnology. 116-155. 10.4018/978-1-4666-6304-6.ch005

[2] G. M. Whitesides, B. Grzybowsky (2002) Self-Assembly at all Scales. *Science* **295**, 2418-2421

[3] Y. Yin, D. Talapin (2013) The Chemical of Functional Nanomaterials. *Chem. Soc. Rev.* **42**, 2484-2487

[4] M. Sasidharan, K. Nakashima (2014) Core Shell Corona Polymeric Micelles as a Versatile Template for Synthesis of Inorganic Hollow Nanospheres. *Acc. Chem. Res.* **47**, 157-167

[5] T. Kusukawa, M. A. Fujita (2002) Self-Assembled M6L4-type Coordination Nanocage with 2,2'-Bipyridine Ancillary Ligands Facile Chrystalization and X-ray of Shape-Selective Enclathartion of Newtral guests in the cage. *J. Am. Chem. Soc.* **124**, 13576-13582.

[6] J. D. Hartherink, E. Beniash, S. I. Strupp (2001) Self-Assembly and Mineralization of Peptide-amphiphile Nanofibers. *Science* **294**, 1684-1688

[7] J. P. Hill, W. Jin, A, Kosaka, T. Fukushima, H. Ichiahara, T. Shimomura, K. Ito, T. Hashizume, N. Ishii, T. Aida (2007) Self-Asembled Hexa-peri-exabenzocoronene Graphitic Nanotube. *Science* **304**, 1481-1483

[8] S. Biswas, K. Kimbara, N. Oya, N. Ishii, H. Taguchi, T. Aida (2009). A Tubular Bicontainer: Metal Ion-Induced 1D Assembly of a Molecularly Engineered Chaperonin. *J. Am. Chem. Soc.* **131**, 7556-7557

[9] S. Iijima (1991) Helical microtubules of graphitic carbon. *Nature* **354**, 56-58

[10] S. Iijima (1993) Growth of carbon nanotubes. *Materials Science and Engineering: B* **19**,172-180

[11] D. Ugarte (1992) Curling and closure of graphitic networks under electron-beam irradiation. *Nature* **359**, 707-709

[12] K. Ariga, M. Li, G. Richards, J. Hill (2011) Nanoarchitectonics: A conceptual Paradigm for Design and Synthesis of Dimension-Controlled Functional Nanomaterials. *J. Nanoci. Nanotechnol.* **11**, 1-13

[13] C.K. Gosh (2015) Quantum effect on properties of nanomaterials. In. Sengupta A., Sarkar C. (eds) Introduction to Nano. Engeneering Materials. Springer. Berlin. Heidelberg.

[14] V.V. Pokropivny, V.V. Skorokhod (2007) Classification of nanostruc-tures by dimensionality and concept of surface forms engineering in nanomaterial science, *Materials Science and Engineering* C 27, 990993

[15] N. Taniguchi (1974) On the basic concept of 'nano-technology'. *Proc. Intl. Conf.*

Prod. Eng., Part II, Japan Society of Precision Engineering.

[16] V. Pokropivny, R. Lohmus, I. Hussainova, A. Pokropivny, S. Blasov (2007). Introduction to nanomaterials and nanotechnology. University of Tartu, 225p.

[17] H. Hahn, (2005) Unique Features and Properties of Nanostructured Materials, in Nanomaterials by Severe Plastic Deformation (eds M. Ze-hetbauer and R. Z. Valiev), Wiley-VCH Verlag GmbH & Co. KGaA, Weinheim, FRG. doi: 10.1002/3527602461.ch1a

[18] J. Kowtecky, M. Tomasek (1960) Study of Surface States of Diamond and Graphite by a Simple MO-LCAO Method. *Phys. Rev.* **120**, 1212-1218

[19] C. E. Nebel, J. Müns, M. Stutzmann (1997) Electronic properties of CVD syntetic diamond. *Phys. Rev. B* **55**, 9765-9791

[20] L. Lang, S. Doyeng-Lang, A. Charlier, M. F. Charlier (1994) Dynamic study of graphite and graphite intercalation compounds. *Phys. Rev. B* **49**, 5672-5681

[21] F. P. Bundy (1989) Pressure-temperature phase diagram of elemental carbon. *Physica A* **156**, 169-178

[22] D. Saada, J. Adler, R. Kalish (1999) Computer simulation of damage in diamond due to ion impact and its annealing. *Phys. Rev. B* **59**(10), 6650-6660

[23] H. W. Kroto, J. R. Heath, S. C. O´Brien, R. F. Curl, R. E. Smalley (1985) C60: Buckminsterfullerene. *Nature* **318**, 162-163

[24] W. D. Callister (2007) Materials Science and Engineering: An Introduction (ed. Joseph Hayton), John Willey & Sons, Inc. ISBN-13:968-0-471-73696-7 (clotch)

[25] F. Li, D. Ramage, J. S. Lannin, J. Conseicao (1991) Radial distribution function of C_{60}: Structure fullerene. *Phys. Rev. B* **44**, 13167-13170

[26] S. Iijima (1991) Helical microtubules of graphitic carbon. *Nature 354*, 56-58

[27] M. S. Hybertsen, S. G. Louie (1985) Proceedings of the I7th International Conference on the Physics of Semiconductors, edited by D. J. Chadi and W. A. Harrison (Springer-Verlag, New York, 1985), p. 1001; *Phys. Rev. Lett.* **55**, 1418 {1985); *Phys. Rev. B* **34**, 5390 (1986)

[28] M. P. Surh, S. G. Louie, M. L. Cohen (1992) Band gaps of diamond under anisotropic stress. *Phys. Rev. B* **45**, 8239-8247

[29] W. Bragg (1928), An Introduction to Crystal Analysis (Bell, London), p. 64

[30] C. M. Mate, G. M. McClelland, R. Erlandsson, S. Chiang (1987) Atomic-scale friction of a tungsten on a graphite surface, *Phys. Rev. Lett.* **59**, 1942

[31] H. Holscher, W. Allers, U. D. Schwarz, A. Schwarz, R. Wiesendanger (1997) Interpretation of "true atomic resolution" images of graphite (0001) in noncontact atomic force microscopy. *Phys. Rev. B* **56**, 6987

[32] H. Holscher, U. D. Schwarz, O. Zwörner, A. Schwarz, R. Wiesendanger (1998) Consequences of thick-slip movement for the scanning force microscopy imagine of graphite *Phys. Rev. B* **57**, 2477-2481

[33] "See: 'http://www.iop.org/publications/iop/2011/page_48026.html' for a short introduction of graphene," *IOP Institute of Physics*, 2011

[34] A. H. Castro Neto, F. Guinea, N. M. R. Peres (2006) Drawing conclusions from graphene. *Physics World* **19**, 33-37

[35] M. I. Katsnelson, K. S. Novoselov, A. K. Geim (2006) Chiral tunneling and the Klein Paradox in graphene. *Nat. Phys.* **2**, 620-625

[36] M. I. Katsnelson, K. S. Novoselov (2007). Graphene: new bridge between condensed matter physics and quantum electrodynamics. *Solid State Commun* **143**, 3-31

[37] A. K. Geim, K. S. Novoselov (2007) The rise of graphene. *Nat. Mater.* **6**, 183–91

[38] A. H. Castro Neto, F. Guinea, N. M. R. Peres, K. S. Novoselov, A. K. Geim (2009) The electronic properties of graphene. *Rev. Mod. Phys.* **81**, 109–162

[39] A K. Geim (2009) Graphene: Status and Prospects. *Science* **324**, 1530–1534

[40] X. Li, W. Cai, J. An, R, Ruoff (2009) Large area synthesis of high quality and uniform graphene films on copper foils. *Science* **324**, 1312–1314

[41] S. Bae *et al.* (2010) Roll-to-roll production of 30-inch graphene films for transparent electrodes. *Nat. Nanotechnol.* **5**, 574-578

[42] J. Bai, R. Cheng, F. Xiu, L. Liao, M. Huang, A. Shailos, K. L. Huang, Y. Huang, X. Duand (2010) Very large magnetoresistance in graphene nanoribbons. *Nat. Nanotechnol.* **5**, 655-659

[43] J. Cai *et al.* (2010) Atomically precise bottom-up fabrication of graphene nanoribbons. *Nature* **466**,470-473

[44] X. Wang *et al.* (2009) N-doping of graphene through electrothermal reactions with ammonia. *Science* **324**,768-771

[45] S. Dutta, S. K. Pati (2008) Half-metallicity in undoped and boron doped graphene nanoribbons in the presence of semilocal exchange-correlation interactions. *J. Phys. Chem. B* **112**, 1333-1335

[46] P. Recher, B. Trauzettel (2011) A defect controls transport in graphene. *Physics* **4**, 25

[47] Y. Mao, J. Yuan, J. Zhong (2010) Density functional calculation of transition metal adatom adsorption on graphene. *Phys. B Condens. Matter* **405**, 3337-3341

[48] P. A. Khomyakov, G. Giovannetti, P. C. Rusu, G. Brocks, J. Van Den Brink, P. J. Kelly (2009) First-principles study of the interaction and charge transfer between graphene and metals. *Phys. Rev. B - Condens. Matter Mater. Phys.* **79**, 1-12

[49] E. Rotenberg, A. Bostwick, T. Ohta, J. L. McChesney, T. Seyller, K. Horn (2008) Origin of the energy bandgap in epitaxial graphene. *Nat. Mater.* **7**, 258-259-260

[50] S. Y. Zhou *et al.* (2008) Origin of the energy bandgap in epitaxial graphene. *Nat. Mater.* **7**,258-260

[51] G. Giovannetti, P. A. Khomyakov, G. Brocks, P. J. Kelly, J. Van Den Brink (2007) Substrate-induced band gap in graphene on hexagonal boron nitride: Ab initio density functional calculations. *Phys. Rev. B - Condens. Matter Mater. Phys.* **76**, 2-5

[52] A. M. Shikin, G. V. Prudnikova, V. K. Adamchuk, F. Moresco, K. H. Rieder (2000) Surface intercalation of gold underneath a graphite monolayer on Ni(111) studied by angle-resolved photoemission and high-resolution electron-energy-loss spectroscopy. *Phys. Rev. B - Condens. Matter Mater. Phys.* **62**, 13202-13208

[53] Y. Dedkov *et al.* (2001) Intercalation of copper underneath a monolayer of graphite on Ni(111). *Phys. Rev. B* **64**, 1-6

[54] Y. S. Dedkov, M. Fonin, U. Rüdiger, C. Laubschat (2008) Graphene-protected iron layer on Ni(111). *Appl. Phys. Lett.* **93**, 0-3

[55] I. Gierz, C. Riedl, U. Starke, C. R. Ast, K. Kern (2008) Atomic hole doping of graphene. *Nano Lett.* **8**, 4603-4607

[56] C. Enderlein, Y. S. Kim, A. Bostwick, E. Rotenberg, K. Horn (2010) The formation of an energy gap in graphene on ruthenium by controlling the interface. *New J. Phys.* **12**, 111

[57] I. Gierz *et al.* (2010) Electronic decoupling of an epitaxial graphene monolayer by gold intercalation. *Phys. Rev. B - Condens. Matter Mater. Phys.* **81**, 1-6

[58] K. T. Chan, J. B. Neaton, M. L. Cohen (2008) First-principles study of metal adatom adsorption on graphene. *Phys. Rev. B - Condens. Matter Mater. Phys.* **77**, 1-12

[59] D. W. Boukhvalov, M. I. Katsnelson (2009) Chemical functionalization of graphene. *Molecules* **21**, 344205

[60] C. Coletti *et al.* (2010) Charge neutrality and band-gap tuning of epitaxial graphene on SiC by molecular doping. *Phys. Rev. B - Condens. Matter Mater. Phys.* **81**, 1-8

[61] E. J. H. Lee, K. Balasubramanian, R. T. Weitz, M. Burghard, K. Kern (2008) Contact and edge effects in graphene devices. *Nat. Nanotechnol.* **3**, 486-490

[62] E. N. Voloshina, Y. Dedcov (2011) Electronic and Magnetic Properties of the Graphene-Ferromagnet Interfaces: Theory vs Experiment. Research Gate DOI: 10.5772/14922 · Source: InTech

[63] T. Mueller, F. Xia, M. Freitag, J. Tsang, P. Avouris (2009) Role of contacts in graphene transistors: A scanning photocurrent study. *Phys. Rev. B - Condens. Matter Mater. Phys.* **79**, 1-6

[64] B. Huard, N. Stander, J. A. Sulpizio, D. Goldhaber-Gordon (2008) Evidence of the role of contacts on the observed electron-hole asymmetry in graphene. *Phys. Rev. B - Condens. Matter Mater. Phys.* **78**, 121402

[65] A. H. C. Neto (2010) The carbon new age. *Mater. Today* **13**, 12-17

[66] B. Xu (2008) Prospects and Research Progress in Nano Onion-Like Fullerenes. *New Carbon Materials* **23**, 289-301

[67] L. Echegoyen, A. L. Ortiz, M. N. Chaur, A. J. Palkar (2010) Carbon Nano Onions. In Chemistry of Nanocarbons. T. Akasaka, F. Wudl, S. Nagase (eds). John Willey & Sons. Chichester, U. K.

[68] J. Bartellmes, S. Giordani (2014) Carbon Nano-Onions (Multi-layer Fullerenes): Chemistry and Applications. *Belstein J. Nanotechnol.* **5**, 1980-1998

[69] I. Suarez-Marinez, N. Grobert, C. P. Ewels (2012) Nomenclature of sp2 carbon nanoforrms. *Carbon* **50**, 741-747

[70] S. Iijima (1980) Direct observation of tetrahedral bonding in graphitized carbon black by high resolution electron microscopy. *J. Cryst. Growt* **50**, 675-683

[71] S. Iijima (1987) The 60-carbon cluster has been revealed. *J. Phys. Chem*. **91**, 3466-3467

[72] D. Ugarte (1992) How to fill or empty a graphitic onion. *Chem. Phys. Lett.* **198**, 99-103

[73] M. Zeiger, N. Jäckel, V. N. Mochalin, V. Presser (2016) Review: carbon onions for electrochemical energy storage. *J. Mater. Chem. A* **4**, 3172-3196

[74] A. Bianco *et al.* (2013) All in the graphene family a recommended nomenclature for two-dimensional carbon materials. *Carbon* **65**, 1-6

[75] O. A. Shenderova, D. M. Gruen (2012) Ultrananocrystaline diamond: synthesis, properties and applications. William Andrew.

[76] M. S. Dresselhaus, G. Dresselhaus, P. C. Eklund (1995) Science of fullerenes and Carbon Nanotubes (Academic Press, California)

[77] D. Pech, *et al.* (2010) Ultrahigh-power micrometer-sized supercapacitors based on onion like-carbon. *Nat. Nanotechnol.* **5**, 651-654

[78] C. Portet, G. Yushin, Y. Gogotsi (2007) Electrochemical performance of carbon onions, nanodiamonds carbon black and multiwalled nanotubesin electrical double layer capacitors. *Carbon* **45**, 2515

[79] R. Bacon (1960) Grow structure and properties of graphite whiskers. *J. Appl. Phys.* **31**, 283-290

[80] D. Tomanek (1995) World with Buckyballs. *J. Korean Phys. Soc.* **28**, S609

[81] D. Ugarte (1995) Onion like-graphitic particles. *Carbon* **33**, 989-993

[82] C.J. Brabec, A. Maiti, J. Bernholc (1994) Structural defects and the shape of large fullerenes. *Chem. Phys. Lett.* **219**, 473-478

[83] M. José-Yacamán, H. Terrones, L. Rendón, J.M. Domínguez (1995) Carbon structures grown from decomposition of a phenylacetylene and thiophene mixture on Ni nanoparticles. *Carbon* **33**, 669–678

[84] K.D. Sattler (Ed.) (2016) Carbon nanomaterials sourcebook. Graphene, fullerenes, nanotubes, and nanodiamonds, Taylor & Francis Group, Boca Raton.

[85] H. Terrones, M. Terrones (1997) The transformation of polyhedral particles into graphitic onions. *J. Phys. Chem. Solids* **58**, 1789-1796

[86] F. Tuinstra, J. L. Koening (1970) Raman Spectrum of Graphite. *J. Chem. Phys.* **53**, 1126

[87] S. A. Solin, A. K. Ramdas (1970) Raman Spectrum of diamond. *Phys. Rev. B* **1**, 1687-1698

[88] A. M. Rao, *et al.* (1997) Diameter-Selective Raman Scattering from Vibrational Modes in Carbon Nanotubes. *Science* **275**, 187-191

[89] E. D. Obraztsova, *et al.* (1998) Raman identification of onion-like carbon. Carbon 36, 821-826

[90] L. Lespade, R. Al-Jishi, M. S. Dresselhaus (1982) Model for Raman scattering from incomplety graphitized carbons. Carbon 20, 427-431

[91] S. Tomita, T. Sakurai, H. Ohta, M. Fujii, S. Hayashi (2001) Structure and electronic properties of carbon onions. *J. Chem. Phys.* **114**, 7477-7482

[92] D. Roy, *et al.* (2003) Characterization of carbon nano-onions using Raman spectroscopy. *J. Chem. Phys. Lett.* **373**, 52-56

[93] S. Krishnamurthy, et al. (2013) In situ formation of onion-like carbon from the evaporation of ultra-dispersed nanodiamonds. *Carbon* **52**, 145-149

[94] O. Mykhailiv, H. Zubyk, M. E. Plonska-Brzezinska (2017) Carbon nano-onions: Unique carbon nanostructures with fascinating properties and their potential applications. *Elsevier* 0020-1693

[95] A. C. Tang, F. Q. Huang (1995) Electronic structures of giant fullerenes with I_h symmetry. *Phys. Rev. B* **51**, 13830-13832

[96] A. C. Tang, F. Q. Huang (1995) Theoretical study of multi-shell fullerenes. *Phys. Rev. B* **52**, 17435-17438.

[97] Y. –L. Lin, F. Nori (1994) Electronic structure of single- and multiple-shell carbon fullerenes. *Phys. Rev. B* **49**, 5020-5023

[98] C. He, N. Zhao, C. Shi, X. Du, J. Li (2006) Carbon nanotubes and onions from methane decomposition using Ni/Al catalysts. *Mater. Chem. Phys*. **97**, 109-115.

[99] S.-S. Hou, D.-H. Chung, T.-H. Lin (2009) High-yield synthesis of carbon nano-onions in counterfow diffusion flames. *Carbon* **47**, 938-947.

[100] M. Choucair, J. A. Stride (2012) The gram-scale synthesis of carbon onions. *Carbon*, **50**, 1109-1115

[101] Y. Gao*, et al*. (2011) Resonant excitation of precursor molecules in improving the particle crystallinity, growth rate and optical limiting performance of carbon nano-onions. *Nanotechnology* **22**, 165604

[102] M. Zhao, H. Song, X. Chen, W. Lian (2007) Large-scale synthesis of onion-like carbon nanoparticles by carbonization of phenolic resin. *Acta Mater.* **55**, 6144-6150

[103] M. Bystrzejewski, M. H. Rummeli, T. Gemming, H. Lang, A. Huczko (2010) Catalyst-free synthesis of onion-like carbon nanoparticles. *New Carbon Mater.* **25**, 1-8

[104] D.-H. Chung, T.-H. Lin, S.-S. Hou (2010) Flame synthesis of carbon nano-onions enhanced by acoustic modulation. *Nanotechnology* **21**, 435604

[105] M. Choi, *et al*. (2004) Formation of Shell-Shaped Carbon Nanoparticles Above a Critical Laser Power in Irradiated Acetylene. *Adv. Mater.* **16**, 1721-1725

[106] J. Huang, H. Yasuda, H. Mori (1999) Highly curved carbon nanostructures produced by ball-milling. *Chem. Phys. Lett.* **303**, 130-134

[107] X. H. Chen, *et al*. (2000) Generation of curved or closed-shell carbon nanostructures by ball-milling of graphite. *J. Cryst. Growth*. **218**, 57-61

[108] T. Cabioc'h, M. Jaouen, E. Thune, P. Guerin, C. Fayoux, M. Denanot (2000) Carbon onions formation by high-dose carbon ion implantation into copper and silver. *Surf. Coat. Technol.* **128**, 43-50

[109] E. Thune, T. Cabioc'h, P. Guerin, M.-F. Denanot, M. Jaouen (2001) Nucleation and growth of carbon onions synthesized by ion-implantation: a transmission electron microscopy study. *Mater. Lett.* **54**, 222-228

[110] H. Lange, M. Sioda, A. Huczko, Y. Zhu, H. Kroto, D. Walton (2003) Nanocarbon production by arc discharge in water. *Carbon* **41**, 1617-1623

[111] M. Ishigami, J. Cumings, A. Zettl, S. Chen (2000) A simple method for the continuous production of carbon nanotubes. *Chem. Phys. Lett.* **319**, 457-459

[112] N. Sano, H. Wang, M. Chhowalla, I. Alexandrou, G. Amaratunga (2001) Nanotechnology: synthesis of carbon 'onions' in water. *Nature* **414**, 506-507

[113] W. Lian, *et al*. (2008) The transformation of acetylene black into onion-like hollow carbon nanoparticles at 1000 °C using an iron catalyst. *Carbon* **46**, 525-530

[114] J.-C. Fan, H.-H. Sung, C.-R. Lin, M.-H. Lai (2012) The production of onion-like carbon nanoparticles by heating carbon in a liquid alcohol. *J. Mater. Chem.* **22**, 9794

[115] S. Tomita, A. Burian, J. C. Dore, D. LeBolloch, M. Fujii, S. Hayashi (2002) Diamond nanoparticles to carbon onions transformation: X-ray diffraction studies, *Carbon* **40**, 1469-1474

[116] Y. V. Butenko, *et al*. (2000) Kinetics of the graphitization of dispersed diamonds at "low" temperatures. *J. Appl. Phys*. **88**, 4380

[117] S. Tomita, T. Sakurai, H. Ohta, M. Fujii, S. Hayashi (2001) Structure and electronic properties of carbon onions. *J. Chem. Phys*. **114**, 7477

[118] Y. V. Butenko, *et al*. (2006) The Thermal Stability of Nanodiamond Surface Groups and Onset of Nanodiamond Graphitization, Fullerenes, Nanotubes. *Carbon Nanostruct.* **14**, 557-564

[119] Q. Zou, Y. G. Li, B. Lv, M. Z. Wang, L. H. Zou, Y. C. Zhao (2010) Transformation of onion-like carbon from nanodiamond by annealing. *Inorg. Mater.* **46**, 127-131

[120] V. L. Kuznetsov, A. L. Chuvilin, Y. V. Butenko, I. Y. Mal'kov, V. M. Titov (1994) Onion-like carbon from ultra-disperse diamond. *Chem. Phys. Lett*. **222**, 343-348

[121] M. Zeiger, N. Jäckel, M. Aslan, D. Weingarth, V. Presser (2015) Understanding structure and porosity of nanodiamond derived carbon onions. *Carbon* **84**, 584-598

[122] N. Xu, J. Chen, S. Deng (2002) Effect of heat treatment on the properties of nano-diamond under oxygen and argon ambient. *Diamond Relat. Mater*. **11**, 249-256

[123] A. Aleksenskii, M. Baidakova, A. Y. Vul, V. Y. Davydov, Y. A. Pevtsova (1997) Diamond–graphite phase transition in ultradisperse-diamond clusters. *Phys. Solid State* **9**, 1007-1015

[124] J. Chen, S. Deng, J. Chen, Z. Yu, N. Xu (1999) Graphitization of nanodiamond powder annealed in argon ambient. *Appl. Phys. Lett*. **74**, 3651-3653

[125] F. Y. Xie, *et al*. (2010) Surface characterization on graphitization of nanodiamond powder annealed in nitrogen ambient. *Surf. Interface Anal*. **42**, 1514-1518

[126] A. Aleksenskii, M. Baidakova, A. Y. Vul, A. Dideikin, V. Siklitskii (2000) Effect of hydrogen on the structure of ultradisperse diamond. *Phys. Solid State* **42**, 1575-1578

[127] M. E. Plonska-Brzezinska, D. M. Brus, A. Molina-Ontoria, L. Echegoyen (2013), Synthesis of carbon nano-onion and nickel hydroxide/oxide composites as supercapacitor electrodes. *RSC Adv*. **3**, 25891-25901

[128] O. Mykhailiv, *et al*. (2015) Influence of the Synthetic Conditions on the Structural and Electrochemical Properties of Carbon Nano-Onions. *ChemPhysChem.* **16**, 2182-2191

[129] M. E. Plonska-Brzezinska, A. T. Dubis, A. Lapinski, A. Villalta-Cerdas, L. Echegoyen (2014) Electrochemical propertiesof oxidized carbon nano-onions: DRIFTS-FTIR and Raman spectroscopic analyses. *ChemPhysChem*. **12**, 2659-2668

[130] M. E. Plonska-Brzezinska, A. Molina-Ontoria, L. Echegoyen (2014) Post-modification by low-temperature annealing of carbon nano-onions in the presence of carbohydrates. *Carbon* **67**, 304-317

[131] A. V. Gubarevich, J. Kitamura, S. Usuba, H. Yokoi, Y. Kakudate, O. Odawara (2003) Onion-like carbon deposition by plasma spraying of nanodiamonds. *Carbon* **41**, 2601-2606

[132] J. Xiao, G. Ouyang, P. Liu, C. Wang, G. Yang (2014) Reversible nanodiamond-carbon onion phase transformations. *Nano Lett*. **14**, 3645-3652

[133] F. Banhart, T. Fuller, P. Redlich, P. Ajayan (1997) The formation, annealing and self-compression of carbon onions under electron irradiation. *Chem. Phys. Lett*. **269**, 349-355

[134] D. Ugarte (1992) Morphology and structure of graphitic soot particles generated in arc-discharge C60 production. *Chem. Phys. Lett*. **198**, 596-602

[135] A. B. Du, X. G. Liu, D. J. Fu, P. D. Han, B. S. Xu (2007) Onion-like fullerenes synthesis from coal. *Fuel* **8**, 294- 298

[136] D. Ugarte (1992) Curling and closure of graphitic networks under electron-beam irradiation. *Nature* **359**, 707-709

[137] V. Serin, *et al*. (2000) Evidence for the solubility of boron in graphite by electron energy loss spectroscopy, *Carbon* **38**, 547-554

[138] Y. Gao, *et al*. (2013) Chemical activation of carbon nanoonions for high-rate supercapacitor electrodes. *Carbon* **51**, 52-58

[139] R. Borgohain, J. Yang, J. P. Selegue, D. Y. Kim (2014) Controlled synthesis, efficient purification, and electrochemical characterization of arc-discharge carbon nano-onions. *Carbon* **66**, 272-284

[140] M. E. Plonska-Brzezinska, A. Palkar, K. Winkler, L. Echegoyen (2010) Electrochemical properties of small carbon nano-onion films. *Electrochem. Solid-State Lett.* **13**, K35-K8

[141] S. Sek, J. Breczko, M.E. Plonska-Brzezinska, A.Z. Wilczewska, L. Echegoyen (2013) STM-based molecular junction of carbon nano-onion. *ChemPhysChem*. **14**, 96-100

[142] M.-S. Wang, D. Golberg, Y. Bando (2010) Carbon ‘‘onions” as point electron sources. *ACS Nano* **4**, 4396-4402

[143] M. Olariu, A. Arcire, M.E. Plonska-Brzezinska (2017) Controlled trapping of onionlike carbon (OLC) via dielectrophoresis. *J. Electron. Mater.* **46**, 443-450

[144] S. Tomita, M. Fujii, S. Hayashi (2002) Optical extinction properties of carbon onions prepared from diamond nanoparticles. *Phys. Rev. B*. **66**, 255424

[145] N. Keller, *et al*. (2002) The catalytic use of onion-like carbon materials for styrene synthesis by oxidative dehydrogenation of ethylbenzene. *Angew. Chem. Int. Ed. Engl.* **41**, 1885-1888

[146] D. Su, N.I. Maksimova, G. Mestl, V.L. Kuznetsov, V. Keller, R. Schlögl, N. Keller (2007) Oxidative dehydrogenation of ethylbenzene to styrene over ultra-dispersed diamond and onion-like carbon. *Carbon* **45**, 2145-2151

[147] M.E. Plonska-Brzezinska, L. Echegoyen (2013) Carbon nano-onions for supercapacitor electrodes: recent developments and applications. *J. Mater. Chem. A* **1**, 13703

[148] F.-D. Han, B. Yao, Y.-J. Bai (2011) Preparation of carbon nano-onions and their application as anode materials for rechargeable lithium-ion batteries. *J. Phys. Chem. C* **115**, 8923-8927

[149] W. Gu, N. Peters, G. Yushin (2013) Functionalized carbon onions, detonation nanodiamond and mesoporous carbon as cathodes in Li-ion electrochemical energy storage devices. *Carbon* **53**, 292-301

[150] A. Hirata, M. Igarashi, T. Kaito (2004) Study on solid lubricant properties of carbon onions produced by heat treatment of diamond clusters or particles. *Tribol. Int.* **37**, 899-905

[151] L. Joly-Pottuz, *et al.* (2008) Diamond-derived carbon onions as lubricant additives, *Tribol. Int.* **41**, 69-78

[152] C. Shu, Y. Lin, B. Zhang, S.B. Abd Hamid, D. Su (2016) Mesoporous boron-doped onion-like carbon as long-life oxygen electrode for sodium–oxygen batteries. *J. Mater. Chem. A* **4**, 6610-6619

[153] L. Joly-Pottuz, *et al.* (2010) Friction properties of carbon nano-onions from experiment and computer simulations. *Tribol. Lett.* **37**, 75-81

[154] J. Luszczyn, *et al.* (2010) Small noncytotoxic carbon nano-onions: first covalent functionalization with biomolecules. *Chem. Eur. J.* **16**, 4870-4880

[155] J. Breczko, M.E. Plonska-Brzezinska, L. Echegoyen (2012) Electrochemical oxidation and determination of dopamine in the presence of uric and ascorbic acids using a carbon nano-onion and poly(diallyldimethylammonium chloride) composite. *Electrochim. Acta* **72**, 61-67

[156] J. Bartelmess, S. Giordani (2014) Carbon nano-onions (multi-layer fullerenes): chemistry and applications. *Beilstein J. Nanotechnol.* **5**, 1980-1998

[157] S. Giordani, *et al.* (2014) NIR fluorescence labelled carbon nano-onions: synthesis, analysis and cellular imaging. *J. Mater. Chem. B* **2**, 7459-7463

[158] R. Landauer (1988) Spatial variation of currents and fields due to localized scatterers in metallic conduction. *IBM J. Res. Dev.* **32**, 306-316,

[159] T.B. Martins, R.H. Miwa, A.J.R. da Silva, A. Fazzio (2007) Electronic and transport properties of boron-doped graphene nanoribbons. *Phys. Rev. Lett.* **98**, 196803

[160] S.K. Das, S. Lau, L.A. Archer (2014) Sodium–oxygen batteries: a new class of metal-air batteries. *J. Mater. Chem. A*. **2**, 12623

[161] S.-M. Kim, et al. (2016) In situ formation of nitrogen-doped onion-like carbon as catalyst support for enhanced oxygen reduction activity and durability. *Carbon* **101**, 420-430

[162] X. Liu, et al. (2013) Co3O4/C nanocapsules with onion-like carbon shells as anode material for lithium ion batteries. *Electrochim. Acta* **100**, 140-146

[163] X. Liu, et al. (2013) NiO/C nanocapsules with onionlike carbon shell as anode material for lithium ion batteries. *Carbon* **60**, 215-220

[164] M.B. Seymour, C. Su, Y. Gao, Y. Lu, Y. Li (2012) Characterization of carbon nanoonions for heavy metal ion remediation. *J. Nanoparticle Res.* **14**, 1087

[165] B. Geogakilas, J. A. Perlman, J. Tucek, R. Zboril (2015) Broad Family of Carbon Nanoallotropes: Classification, Chemistry and Applications of Fullerenes, Carbon Dots, Nanotubes, Graphene, Nanodiamonds and Combined Superstructures. *Chem. Rev.* **115**, 4744-4822

[166] F. Pietrucci and Wanda Andreoni (2014) Fate of Graphene Flake: A New Route toward Fullerenes Disclosed with Ab Initio Simulations. *J. Chem. Theory Comput.* **10**, 913-917

[167]A. Szabo and N. Ostlund (1994) Modern Quantum Chemistry Introduction to Advanced Electronic Structure Theory London, Macmillan Publishing CO. INC , Collier Macmillan Publishers

[168]R. G. Parr and W. Yang (1989) Density Functional Theory of Atoms and Molecules Oxford, Clarendon Press, New York, Oxford University Press

[169]G. De Luca (2013) Assessment of the key properties of materials used in mem-brane reactors by quantum computational approaches Handbook of membrane reactors. *Woodhead Publishing Limited*, **17**, 598-626

[170]A. D. Becke (1993) Density-functional thermochemistry. III. The role of exact exchange *J. Chem. Phys*., **98**, 5648

[171]J. P. Perdew, K. Burke and M. Ernzerhof (1997) Generalized gradient approx-imation made simple. *Phys. Rev. Lett*., **78**, 1396

[172]X. Xu, W.A. Goddard (2004) The X3LYP extended density functional for accurate descriptions of nonbond interactions, spin states, and thermochemical properties. *PNAS* **101**, 2673-2677

[173]F. Pacios and P.A. Christiansen (1985) Ab initio relativistic effective potentials with spin-orbit operators. I. Li through Ar *J. Chem. Phys*., **82**, 2664 2671

[174]C. C. J. Roothan (1951) New developments in molecular orbital theory. *Rev. Mod. Phys*. **23**, 69

[175] R. G. Parr, W. Yang (1984) Density functional approach to the frontier-electron theory of chemical reactivity. *J. Am. Chem. Soc.*, **106**, 4049-4050

[176] S. R. Sanderson (1951) An interpretation of Bond Lengths and Clasiffication Bonds. *Science,* **114**, 670

[177] S. R. Sanderson, *Chemical Bonds and Bond Energy*, 2d edn. New York: Academic Press (1976)

[178] R. G. Parr, R. A. Donnelly, M. Levy, W. E. Palke (1978) Electronegativity:The density Functional viewpoint. *J. Chem. Phys.*, **68**, 3801

[179] R. S. Mulliken (1934) Electronic Structures of Molecules XII. Electroaffinity and Molecular Orbitals, Polyatomic Applications. *J. Chem Phys.*, 3, 586

[180] R. G. Parr, R. G. Pearson (1983) Absolute Hardness: companion parameter to absolute electronegativity. *J. Am. Chem. Soc.*, **105**, 7512-7516

[181] W. Yang, R. G. Parr (1985) Hardness, softness and the fukui function in the electronic theory of metals and catalysis. *Proc. Natl. Acad. Sci. USA*, **82**, 6723-672

[182] G. De Luca, E Sicilia, N. Russo, T. Mineva (2001) On The harness Evaluation in Solvent for Neutral and Charged Systems. *J. Am. Chem. Soc.*, **124**, 1494-1499

[183] Atkins, Peter; de Paula, Julio (2006). Atkins' Physical Chemistry (8th ed.). United States: *Oxford University Press*. *ISBN 0-7167-8759-8*

[184] I. N. Levine (1991) Quantum Chemistry (4th ed.). United States: *Prentice-Hall*. *ISBN 0-205-12770-3*

[185] Australian Microscopy & Microanalysis Research Facility www.ammrf.org.au/

[186]" http://www.nanoscience.gatech.edu/zlwang/research/tem.html#2"

[187]A. W. Coats and J. P. Redfern (1963) Thermogravimetric Analysis. A review. *Analyst* 88, 906-924

[188]G. R. Heal (2002) Compositional Analysis by Thermogravimetry. In P. J. Haines (ed) Royal Society in Chemistry. Cambridge

[189]V. L. Kuznetsov, A. L. Chuvilin, Y. V. Butenko, L. Y. Mal'kov, V. M. Titov (1994) Onion-like carbon from ultra-disperse diamond. *Chem. Phys. Lett*. **222**, 343–348

[190]D. Roy, M. Chhowalla, H. Wang, N. Sano, I. Alexandrou, T. Clyne, G.A. Amaratunga (2003) Characterisation of carbon nano-onions using Raman spectroscopy. *Chem. Phys. Lett*. **373**, 52-56

[191]N. Sano, H. Wang, M. Chhowalla, I. Alexandrou, G.A.J. Amaratunga (2001) Synthesis of carbon ''onions" in water, *Nature* **414**, 506-507

[192]N. Sano, H. Wang, I. Alexandrou, M. Chhowalla, K.B.K. Teo, G.A.J. Amaratunga, K. Iimura (2002) Properties of carbon onions produced by an arc discharge in water. *J. Appl. Phys.* **92**, 2783

[193]M. Choucair, J.A. Stride (2012) The gram-scale synthesis of carbon onions. *Carbon* **50,** 1109-1115

[194]T. Cabioc'h, M. Jaouen, E. Thune, P. Guérin, C. Fayoux, M. Denanot (2000) Carbon onions formation by high-dose carbon ion implantation into copper and silver. *Surf. Coat. Technol.* **128**, 43–50

[195]X. Chen, F. Deng, J. Wang, H. Yang, G. Wu, X. Zhang, J. Peng, W. Li (2001) New method of carbon onion growth by radio-frequency plasma-enhanced chemical vapor deposition. *Chem. Phys. Lett*. **336**, 201-204

[196]M. Choi, I.S. Altman, Y.-J. Kim, P.V. Pikhitsa, S. Lee, G.-S. Park, T. Jeong, J.-B. Yoo (2004) Formation of shell-shaped carbon nanoparticles above a critical laser power in irradiated acetylene. *Adv. Mater*. **16**, 1721-1725

[197]I. Alexandrou, H. Wang, N. Sano, G.A.J. Amaratunga (2004) Structure of carbon onions and nanotubes formed by arc in liquids. *J. Chem. Phys*. **120**, 1055

[198]S. Tomita, T. Sakurai, H. Ohta, M. Fujii, S. Hayashi (2001) Structure and electronic properties of carbon onions. *J. Chem. Phys*. **114**, 7477

[199]K.W. Street, M. Marchetti, R.L. Vander Wal, A.J. Tomasek (2004), Evaluation of the tribological behavior of nano-onions in krytox 143AB. *Tribol. Lett*. 16, 143-149

[200]Y. Gan, F. Banhart (2008) The mobility of carbon atoms in graphitic nanoparticles studied by the relaxation of strain in carbon onions. *Adv. Mater*. **20**, 4751-4754

[201]V.L. Kuznetsov, A.L. Chuvilin, E.M. Moroz, V.N. Kolomiichuk, S.K. Shaikhutdinov, Y.V. Butenko, I.Y. Mal'kov (1994) Effect of explosion conditions on the structure of detonation soots: ultradisperse diamond and onion carbon, *Carbon* **32**, 873-88

[202]E. Wajs, A. Molina-Ontoria, T.T. Nielsen, L. Echegoyen, A. Fragoso (2015) Supramolecular solubilization of cyclodextrin-modified carbon nano-onions by host-guest interactions, *Langmuir* **31**, 535-541

[203]A. Palkar, F. Melin, C.M. Cardona, B. Elliott, A.K. Naskar, D.D. Edie, A. Kumbhar, L. Echegoyen (2007) Reactivity differences between carbon nano onions (CNOs) prepared by different methods, *Chem. Asian J*. **2**, 625-633

[204]T. Cabioc'h, M. Jaouen, J.P. Rivière, J. Delafond, G. Hug (1997) Characterization and growth of carbon phases synthesized by high temperature carbon ion implantation into copper. *Diam. Relat. Mater*. **6**, 261-265

[205] T. Cabioc'h, A. Kharbach, A. Le Roy, J.P. Rivière (1998) Fourier Transform infra-red characterization of carbon onions produced by carbon-ion implantation. *Chem. Phys. Lett*. **285**, 216-220

[206]T. Cabioc'h, M. Jaouen, J.C. Girard (1998) Thin film of spherical carbon onions onto silver. *Carbon* **36**, 499-502

[207]T. Cabioc'h, E. Thune, M. Jaouen (2002) Mechanisms involved in the formation of onionlike carbon nanostructures synthesized by ion implantation at high temperature. *Phys. Rev. B*. **65**, 132103

[208]J. Du, R. Zhao, Z. Zhu (2011) A facile approach for synthesis and in situ modification of onion-like carbon with molybdenum carbide. *Phys. Status Solidi A* **208**, 878-881

[209]M. Bystrzejewski, M.H. Rummeli, T. Gemming, H. Lange, A. Huczko (2010) Catalystfree synthesis of onion-like carbon nanoparticles. *New Carbon Mater*. **25**, 1-8

[210]G. Radhakrishnan, P.M. Adams, L.S. Bernstein (2007) Plasma characterization and room temperature growth of carbon nanotubes and nano-onions by excimer laser ablation. *Appl. Surf. Sci*. **253**, 7651-7655

[211]M. Zhao, H. Song, X. Chen, W. Lian (2007) Large-scale synthesis of onion-like carbon nanoparticles by carbonization of phenolic resin. *Acta Mater*. **55**, 6144-6150

[212]S. Welz, M.J. McNallan, Y. Gogotsi (2006) Carbon structures in silicon carbide derived carbon. *J. Mater. Process. Technol*. **179**, 11-22

[213]J.Y. Huang, H. Yasuda, H. Mori (1999) Highly curved carbon nanostructures produced by ball-milling. *Chem. Phys. Lett*. **303**, 130-134

[214]T. Kobayashi, T. Sekine (2003) H. He, Formation of carbon onion from heavily shocked SiC. *Chem. Mater*. **15**, 2681-2683

[215]A.E. Aleksenskii, M.V. Baidakova, A.Y. Vul', V.Y. Davydov, Y.A. Pevtsova (1997) Diamond-graphite phase transition in ultradisperse-diamond clusters. *Phys. Solid State* **39**, 1007-1015

[216]D. Baowan, N. Thamwattana, J.M. Hill (2007) Continuum modelling of spherical and spheroidal carbon onions. *Eur. Phys. J*. **44**, 117-123

[217]I. Ponomareva, L. Chernozatonskii (2003) How can carbon onion transform into diamond-like structure. *Microelectron. Eng*. **69**, 625-628

[218]T. W. Ebbesen, P. M. Ajayan (1992) Large-scale synthesis of carbon nanotubes, *Nature* **358**, 220-222

[219]S. Karthikeyan, P. Mahalingam, M. Karthik (2009) Large Scale Synthesis of Carbon Nanotubes. *E. Journal of Chemistry* **6**, 1-12

[220]N. Sano, M. Naito, M. Chhowalla, T. Kikuchi, S. Matsud, K. Iimura K, *et al* (2003). Pressure effects on nanotubes formation using the submerged arc in water method. *Chem. Phys. Lett.* **378**, 29-34

[221]I. Alexandrou, H. Wang, N. Sano, G. Amaratunga (2004) Structure of carbon onions and nanotubes formed by arc in liquids. *J Chem Phys* **120**,1055

[222]A. S. Rettenbacher, B. Elliott, J. S. Hudson, A. Amirkhanian, L. Echegoyen (2005) Preparation and functionalization of multilayer fullerenes (carbon nano-onions). *Chem Eur J.* **11**, 1-13

[223]L. Echegoyen, A. Ortiz, M. N. Chaur, A. J. Palkar (2010) *Carbon nano onions. In Chemistry of nanocarbons*. Akasaka T, Wudl F, Nagase S, Eds; John Wiley & Sons: Chichester, UK, 463-83

[224]R. Borgohain, J. Yang, J. P. Selegue, D. Y. Kim (2014) Controlled synthesis, efficient purification, and electrochemical characterization of arc-discharge carbon nano-onions. *Carbon* **66**, 272-84

[225]H. Lange, D.R.M. Walton (2003) Nanocarbon production by arc discharge in water. *Carbon* **41**, 1617-1623

[226]K. Imasaka, J. Suehiro, Y. Kanatake, Y. Kato, M. Hara (2006) Preparation of water-soluble carbon nanotubes using a pulsed streamed discharge in water. *Nanotechnology* **17**, 3421-3427

[227]A. Palkar, F. Melin, C. Cardona, B. Elliot, A. Naskar, *et al,* (2007) Reactivity Difference between Carbon Nano Onions (CNOs) Prepared by Different Methods. *Chem. Asian J.* **2**, 625-633

[228]H. Lange, M. Sioda, A. Huczko, Y. Q. Zhu, H. W. Kroto, D. M. R.Walton (2003) Nanocarbon production by arc discharge in water. **Carbon 41**,1617-1623

[229] F. Alessandro, A. Scarcello, M.D. Basantes Valverde, D.C. Coello Fiallos, S.M. Osman, A. Cupolillo, A. Aloise, E. Curcio and L.S. Caputi (2017) Selective synthesis of polyhedral carbon nano-onions by underwater arc discharge (submitted Carbon: https://ees.elsevier.com/carbon/coAuthorLinkToOrcid.asp)

[230]H. W. Kroto, J. R. Heath, S. C. O´Brien, R. F. Curl, R. E. Smalley (1985) C60: Buckminsterfullerene. *Nature* **318**, 162-163

[231]S. Iijima (1980) Direct observation of tetrahedral bonding in graphitized carbon black by high resolution electron microscopy. *J. Cryst. Growt* **50**, 675-683

[232]V. Z. Mordkovich, Y. Takeuchi (2002) Multishells fullerenes by laser vaporization of composite carbon-metal targets. *Chem. Phys. Lett.* **355**, 133-138

[233]M. Zeiger, N. Jäckel, M. Aslan, D. Weingarth, V. Presser (2015) Understanding structure and porosity of nanodiamond derived carbon onions. *Carbon* **84**, 584-598

[234]D. W. M. Lau, D. G. McCulloch, N. A. Marks, N. R. Masden, A. V. Rode (2007) High-temperature of concentric fullerene-like structures within foam-like carbon: Experiment and molecular dynamics simulation. *Phys. Rev. B*, **75**, 233408

[235]L. Hawelek, A. Brodka, S. Tomita, J. C. Dore, V. Hokimäki, A. Burian (2011) Transformation of nano-diamonds to carbon nano-onions studied by X-ray diffraction and molecular dynamics. *Diamond & Related Materials* **20**, 1333-1339

[236] D. C. Pujals, O. Arias de Fuentes, L. F. Desdin Garcia, E. Cazzanelli, L. S. Caputi (2015) Raman spectroscopy of polyherdral carrbon ano-onions. *Appl. Phys. A* **120**, 1339-1345

[237] K. Doore, M. Cook, E. Clausen, P. V. Lukashev, T. E. Kidd, A. J. Stollenwerk (2017)

[238]Electronic Structure of multi-walled carbon fullerenes. *J. Phys. Condens. Matter* **29**, 075302

[239] M. Kaur, R. S. Sawhney, D. Engles (2017) Linear response formulism of a carbon-onion stringed to gold electrodes. *Appl. Phys. A* **123**, 292

[240]A. A. Voityuk, M. Solà (2016) Photoinduced Charge Separation in the Carbon Nano-Onion C60@C240. *J. Phys. Chem. A* **120**, 5798-5804

[241]M. V. Diudea, A. Bende, C. L Nagy (2014) Carbon multi-shell cages. *Phys. Chem. Chem. Phys.* DOI: 10.1039/c3cp55309d

[242]B. Adhikari, B. Muthuraman, C. Mathioudakis, M. Fyta (2014) Promoting the assembly of carbon onions: An atomistic approach. *Phys. Status Solidi A* **211**, 277-287

[243]O. Boltalina, I. Ioffe, L. Sidorov, G. Seifert, K. Vietze (2000) Ionization Energy of Fullerenes. *J. Am. Chem. Soc.* **122**, 9745-9749

[244]A. B. Atanasov, J. C. Ellenbogen (2017) Simple, accurate electrostatics-based formulas for calculating ionization potentials, electron affinities, and capacitances of fullerenes. *Phys. Rev. B* **95**, 032508

[245]M. Goldberg M (1937) A class of multi-symmetric polyhedra. *Tohoku Math J* **43**, 104–108

[246]S. Schein, J. M. Gayed (2014) Fourth Class of convex equilateral polyhedron with polyhedral symmetry related to fullerenes and viruses. *PNAS* **111**, 2920-2925

[247]C. Cioffi, *et al.* (2009) A Carbon Nano-Onion-Ferrocene Donor-Aceptor System: Synthesis, Characterization and Properties. *Chem. Eur. J* **15**, 4419-4427

[248]G. Brinkmann, OD. Friedrichs, A. Dress, T. Harmuth (1997) CaGe - a virtual environment for studying some special classes of large molecules. *Match-Commun Math Comput Chem.* **36**, 233-23

[249]G. Brinkmann, OD. Friedrichs, S. Lisken, A. Peeters, N. Van Cleemput (2010) CaGe – a virtual environment for studying some special classes of plane graphs - an update. *Match-Commun Math Comput Chem.* **63**, 533-552

[250]Adove Iliustrator CS4. Adobe Systems, Inc.

[251]**www.cgl.ucsf.edu/chimera**

[252]W. Hehre, S. Ohlinger S (2006–2009) Spartan '08 for Windows, MacIntosh and Linux: Tutorial and User's Guide. (Wavefunction, Inc., Irvine, CA).

[253]Wolfram Research, Inc., Mathematica, Version 11.2, Champaign, IL (2017)

[254]P. Schwerdtfeger, L. Wirz, J. Avery (2013) Program: Fullerene a software package for constructing and analyzing structures of regular fullerenes. *J. Comput. Chem.* **17**, 1508

[255]F. Cataldo, A. Graovac, O. Ori, *The Mathematics and Topology of Fullerenes*; Springer:Berlin, 2011

[256]http://www.crystal.unito.it/

[257]http://www.turbomole.com/

[258]I. Noël, M. De La Pierre, C. M. Zicovich-Wilson, R. Orlando, R. Dovesi (2014) Structural, electronic and energetic properties of giant icosahedral fullerenes up to C6000: insights from an ab initio hybrid DFT study. *Phys. Chem. Chem. Phys.* **16**, 13390-13401

[259]A. Perez-Garrido (2000) Giant multilayer fullerene structures with symmetrically arranged defects. Phys. Rev. B 62, 6979-6971

[260]P. Calaminici, G. Geudtner, A. M. Köster (2009) First-Principle Calculations of Large Fullerenes. *J. Chem. Theory Comput.* **5**, 29-32

[261]D. Bakowies, M. Bülh, W. Thiel (1995) Can large fullerenes be spherical**.** *J. Am. Chem. Soc.* **117**, 10113-10118

[262]G. E. Scuseria (1995) The equilibrium structures of giant fullerenes - faceted or spherical shape - An ab-initio Hartree-Fock study of icosahedral. C_{240} and C_{540}. *Chem. Phys. Lett.* **243**, 193-198

[263]Haddon, R. C.; Scuseria, G. E.; Smalley, R. E. C240 (1997)- The most chemically inert fullerene. *Chem. Phys. Lett.* **272**, 38-42

[264]K. R. Bates, G. E. Scuseria (1998) Why are buckyonions round. *Theor. Chem. Acc.* **99**, 29-33

[265]G. E. Scuseria (1996) Ab initio calculations of Fullerenes. ***Science* 271**, 942-945

[266]C. H. Xu, G. E. Scuseria (1996) An O(N) tight-binding study of carbon clusters up to C_{8640}: the geometrical shape of the giant icosahedral fullerenes. *Chem. Phys. Lett*. **262**, 219–226

[267]B. I. Dunlap, D. W. Brenner, J. W. Mintmire, R. C. Mowrey, C. T. White (1991) Local density functional electronic structures of three stable icosahedral fullerenes. *J. Phys. Chem.* **95**, 8737-8741

[268]Yeon-Lieh Lin, F. Nori (1993) Electronic structure of single- and multi shell carbon fullerenes. *Phys. Rev. B* **49**, 5020-5023

[269]J. P. Lu, W. Yang (1994) Shape of large single- and multiple-shell fullerenes. *Phys. Rev. B* **49**, 11421-11424

[270]http://www.nwchem-sw.org/index.php/Main_Page

[271]M. Valiev, E.J. Bylaska, N. Govind, K. Kowalski, T.P. Straatsma, H.J.J. van Dam, D. Wang, J. Nieplocha, E. Apra, T.L. Windus, W.A. de Jong (2010) NWChem: a comprehensive and scalable open-source solution for large scale molecular simulations. *Comput. Phys. Commun*. **181**, 1477

[272]J. P. Perdew, K. Burke, M. Ernzerhof (1996) Generalized Gradient Approximation Made Simple. *Phys. Rev. Lett*. **77**, 3865-3868

[273]D. Manna and J. M. L. Martin (2016) What are the Ground State Structures of C20 and C24? An Explicitly Correlated Ab Initio Approach. *J. Phys. Chem A* **120**, 153-160

[274]G. De Luca, F. Bisignano, A. Figoli, F. Galiano, E. Furia, R. Mancuso, O. Saoncella, M. Carraro, M. Bonchio, B. Gabriele (2014) Bromide Ion Exchange with a Keggin Polyoxometalate on Functionalized Polymeric Membranes: A Theoretical and Experimental Study. *J. Phys. Chem. B* **118**, 2396-2404

[275]N. Shao, Y. Gao, S. Yoo, W. An, X. C. Zeng (2006) Search for Lowest-Energy Fullerenes: C_{98} to C_{110}. *J. Phys. Chem. A* , **110**, 7672-7676.

[276]A. Erba, J. Baima, I. Bush, R. Orlando, R. Dovesi (2017) Large-Scale Condensed Matter DFT Simulations: Performance and Capabilities of the CRYSTAL Code. *J. Chem. Theory Comput.* DOI: 10.1021/acs.jctc.7b00687

[277]R. R. Zope (2008) Electronic structure and static dipole polarizability of C60@C240. *J. Phys. B* **41**, 085101 (4pp)

[278] R. G. Parr, W. Yang (1989) *Density-Functional Theory of Atoms and Molecules*. International Series of Monographs on Chemistry - 16, New York, Oxford University Press

[279]G. R. Lewis, W. E. Bunting, R. R. Zope, B. I. Dunlap, J. C. Ellenbogen (2013) Smooth scaling of valence electronic properties in fullerenes: From one carbon atom, to C_{60}, to graphene. *Phys. Rev. A* **87**, 052515

[280]R. R. Zope, T. Baruah, M. R. Perderson, B. I. Dunlap (2008) Static dielectric response of icosahedral fullerenes from C_{60} to C_{2160} by an all electron density functional theory. *Cond. Mat. Mtrl. Sci.* arXiv:0801.4433v1

[281] G. De Luca, E. Sicilia, N. Russo, T. Mineva (2002) On the Hardness Evaluation in Solvent for Neutral and Charged Systems. *J. Am. Chem. Soc*. **124**, 1494-1499

[282]G. De Luca, M. Basantes V., L.S. Caputi (2017) Valence electronic properties of single and double-wall icosahedral fullerenes: a Comparative DFT Study (submitted J. Phys. Chem. B ID. Jp-2017-12261x)

Publications

1. G. De Luca, M. Basantes V., L.S. Caputi (2017) Valence electronic properties of single and double-wall icosahedral fullerenes: a Comparative DFT Study (submitted J. Phys. Chem. B ID jp-2017-12261x)

2. F. Alessandro, A. Scarcello, M.D. Basantes Valverde, D.C. Coello Fiallos, S.M. Osman, A. Cupolillo, A. Aloise, E. Curcio and L.S. Caputi (2017) Selective synthesis of polyhedral carbon nano-onions by underwater arc discharge (submitted Carbon https://ees.elsevier.com/carbon/coAuthorLinkToOrcid.asp)

3. M. Basantes V., G. De Luca, L.S. Caputi (2017) Theoretical Study of separation properties of single wall icosahedral fullerenes, in preparation.

Posters Participation

2017 International Congress on Membranes and Membrane Processe. 29 July – 4 August 2017

Hilton San Francisco Union Square, San Francisco, CA USA

1. G. De Luca*, M. Basantes, L. S. Caputi (2017) Theoretical Study of separation properties of carbon nanotubes and polyhedral carbon nano-onions
2. G. De Luca. R. Amuso, M. Basantes, F. Galiano, M. Carrano, M. Bochio, A. Figoli (2017) Polyoxometalates in polymer membranes for a more efficient fouling treatment: A nanoscale modelling.

http://www.icom2017.org/program.html

https://elsevier.conference-services.net/resources/247/4142/pages/posterprog.pdf

https://elsevier.conference-services.net/secureProgramme.asp?conferenceID=4142&uID=808011

Appendix A

The dihedral angles θ_1 and θ_2 are shown in the following Figure S1. The full balls in this Figure identifies the planes used to define these dihedrals

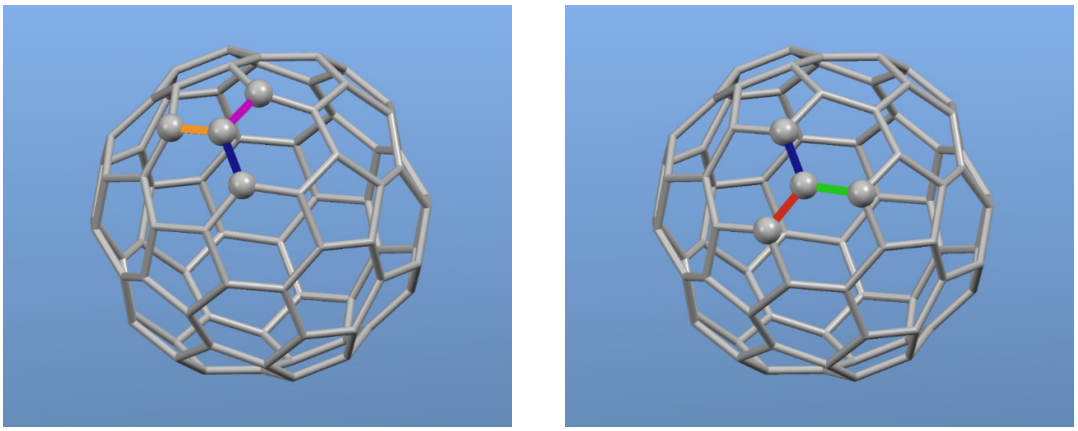

In the Figure S2 θ_1 and θ_2 are are illustrated in a different views, in turn $\theta_1 - \theta_2$ defines the $\Delta_{\theta 1,\theta 2}$

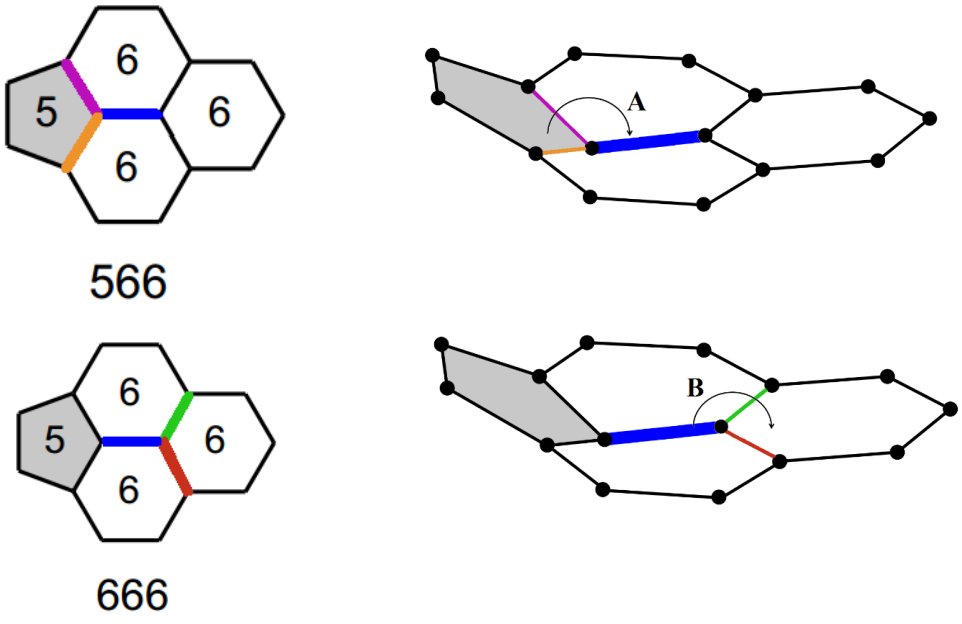

T=4 (2,0) vertices' numbers = 80
Schein and Gayed Merely Equilateral

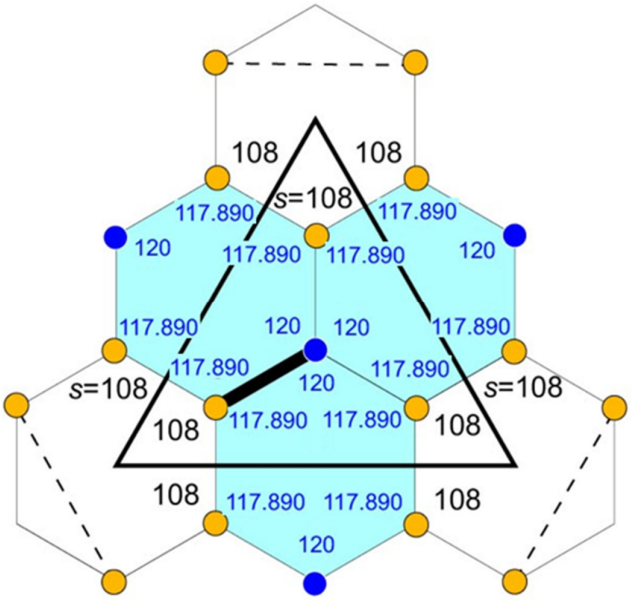

This work

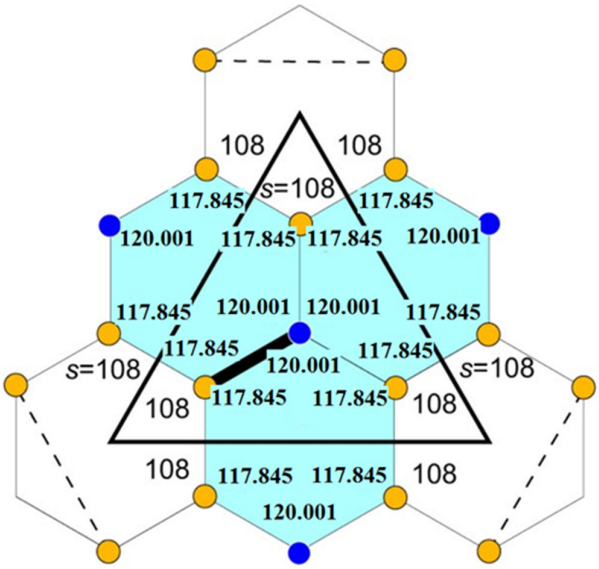

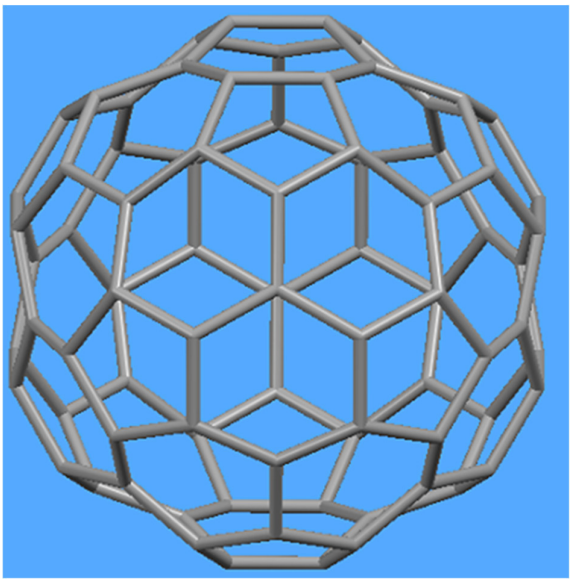

$RMSD_{angles}$ =0.028868°
Schein and Gayed
A=138.2° B=180° A=136.6° B=180°
D^{AB}_{SG} = B – A = 41.8° D^{AB}_{DLBC}= B – A = 43.4°
$\Delta D=D^{AB}_{DLBC} - D^{AB}_{SG}$=1.57°

T=9 (3,0) vertices=180

Merely Equilateral Schein and Gayed

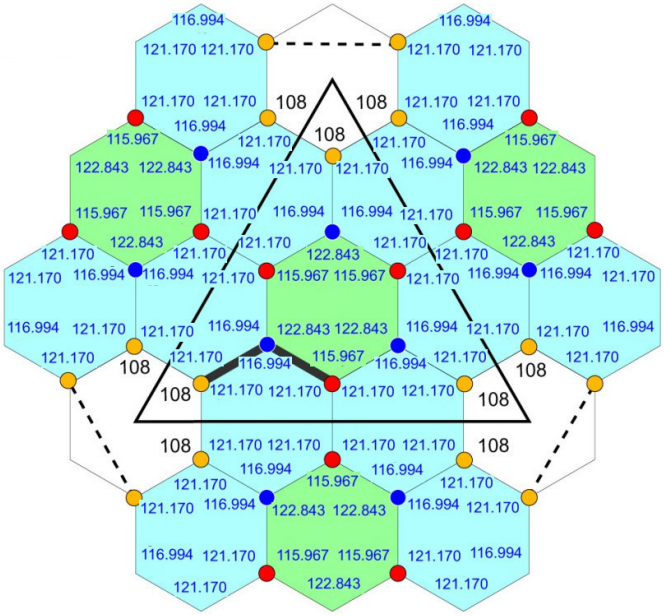

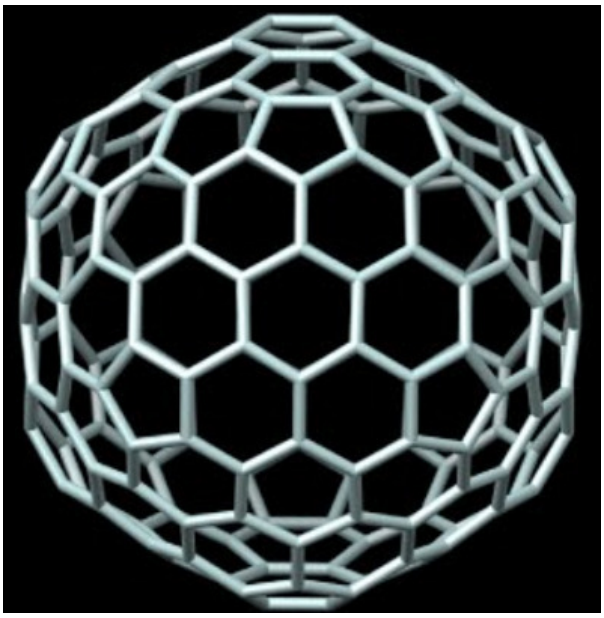

This work

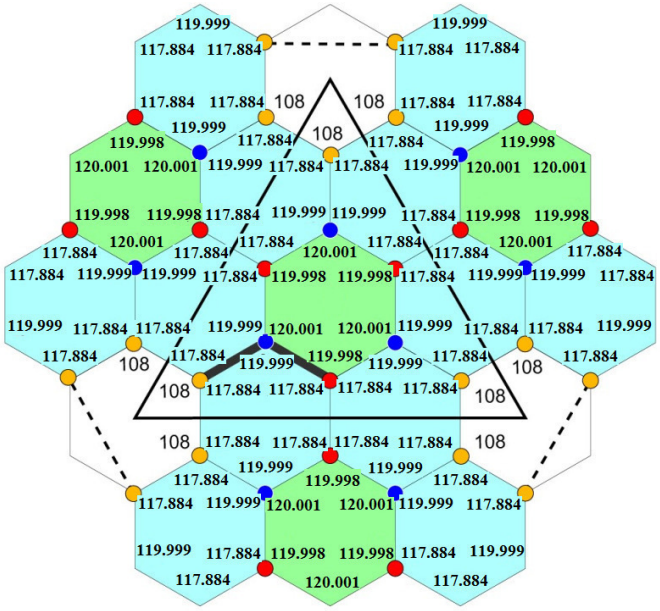

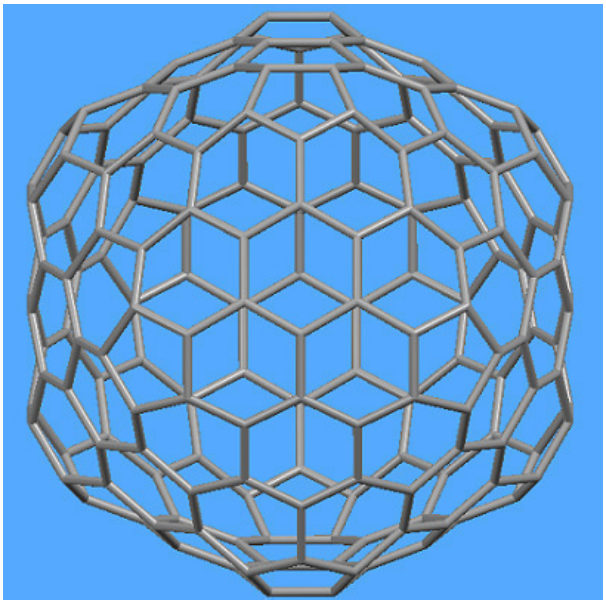

$RMSD_{angles}$ =2.981928°

T=16 (4,0) vertices=320
Merely Equilateral Schein and Gayed

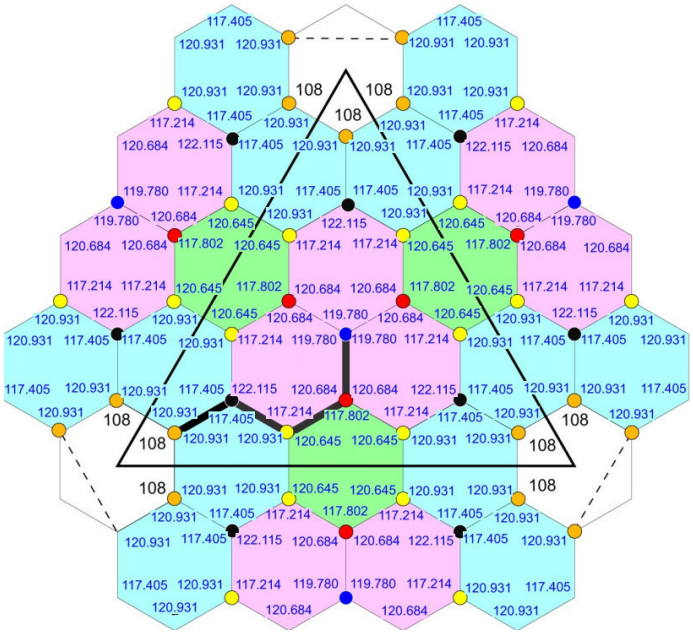

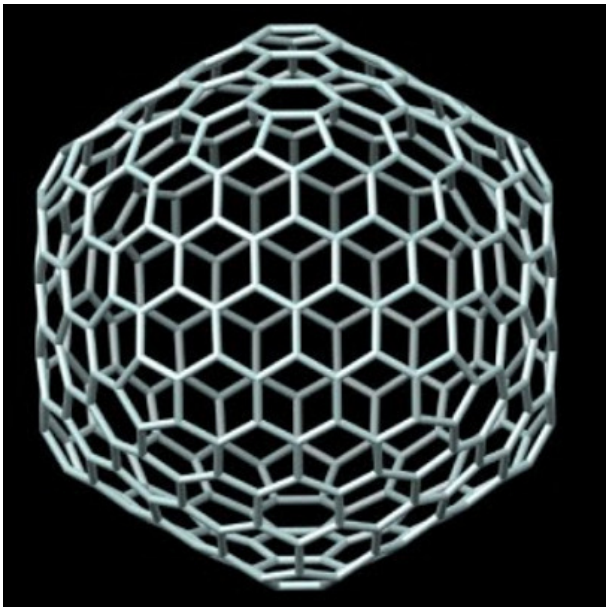

This work

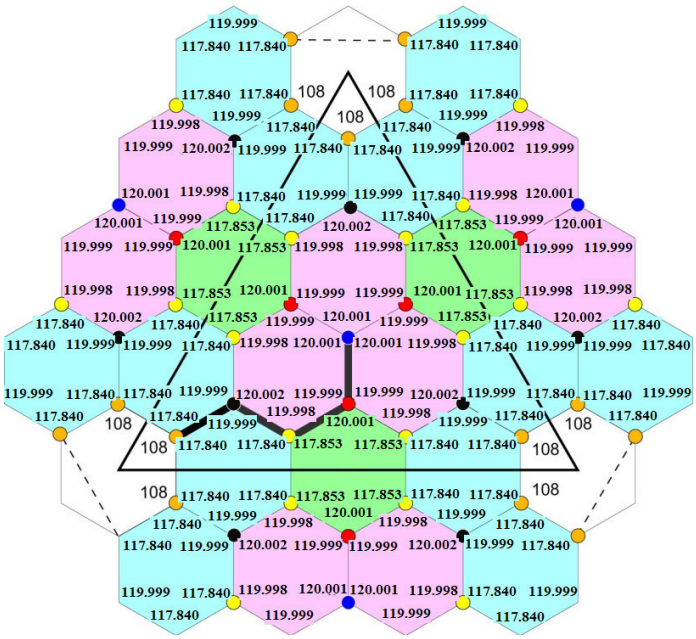

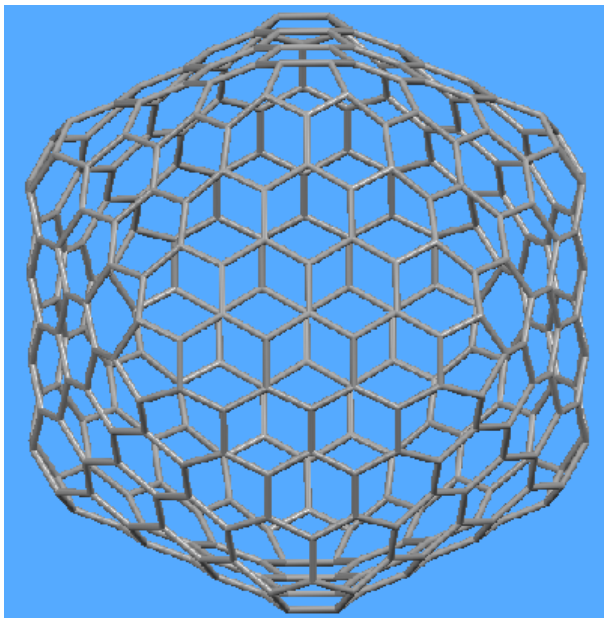

$RMSD_{angles}$ =2.151162°

T=25 (5,0) vertices=500
Merely Equilateral Schein and Gayed

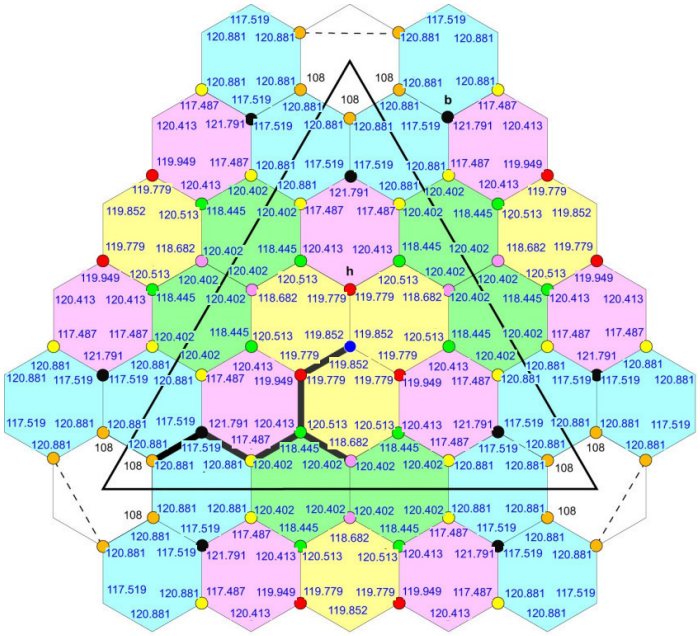

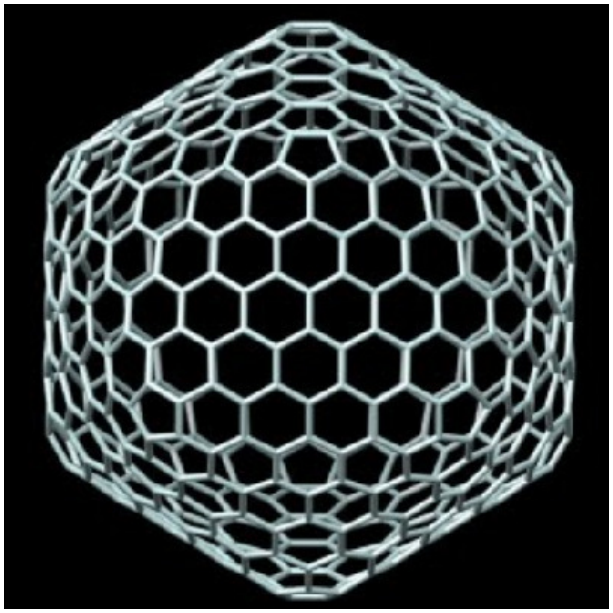

This work

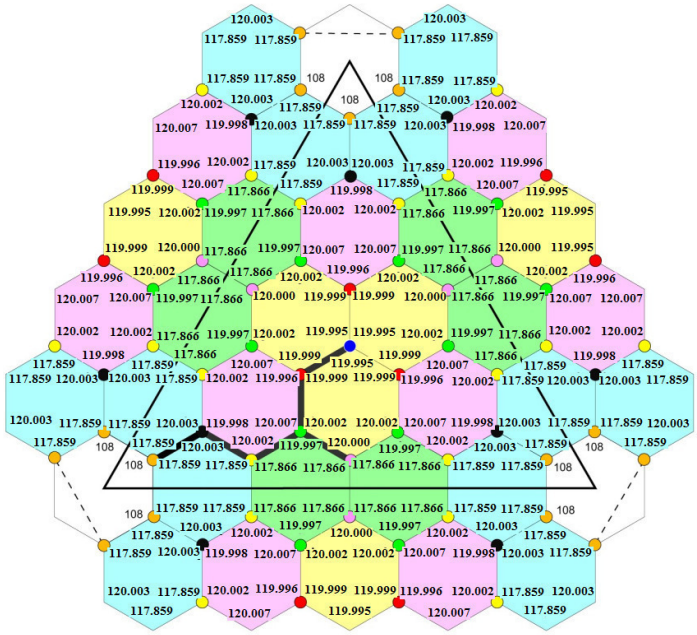

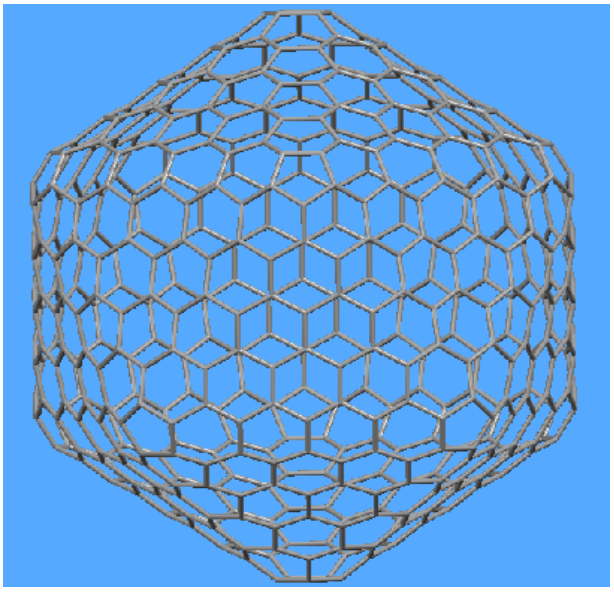

$RMSD_{angles}$ =1.66218°

T=36 (6,0) vertices=720

Merely Equilateral Schein and Gayed

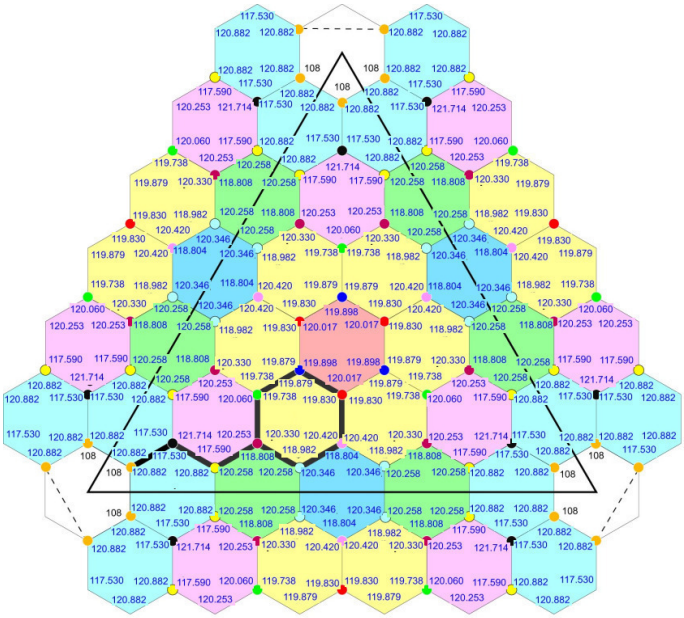

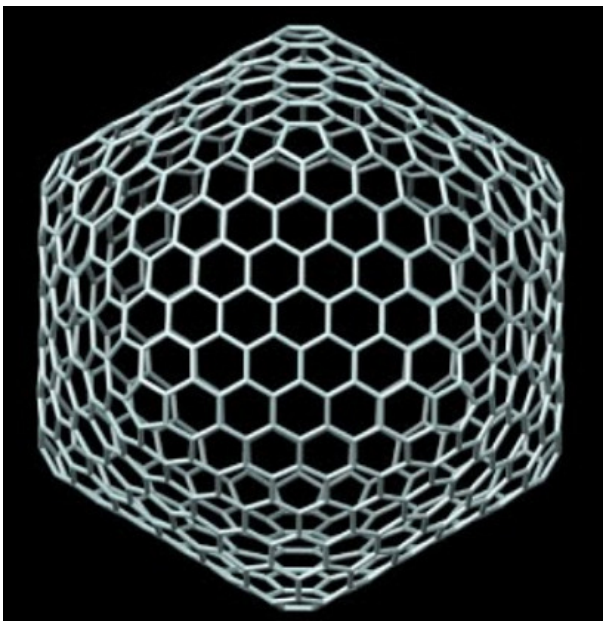

This work

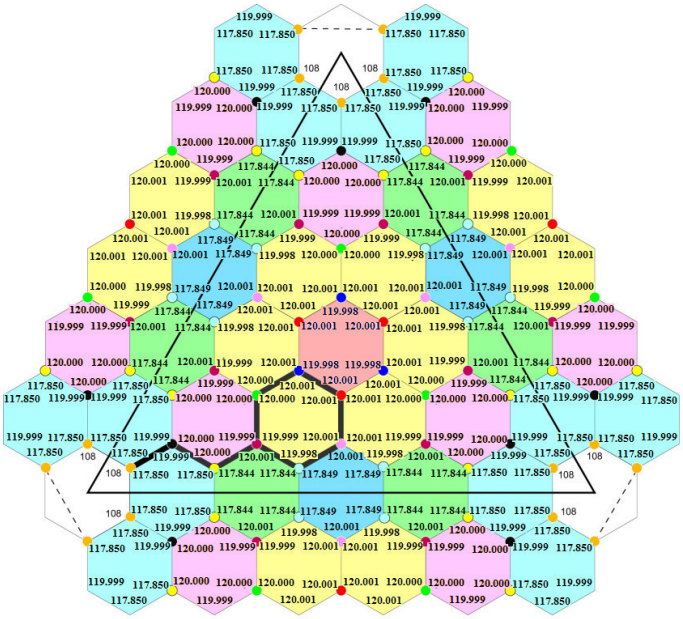

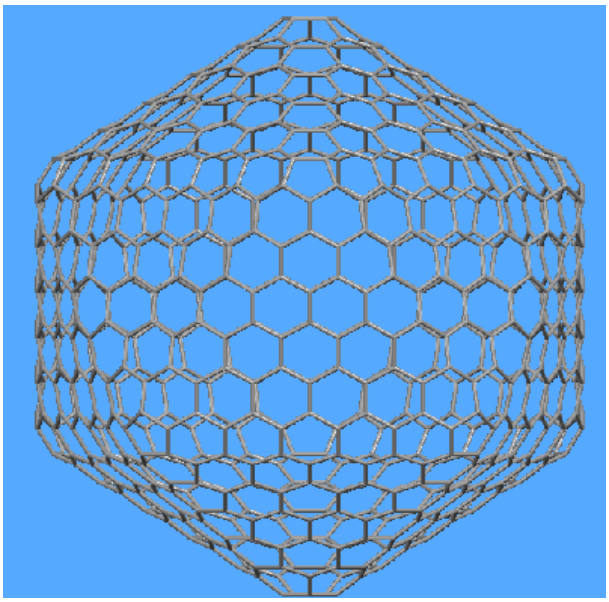

$RMSD_{angles}$ =1.459305°

T=49 (7,0) vertices=980
Merely Equilateral Schein and Gayed

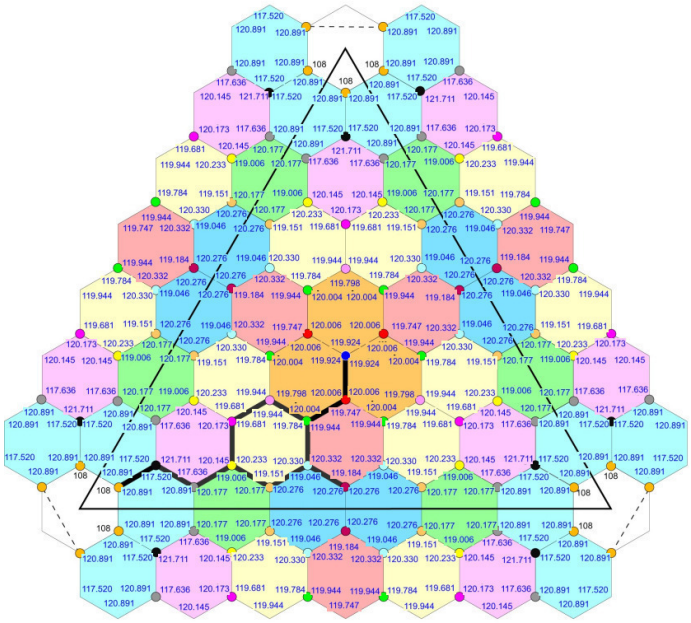

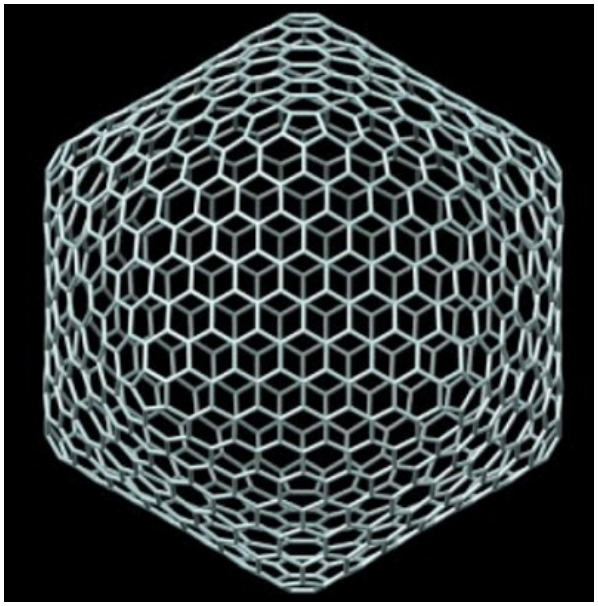

This work

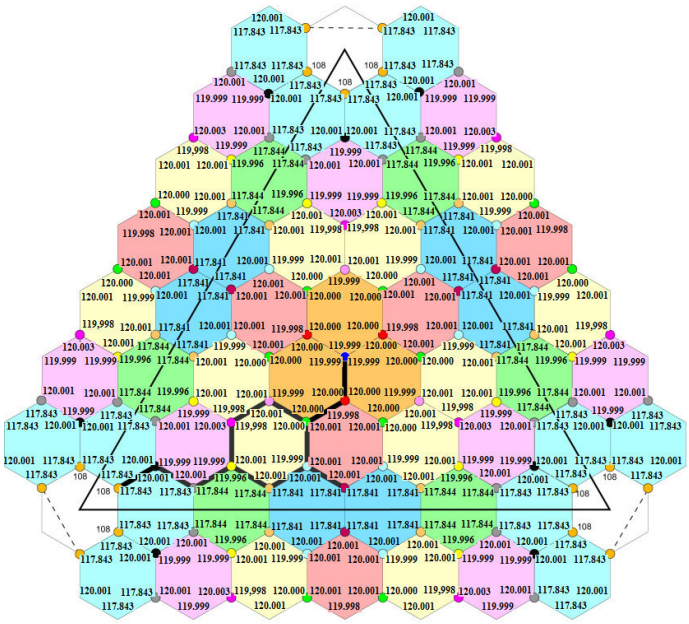

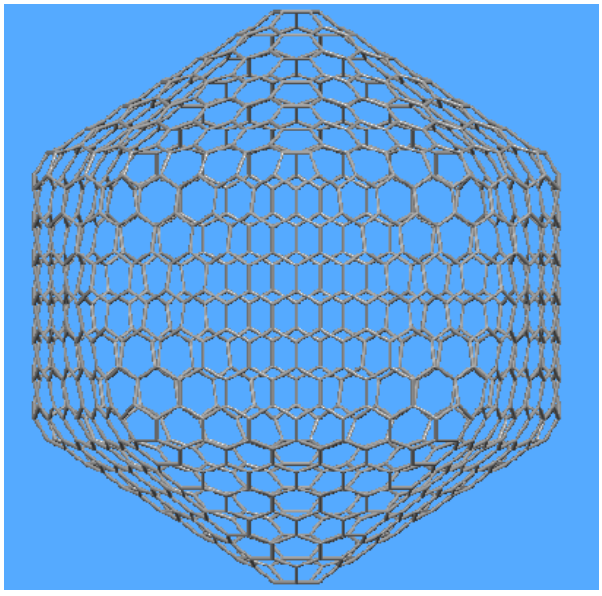

$RMSD_{angles}$ =1.252284°

DAD Equations Number

T	Schein and Gayed	This work
1	-	-
4	1	1
9	2	2
16	4	3
25	6	4
36	9	5
49	12	6

In this case, our homemade algorithm is better than Schein and Gayed because the DAD equations number, as T grows, is significantly lower!